

PDF hosted at the Radboud Repository of the Radboud University Nijmegen

The following full text is a publisher's version.

For additional information about this publication click this link.

<http://hdl.handle.net/2066/204153>

Please be advised that this information was generated on 2019-07-08 and may be subject to change.

A Multistage Zeeman Decelerator for Molecular-Beam Scattering Experiments

Theo Cremers

Copyright © 2019 Theo Cremers

A Multistage Zeeman Decelerator for Molecular-Beam Scattering Experiments

PhD Thesis, Radboud University

Cover design by T. Cremers

Printed by Ipskamp printing

ISBN: 978-94-028-1484-2

A Multistage Zeeman Decelerator for Molecular-Beam Scattering Experiments

Proefschrift

ter verkrijging van de graad van doctor
aan de Radboud Universiteit Nijmegen
op gezag van de rector magnificus prof. dr. J.H.J.M. van Krieken,
volgens besluit van het college van decanen
in het openbaar te verdedigen op vrijdag 14 juni 2019
om 12:30 uur precies

door

Theodorus Leonardus Cremers

geboren op 16 november 1990
te Nijmegen

Promotor: Prof. dr. Sebastiaan Y.T. van de Meerakker

Manuscriptcommissie: Prof. dr. Wilhelm T.S. Huck

Prof. dr. Frédéric Merkt (ETH Zürich, Zwitserland)

Dr. Hendrick L. Bethlem (VU Amsterdam)

Voorwoord

Ik ben niet iemand die veel vooruit plant, dus toen Bas mij vijf jaar geleden vroeg of ik een promotieonderzoek bij hem wilde doen, was dat mijn eerste baanaanbod. Op dat moment zat ik al in de groep van Bas als masterstudent en werkte ik aan het Zeeman project, dat toen nog in zijn kinderschoenen stond. Hierdoor was ik erg geïnteresseerd in het aanbod, want dit gaf mij de mogelijkheid om mijn project tot leven te zien komen. Nou had ik nog niet veel ervaring in het lab, maar vooral met computersimulaties en programmeren, omdat we nog in de ontwerpfase zaten. Terwijl het in elkaar zetten en meten met een nieuw apparaat nogal wat handigheid vereist. In zekere zin nam Bas dus een gok door mij aan te nemen. Hiervoor ben ik hem zeer dankbaar.

De afgelopen vier jaar waren namelijk een geweldige tijd, waarin ik veel geleerd heb over onderzoek doen en molecuulfysica in het algemeen. Werken in het lab ging mij gelukkig goed af, hoewel ik het schrijven van programma's voor de metingen nog steeds met het meeste plezier deed. Maar vooral het samenkomen van alle elementen, software en hardware, gaf de meeste voldoening. Ik kan me de eerste afgeremde atomen nog goed herinneren, een zwak maar duidelijk signaal in een grafiek van aankomsttijden van de atomen. Bewijs dat we werkelijk deze onvoorstelbare kleine deeltjes met onze machine op de rem kunnen zetten.

Wat deze vier jaar helemaal speciaal maakte, waren mijn collega's in de groep 'Spectroscopy of Cold Molecules' (toen ik begon nog 'Cold and Controlled Collisions'). Mijn begeleider, Bas van de Meerakker, wil ik graag bedanken voor de jaren van waardevolle supervisie. Jouw constante interesse in het Zeeman project hielp mij om gemotiveerd te blijven. Tevens had ik door jou nooit een tekort aan nieuwe ideeën om uit te werken. Wat begeleiders betreft ben jij zeker één van de besten. Ik wens je veel succes met toekomstige projecten, en ik hoop dat de Zeeman afremmer hierin een belangrijke rol zal spelen.

Het bouwen van de Zeeman afremmer was bij lange na geen prestatie van mij alleen. Ik ben zeer dankbaar voor de groep technici waarmee het apparaat ontworpen en gebouwd is. De wekelijkse Zeeman-meetings waren altijd een moment om naar uit te kijken. Peter, jouw idee om de spoelen in de afremmer te maken van

koperen capillair legde de grondslag voor het uiteindelijke ontwerp. Bedankt voor jouw betrokkenheid bij het project. Niek, bedankt voor het ontwerpen en testen van de elektronica die de afremmer tot leven wekt. Ook bedankt dat je de vele alledaagse problemen met elektronica wist op te lossen, regelmatig door het open te schroeven, er naar te kijken, en het weer dicht te maken zonder iets aan te passen. Ik vermoed nog steeds dat je stiekem een tovenaars bent. Edwin, jouw oog voor precisie was essentieel bij de constructie en het uitlijnen van de Zeeman afremmer. Ik heb erg genoten van onze samenwerking in het lab. Bedankt voor je harde werk en inzet. Gerben, ik ben telkens onder de indruk van jouw gedetailleerde 3D-modellen van de afremmer. Jij hebt veel problemen opgelost waarvan wij nog niet eens wisten dat ze er waren. Bedankt voor de vele ontwerptekeningen. Sven, bedankt voor het ontwerpen en bouwen van ons prototype. Ook bedankt aan de technische stagiaires die geholpen hebben in het Zeeman project.

Simon, thank you for being an amazing lab partner and for helping me do the experiments with the Zeeman decelerator. I learned a lot from watching you. I also remember fondly the evenings of measuring at the FELIX facility, which resulted in a nice paper. I wish you good luck in your future endeavors. Mijn opvolger, Vikram Plomp, bedankt dat je dit project voort zet. Wij hebben altijd veel vertier in het lab, zelfs als het experiment even tegen zit. Met jouw harde werk weet ik zeker dat je mooie resultaten zult behalen. Zorg goed voor de Zeeman afremmer, want we willen geen herhaling van de grote verstopping. Zhi, thank you for helping us with our first collision experiments. I am sure you will have a great future in China. We hebben ook veel hulp gehad van bachelor studenten. Douwe, Mees, Tim, Jasper, Eline en Marieke; bedankt voor jullie bijdrages.

I would like to thank the rest of the office for the nice atmosphere. Sjoerd, Jolijn, Alex, Roy, Tim, Guoqiang, Quan, Matthieu, Zhongfa, Steffen and Agniva; what an interesting dynamic this group made. I hope my next job will have the same comradeship as I experienced over here. Bedankt Magda en Marian, voor de hulp met administratieve zaken, en het regelen van de beste kamers bij FOM Veldhoven en AMO Lunteren. Chris en Andre, bedankt dat jullie me hielpen met mechanische problemen. Dave, thank you for the scientific insights and for being my original promotor. Thanks to Joost and the people at the FELIX facility for helping us in the experiments with FELICE.

Ik wil ook graag mijn familie en vrienden bedanken voor alle steun door de jaren heen. Jullie luisterden altijd aandachtig naar mij als ik mijn onderzoek probeerde uit te leggen, ondanks dat het waarschijnlijk moeilijk te begrijpen was. Frans en Diana, aan jullie heb ik het meeste te danken, voor meer dan ik hier in een paar zinnen kan opnoemen. Ik kan mij geen betere ouders voorstellen. Ik zal proberen om jullie trots te maken, ook in de toekomst.

Contents

1	Introduction	1
1.1	Decelerators	2
1.2	Phase stability	3
1.3	Outline	5
2	Methods	7
2.1	Molecular beams	8
2.2	The Zeeman effect	12
2.3	Multistage Zeeman deceleration	16
2.4	Detection	21
3	A new concept multistage Zeeman decelerator	27
3.1	Introduction	28
3.2	Zeeman decelerator concept	28
3.3	Conclusions and Outlook	42
4	Multistage Zeeman deceleration of metastable helium	45
4.1	Introduction	46
4.2	Experimental	46
4.3	Results and Discussion	50
4.4	Conclusions and Outlook	56
5	Design and construction of a multistage Zeeman decelerator for molecular-beam scattering experiments	57
5.1	Introduction	58
5.2	Experimental	58
5.3	Results	68
5.4	Conclusions and Outlook	72
6	Multistage Zeeman deceleration of O and O₂	75
6.1	Introduction	76
6.2	Experimental	76
6.3	Results	78

Contents

6.4	Conclusions and Outlook	84
7	Conclusions and Outlook	85
7.1	Scattering experiments	87
7.2	Merged beams	89
A	One dimensional model for phase stability	91
B	Extreme equilibrium phase angles	93
	Bibliography	95
	Summary	103
	Samenvatting	107
	Publications	111
	Curriculum Vitae	113

1

Introduction

Atoms and molecules are the building blocks of the universe. For centuries, researchers have studied the interactions between them. During this time, in order to understand and predict these types of interactions, robust theoretical models have been developed. These were conceived in the form of potential energy surfaces, that describe the energetic landscape between molecules. Combined with the dynamics of the particles, these can accurately describe the interactions between particles. An early example of such a potential energy surface is the Lennard-Jones potential [1]. To test these theoretical models, experimental results are required that probe isolated interactions between molecules. However, interactions on this scale are difficult to study given that the typical size of molecules is on the order of 10^{-10} meters. With the advent of molecular beam techniques, isolated atoms and molecules could be studied in detail. The earliest crossed-beam experiments were performed with effusive beams, with relatively broad velocity distributions [2, 3]. These experiments were greatly improved by the techniques pioneered by Herschbach and Lee in the 1950s, for which they received a Nobel prize in 1987 [4, 5]. For the first time, molecular interactions could be studied in single-collision conditions. As theoretical models continued to grow in scope and complexity, so too had the quality of the experiments. The development of supersonic molecular beams was a major step towards better energy resolution in scattering experiments [6]. Particles in these beams have lower rotational and vibrational energies, and by skimming the molecular beam after it has been produced, collisions take place in an almost background-free environment.

However, even when the best molecular beam sources are used, the energy resolution in a collision experiment is limited by the velocity spread of the parent beams. In order to improve beam parameters such as velocity spread and quantum state purity, additional control over molecular beams is required. Several methods exist that can be used to reduce the initial velocity of molecular beams, such as buffer-gas cooling [7], counter-rotating nozzles [8] or seeded gas mixtures [9]. After the beams are produced, there are several methods that allow for the in-vacuum manipulation of these beams. Some decades after the introduction

of the laser in 1960s, laser cooling of atoms [10, 11] became a prominent technique in producing cold beams. More recently laser cooling of molecules has been demonstrated, although this is inherently much more challenging and limited to a select few molecules [12–16]. A mechanical means of slowing down a supersonic beam using a receding atomic mirror was shown by Narevicius *et al.* [17]. As a more general method of manipulating molecular beams, electric and magnetic fields can be used to adjust the momenta of particles with an electric or magnetic dipole moment [18–20]. Neutral particles with an electric or magnetic dipole moment experience a force when they encounter inhomogeneous electric or magnetic fields, through the Stark and Zeeman effect, respectively. These forces can be used to focus or deflect molecules, but can also be used to change the forward velocity and velocity distribution of a packet of molecules. This thesis describes the development of a magnetic decelerator that prepares molecular beams for crossed-beam scattering experiments.

1.1 Decelerators

In the last two decades, tremendous progress has been made in manipulating the motion of molecules in a molecular beam. Using methods that are inspired by concepts from charged particle accelerator physics, complete control over the velocity of molecules in a beam can be achieved. In particular, Stark and Zeeman decelerators have been developed to control the motion of molecules that possess an electric or magnetic dipole moment using time-varying electric and magnetic fields, respectively. Since the first experimental demonstration of Stark deceleration in 1998 [21], several decelerators ranging in size and complexity have been constructed [20, 22, 23]. Applications of these controlled molecular beams are found in high-resolution spectroscopy, the trapping of molecules at low temperature, and advanced scattering experiments that exploit the unprecedented state-purity and/or velocity control of the packets of molecules emerging from the decelerator [18, 19, 24–27].

While beams of paramagnetic particles have been manipulated with magnetic fields since the experiment of Stern and Gerlach [28], the use of time-varying magnetic fields to slow down molecules in so-called Zeeman decelerators is relatively new. In 2007 the Merkt group at the ETH Zürich first demonstrated Zeeman deceleration using six magnetic-field-producing solenoids to slow down H and D atoms [29, 30]. In parallel to these developments, the Raizen group at the university of Texas developed the atomic coilgun, which consisted of 18 solenoids and was used to decelerate metastable neon atoms [31]. Shortly after, they constructed a 64-solenoid decelerator and were able to decelerate oxygen molecules to near-standstill velocities [32]. In the Merkt group the decelerator was extended to 90 solenoids, which allowed them to decelerate O₂ and show full spin-rovibronic

state selectivity with only a single magnetic sub-level populated [33]. In Tel Aviv, the Narevicious group developed an alternative to the multistage Zeeman decelerator, the magnetic traveling-wave decelerator, in which a moving trap is created by overlapping quadrupole magnetic fields [34]. This technique has been used to confine high density samples of atoms and molecules in magnetic traps [35–37]. In recent years, more groups have developed Zeeman decelerators: Vanhaecke (LAC, France) developed a magnetic traveling-wave decelerator of planar helical coils [38]; Softley (Oxford, UK) developed a multistage Zeeman decelerator based on the Merkt design, with a change to the solenoid cooling system [39–43]; Momose (UBC, Canada) has shown the ability to decelerate and trap O₂ and methyl radicals with a magnetic coilgun similar to Raizen’s design [35, 36, 44]; Carty (Durham, UK) developed a magnetic traveling-wave decelerator similar to the Vanhaecke design, but with changes to the design that allow it to capture a larger part of a molecular beam [45].

1.2 Phase stability

Essential in any experiment that uses a Stark or Zeeman decelerator is a high particle density of the decelerated packet. For this, it is imperative that the molecules are decelerated with minimal losses, i.e., molecules within a certain volume in six-dimensional (6D) phase-space should be kept together throughout the deceleration process [46]. It is a formidable challenge, however, to engineer decelerators that exhibit this so-called phase stability. The problem lies in the intrinsic field geometries that are used to manipulate the beam. In a multistage Zeeman (Stark) decelerator a series of solenoids (high-voltage electrodes) yields the deceleration force as well as the transverse focusing force. This can result in a strong coupling between the longitudinal (forward) and transverse oscillatory motions; parametric amplification of the molecular trajectories can occur, leading to losses of particle density [47, 48].

For Stark decelerators, the occurrence of instabilities can be avoided without changing the electrode design. By operating the decelerator in the so-called $s = 3$ mode [49], in which only one third of the electrode pairs are used for deceleration while the remaining pairs are used for transverse focusing, instabilities are effectively eliminated [47, 50]. The high particle densities afforded by this method have enabled a number of high-resolution crossed-beam scattering experiments, for instance [51–56]. For multistage Zeeman decelerators, several advanced switching protocols have been proposed and tested to mitigate losses. Wiederkehr *et al.* extensively investigated phase stability in a Zeeman decelerator, particularly including the role of the nonzero rise and fall times of the current pulses, as well as the influence of the operation phase angle [57, 58]. Evolutionary algorithms were developed to optimize the switching pulse sequence, significantly

increasing the number of particles that exit from the decelerator [43, 58]. Furthermore, inspired by the $s = 3$ mode of a Stark decelerator, alternative strategies for solenoid arrangements were investigated numerically [58]. Dulitz *et al.* developed a model for the overall 6D phase-space acceptance of a Zeeman decelerator, from which optimal parameter sets can be derived to operate the decelerator at minimum loss [40]. Dulitz *et al.* also proposed and implemented schemes to improve the transverse focusing properties of a Zeeman decelerator by applying reversed current pulses to selected solenoids [39]. Yet, despite the substantial improvements these methods can offer, the phase-stable operation of a multistage Zeeman decelerator over a large range of velocities remains challenging.

The aforementioned traveling-wave decelerators have proven an elegant solution to overcome these intrinsic limitations of multistage decelerators. These decelerators employ spatially moving electrostatic or magnetic traps to confine part of the molecular beam in one or multiple wells that start traveling at the speed of the molecular beam pulse and are subsequently gradually slowed down. In this approach the molecules are confined in genuine potential wells, and stay confined in these wells until the final velocity is reached. Consequently, these decelerators are inherently phase stable, and no losses occur due to couplings of motions during the deceleration process. The acceptances are almost equal in both the longitudinal and transverse directions, which appears to be particularly advantageous for experiments that are designed to spatially trap the molecules at the end of the decelerator. Both traveling-wave Stark [59–61] and Zeeman [34, 38, 62, 63] decelerators have been successfully demonstrated.

For high-resolution scattering experiments, however, there are rather different requirements for the beam than for trapping. Certainly, phase-stable operation of the decelerator—and the resulting production of molecular packets with high number densities—is essential. In addition, tunability over a wide range of final velocities is important, but the ability to reach very low final velocities approaching zero meters per second is often inconsequential. More important is the shape of the emerging packet in phase-space, i.e., the spatial and velocity distributions in both the longitudinal and transverse directions.

Ideally, for crossed-beam scattering experiments the longitudinal acceptance of the decelerator should be relatively large, whereas it should be small in the transverse directions. A broad longitudinal distribution—in the order of a few tens of mm spatially and 10–20 m/s in velocity—is typically required to yield sufficiently long interaction times with the target beam or sample, and to ensure the capture of a significant part of the molecular beam pulse that is available for scattering. In addition, a large longitudinal velocity acceptance allows for the application of advanced phase-space manipulation techniques such as bunch compression and longitudinal cooling to further improve the resolution of the experiment [64]. By contrast, much narrower distributions are desired in the transverse directions.

Here, the spatial diameter of the beam should be matched to the size of the target beam and the detection volume; typically a diameter of several mm is sufficient. Finally, the transverse velocity distribution should be narrow to minimize the divergence of the beam. These desiderata on beam distributions are unfortunately not met by traveling-wave decelerators, where the resulting longitudinal (spatial) distributions are smaller and the transverse distributions are larger than what may be considered ideal for scattering experiments. This thesis describes the development of a multistage Zeeman decelerator that fulfills the aforementioned requirements for crossed-beam scattering experiments.

1.3 Outline

In Chapter 2 an overview is given of the methods that are used throughout this thesis. This includes the theoretical methods that were used to calculate the Zeeman energy, the basics of multistage Zeeman deceleration, and the experimental methods of producing and detecting molecular beams. Chapter 3 describes the new concept for a multistage Zeeman decelerator optimized for crossed-beam scattering experiments. In chapter 4, the experimental implementation of this new concept in a prototype design is reported. This prototype features 24 stages of decelerating solenoids and was tested with beams of metastable helium atoms. Chapter 5 describes the design and construction of a 100-stage decelerator that features additional cooling and pumping capacity compared to the prototype. In this chapter the transverse properties of decelerated beams are characterized via spatial mapping of the radial distribution. In chapter 6 the longitudinal properties in decelerated beams of atomic and molecular oxygen are explored. Finally, in chapter 7 some concluding remarks and prospects for future experiments are given.

2

Methods

This chapter describes the methods that were used to perform the experiments in this thesis. The experiments are described in three steps: First, the creation of a supersonic beam of atoms or molecules with a pulsed valve. Second, the manipulation stage in which a Zeeman decelerator was used to alter the velocities of atoms or molecules into the desired distribution. And finally, the detection region where the resulting distributions are measured. This chapter also contains a short description of the Zeeman effect in the atoms and molecules that are relevant to this thesis.

2.1 Molecular beams

This section describes the types of molecular beams that are used in our experiments and the method with which they are created. We will also describe the type of discharge valves that are used to create excited and radical atoms and molecules for Zeeman deceleration.

2.1.1 Supersonic expansion

Molecular beams can be created by allowing a region of high-pressure gas-phase molecules to expand through a small orifice into a region of lower pressure, such as a vacuum chamber. When the orifice is smaller than the mean-free path of the molecules in the high-pressure region, an effusive molecular beam is created. The velocity distribution of the effusive beam will correspond to the Maxwell-Boltzmann distribution of the high-pressure gas. Alternatively, by increasing the orifice size or the stagnation pressure of the source such that the orifice diameter is bigger than the mean-free path of the molecules, a supersonic molecular beam will form. In a supersonic beam collisions occur between molecules in the orifice and the region immediately beyond it. The molecules that stay on the beam axis are those for which most of the translational and internal energy has been converted to forward velocity [65]. This results in faster beams of molecules that have nearly no internal energy and a narrow velocity spread.

In a supersonic expansion, the molecules initially undergo many collisions near the orifice. However, the local density of the expanding gas quickly decreases away from the orifice and the molecules enter a region where collisions cease to happen. This region is called the 'zone of silence', referring to the near zero speed of sound in the expanding gas. Since interactions between molecules no longer occur, the velocities of the molecules remain unchanged. If we consider an ideal gas that undergoes an adiabatic expansion into vacuum, the terminal flow velocity is given by [66]:

$$V_0(T_0) = \sqrt{\frac{2k_B T_0}{m} \frac{\gamma}{\gamma - 1}}, \quad (2.1)$$

Where T_0 is the stagnation temperature, m is the mass of the molecule, k_B is the Boltzmann constant and γ is the ratio of heat capacities at constant pressure and constant volume. In reality, the flow velocity also depends on the pressure in the gas reservoir. However, at the pressures used in the experiments described in this thesis (1-10 bars) no noticeable change is observed nor expected.

In a supersonic expansion, the expanding jet of molecules will form shockwaves in the form of a barrel around the beamline and a Mach disk further downstream [67]. The exact size and shape of these shockwaves depends on the background pressure in the vacuum chamber. When the beam passes the Mach disk,

the velocity distributions become randomized due to inter-molecular collisions. In order to avoid this disruption of the beam, a skimmer is used to isolate the center part of the molecular beam and transmit it into a chamber of higher vacuum (10^{-7} to 10^{-8} mbar). This avoids the formation of a Mach disk and allows the transmitted molecular beam to travel relatively undisturbed. Random collisions with background gas can still occur, but become much less probable.

As can be seen in equation 2.1 for a given particle of mass m , the flow velocity can be changed by heating or cooling the gas prior to expansion. Other methods of changing the initial velocity of a molecular beam include using seeded gas mixtures [9], buffer gas cooling [7] and counter-rotating nozzles [68]. In our experiments seeded gas mixtures are used to decrease the initial flow velocity of our molecular beams, and to further reduce the rotational and translational temperature. In a gas mixture of two or more molecules, the flow velocity can be calculated approximately with the average properties of the mixed gas with regards to mass and heat capacities. By seeding a small percentage of the molecules of interest in a heavier gas, the flow velocity of these molecules is brought down towards the mean velocity of the heavier gas expansion. Rare gas molecules such as argon, krypton and xenon are chosen as the seed gas, as they are non-reactive.

2.1.2 Pulsed valves

In our experiments we use pulsed valves to produce high-density supersonic molecular beams. However, the realization of a pulsed valve that meets the criteria for scattering experiments is not trivial. Ideally, short pulses of gas are produced with minimal opening and closing times of the valve. Heat generation in the valve mechanism should also be minimized, to avoid unnecessary heating of the gas reservoir. Numerous types of valve designs have been reported on so far. Their opening mechanism are either based on magnetic forces [69, 70], or on piezoelectric crystals [71, 72]. For the experiments described in this thesis, two valve designs were used: The commercially available Even-Lavie valve (ELV) [73] and the Nijmegen pulsed valve (NPV) [74]. The NPV was designed and built in our local workshop.

The ELV opening mechanism is initialized by a small current through a solenoid inside the valve body. Inside the solenoid is a magnetic rod with a spring that closes the nozzle. When a current pulse is applied, the magnetic rod experiences a force that pulls it against the spring and the nozzle is briefly opened. The nozzle opening diameter is specified to be $100 \mu\text{m}$, and continues in a 40° conical shape. Typical pulse times for the solenoid currents are between 10 and $25 \mu\text{s}$. The valve produces beams with a high speed ratio ($v/\Delta v$) and can be operated at repetition rates up to 600 Hz. In our experiments we utilized the copper ELV design that is suitable for cryogenic operation down to 10 K. The application of this valve will

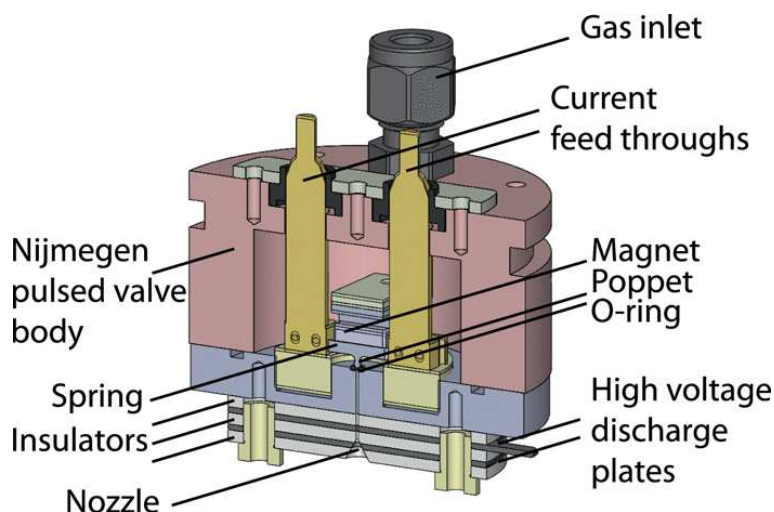


Figure 2.1: Schematic cross-section of a Nijmegen pulsed valve with discharge nozzle. The valve opening mechanism is based on the Lorentz force in an aluminium spring, situated between two strong permanent magnets. When a current is applied through the spring, it is pulled back together with the poppet that closes the O-ring, resulting in a short pulse of gas. An electrical discharge can be created in the nozzle between the stainless-steel plates that are separated by insulators. Reprinted with permission from the authors [75].

be discussed in chapter 4 and 6.

The NPV was designed with low-cost components and ease of manufacturing in mind. A schematic cross-section of this valve can be seen in Figure 2.1. The opening mechanism is based on the Lorentz force on a current-carrying strip of aluminium in a magnetic field. The aluminium strip is shaped such that it acts as a spring that closes the nozzle of the valve when no current is applied. Two permanent magnets are used to supply the magnetic field. The nozzle diameter at the base is $500 \mu\text{m}$, and ends in a 60° conical shape. The valve produces molecular beams with short pulse duration around $20 \mu\text{s}$ and low rotational temperature. This valve is used exclusively at room temperature, and is featured in chapter 5.

2.1.3 Discharge beam production

Many atoms or molecules that are used in our experiments are unstable or highly reactive, and need to be produced from stable precursors. Another possibility is that an atom or molecule cannot be manipulated in a multistage Zeeman decelerator in their ground state, and needs to be excited to a higher state. Particles

in a molecular beam can be excited from the ground state into an excited state via several methods such as inelastic collision with other molecules or atoms [76], electron-impact [77] or laser excitation. Alternatively, an electrical discharge can be used to excite the atoms or molecules. We chose this method for our experiments as it can be applied easily to many systems, whereas most other methods would require a specific configuration for each species. In addition, an electrical discharge can be used to dissociate molecules to create beams of fragment atoms or molecules. One downside of this all-purpose method is that many by-products are formed in the discharge, such as different states or fragments which are not desired in the molecular beam. However, most of these will filter out when using a multistage Zeeman decelerator, as will become clear in chapter 4.

An electrical discharge is created by applying a large electric field gradient (about 400 V/mm) in the expanding molecular beam. The discharge is created between two stainless-steel plates that are insulated from each other and the valve body by Macor plates. These plates are integrated in the pulsed valve design, directly after the valve mechanism. A cross section of a NPV design with such a modification can be seen in Figure 2.1. This type of design is referred to as a pinhole discharge, as the discharge occurs in a small hole in the plates through which the molecular beam expands [75]. A similar design has been implemented for the ELV. Since the discharge occurs before the complete expansion of the gas, any additional energy from the discharge in the form of rotational or translation energy will be carried off-axis due to collisions in the expanding gas. This results in beams of radicals or excited particles with the favorable characteristics of a regular supersonic beam. Part of the excess energy will also be converted to forward velocity of the beam. This effect is more pronounced in particles that inherently have a small amount of kinetic energy, as the relative change in velocity is larger.

Referring back to the valve cross section shown in Figure 2.1, the electrode closest to the valve mechanism is grounded to carry away the discharge current. The voltages applied to the front plate of the discharge is typically between -650 V and -850 V. The voltages are supplied in pulses of 30-50 μs duration, to limit heating of the valve and provide an accurate window in which the excited or radical species are made. Negative voltages are used on the front plate to ensure that the electrons flow against the direction of the expanding molecules or atoms and thus cause more collisions.

The discharge process is not inherently stable. Without assistance the discharge will not ignite instantly during every gas pulse. Higher voltages will make the discharge more likely to ignite, but will also result in more heating of the molecular beam. In addition, when the applied voltage is too high, the discharge type can change from the desired glow-type discharge to an arc discharge. In an arc discharge, the current that is pulled through the expanding gas is much larger than in a glow discharge, resulting in even hotter beams. In order to obtain a stable glow

discharge, a hot filament can be used near the valve. A current ranging from 2-3 A through a 0.3-mm-diameter tungsten wire will heat up the wire to an orange glow and cause electrons to escape. These free electrons can ignite the pulsed discharge reliably, at conditions below the arcing threshold.

2.2 The Zeeman effect

Atoms and molecules in quantum states that have a magnetic dipole moment will experience a shift of the corresponding energy levels when they enter a magnetic field, \vec{B} . This is a quantum mechanical effect, since the magnetic dipole moment is governed by the quantized orbital and spin moments of the particle. The effect was named after the Dutch physicist Pieter Zeeman, who in 1896 first measured the broadening and consequently the splitting of an absorption line in sodium due to the application of a magnetic field [78]. In the following subsections, the Zeeman effect is derived for helium in the metastable 3S_1 state, oxygen atoms in the 3P_2 state, and finally for oxygen molecules in the $X^3\Sigma_g^-$ state.

2.2.1 Zeeman energy in atoms

The Zeeman energy-level splitting of atoms in a magnetic field is calculated using an additional term to the field-free Hamiltonian. This added term contains all factors related to the magnetic field, and is called the Zeeman Hamiltonian. The Zeeman Hamiltonian for atoms contains terms for the contribution of the angular momentum (\vec{L}) and spin (\vec{S}) of the electrons, and the total nuclear spin (\vec{I}):

$$H_Z = \frac{\mu_B}{\hbar} \vec{L} \cdot \vec{B} + \frac{\mu_B g_e}{\hbar} \vec{S} \cdot \vec{B} + \frac{\mu_N g_N}{\hbar} \vec{I} \cdot \vec{B}. \quad (2.2)$$

In this equation μ_B is the Bohr magneton, \hbar the reduced Planck constant, g_e the electron g-factor equal to ≈ 2.00232 , μ_N the nuclear magneton and g_N the nuclear g-factor. The Bohr magneton is equal to $e\hbar/2m_e$, while the nuclear magneton equals $e\hbar/2m_p$, where e is the electron charge, m_e is the electron mass and m_p the proton mass. Since the proton-to-electron mass ratio is about 1836, the contribution of the nuclear spin to the total magnetic moment is negligible in cases where the orbital or spin moments are non-zero. The nuclear g-factors for the proton and the neutron are $g_p \approx 5.58569$ and $g_n \approx 3.82609$, respectively. The g-factors and the proton-electron mass ratio were obtained from the CODATA recommended values of 2014 [79].

In the following derivations, the z-axis is chosen along the direction of the magnetic field. Since the helium and oxygen atoms have zero total nuclear spin, the equation for the Hamiltonian can be rewritten as:

$$\hat{H}_Z = \frac{\mu_B}{\hbar} B_z (\hat{L}_z + g_e \hat{S}_z), \quad (2.3)$$

where \hat{L}_z and \hat{S}_z are operators on the basis-set of atomic wave functions with the following relations:

$$\hat{S}_z |m_S\rangle = \hbar m_S |m_S\rangle, \quad \hat{L}_z |m_L\rangle = \hbar m_L |m_L\rangle. \quad (2.4)$$

Here, the quantum numbers m_S and m_L represent the projections of S and L on the z-axis. The functions $|m_S\rangle$ and $|m_L\rangle$ represent the complete basis set of spin and orbital momentum wave functions, respectively.

Metastable helium

In the ground state helium (1S_0) has an electron configuration of $(1s)^2$ according to standard orbital notation. It has no unpaired electrons, zero orbital momentum, and zero total nuclear spin. Therefore it has zero magnetic moment and is unaffected by magnetic fields. Helium in the first excited state (3S_1) with electron configuration $(1s)(2s)$ has two unpaired spins and an extremely long lifetime of 7870 seconds [80]. The two electron spins can form a singlet or a triplet state, with the latter being lower in energy due to exchange interaction. This metastable helium state with a total spin of one has a magnetic moment of approximately two Bohr magnetons. Because $L = 0$, a complete spin-orbit basis set can be comprised of the three vectors that represent the m_S components -1, 0 and 1. The energy levels due to the Zeeman effect are calculated with the Zeeman Hamiltonian, represented as matrix elements that act on the wave functions:

$$\langle m'_S | \hat{H}_Z | m_S \rangle = g_e \mu_B B_Z \delta_{m'_S m_S} m_S. \quad (2.5)$$

The three energy levels corresponding to the eigenstates can be seen in Figure 2.2a as a function of the magnetic field strength. In this diagram, the metastable helium energy levels split up according to their m-states. Helium in the $m_S = 1$ state increases in energy when the magnetic field rises. These type of states are referred to as low-field-seeking (LFS) states, as particles in these states are accelerated toward regions of lower magnetic field strength. The opposite state, $m_S = -1$, shows a decreasing trend in energy at increasing magnetic field, and is referred to as a high-field-seeking (HFS) state. Finally, there is the neutral $m_S = 0$ state that is unaffected by magnetic field changes. As will be explained in section 2.3, the multistage Zeeman decelerator will be used to decelerate and focus exclusively LFS states, according to their magnetic-moment-to-mass ratios.

Oxygen atoms

Oxygen atoms have a ground-state electron configuration of $(1s)^2(2s)^2(2p)^4$, with the atomic term symbol 3P_2 . This atom has both a spin and orbital angular momentum of one. The total angular momentum is obtained with the well-known

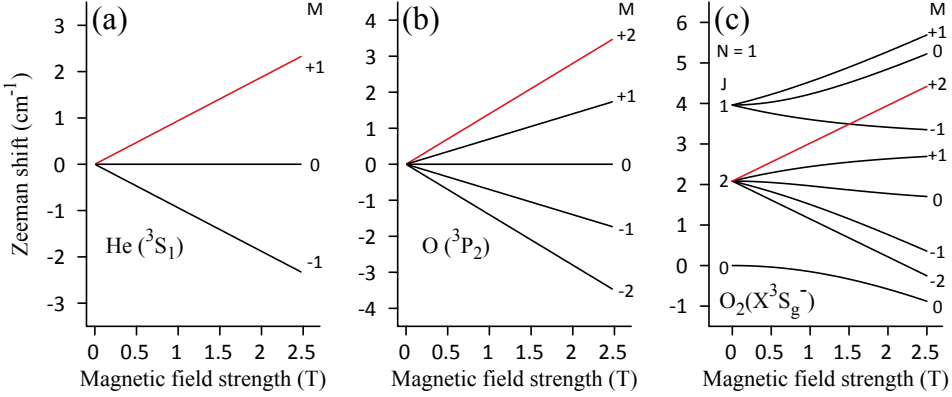


Figure 2.2: The Zeeman energy-level diagrams of (a) metastable He ($1s2s\ ^3S_1$), (b) O ($2p^4\ ^3P_2$) and (c) O₂ ($X^3\Sigma_g^-, N = 1$). The low-field-seeking states with the largest Zeeman shift are shown in red.

relation $\vec{J} = \vec{S} + \vec{L}$. In accordance with Hund's rules, the absolute ground state corresponds to the $J = 2$ spin-orbit state. Only this lowest-energy spin-orbit state is evaluated in the following calculations. The coupled basis set that is used to calculate the Zeeman energy levels of this state has the form of $|J = 2, m_J\rangle$. Here, m_J is the projection of the spin-orbit moment on the z-axis. In order to evaluate the operators in equation 2.3 using equation 2.4, a transformation matrix A is used to convert the uncoupled basis $|m_S, m_L\rangle$ (in the order $\{|-1, -1\rangle, |0, -1\rangle, |1, -1\rangle, |-1, 0\rangle, |0, 0\rangle, |1, 0\rangle, |-1, 1\rangle, |0, 1\rangle, |1, 1\rangle\}$ to the coupled basis $|J = 2, m_J\rangle$ for $m_J = -2, -1, 0, 1, 2$. The transformation matrix is comprised of the appropriate Clebsch-Gordan coefficients:

$$A = \begin{pmatrix} 1 & 0 & 0 & 0 & 0 & 0 & 0 & 0 & 0 \\ 0 & 1/\sqrt{2} & 0 & 1/\sqrt{2} & 0 & 0 & 0 & 0 & 0 \\ 0 & 0 & 1/\sqrt{6} & 0 & \sqrt{2/3} & 0 & 1/\sqrt{6} & 0 & 0 \\ 0 & 0 & 0 & 0 & 0 & 1/\sqrt{2} & 0 & 1/\sqrt{2} & 0 \\ 0 & 0 & 0 & 0 & 0 & 0 & 0 & 0 & 1 \end{pmatrix}. \quad (2.6)$$

The Hamiltonian operator that describes the Zeeman effect of the 3P_2 state of oxygen in the coupled basis set is given by:

$$A^T \hat{H}_Z A \approx \mu_B B_z \begin{pmatrix} -3 & 0 & 0 & 0 & 0 \\ 0 & -1.5 & 0 & 0 & 0 \\ 0 & 0 & 0 & 0 & 0 \\ 0 & 0 & 0 & 1.5 & 0 \\ 0 & 0 & 0 & 0 & 3 \end{pmatrix}, \quad (2.7)$$

where the approximation was made that $g_e \approx 2$. The Zeeman energy shifts of the five m_J levels correspond to the eigenvalues of this matrix, and can be seen as a function of the magnetic field strength in Figure 2.2b. Since it is a diagonal matrix, the eigenvalues are the diagonal elements and the Zeeman shift is linear. Because $J = 2$, there is a five-way splitting of the energy levels, with two LFS and two HFS states. The absolute magnetic moment of this state is three bohr magnetons. For the $J = 1$ state of oxygen there is a three-level splitting, with an absolute magnetic moment of 1.5 Bohr magnetons. Consequently, particles in the (${}^3P_1, m_J = 1$) state experience the same energy shift as particles in the (${}^3P_2, m_J = 1$) state.

2.2.2 Zeeman energy in diatomic molecules

In diatomic molecules an additional angular momentum is present, namely the end-over-end rotation of the molecules as a whole, denoted by the quantum number N . This angular momentum contributes to the magnetic dipole moment of the molecule. However, this work considers oxygen molecules, for which the contribution of the rotation to the total magnetic moment is four orders of magnitude less compared to the electron spin contribution. Another change in molecules compared to atoms is the manner in which the different angular momenta couple together. Prior to the evaluation of the Zeeman Hamiltonian, it is helpful to determine which angular momenta couple the strongest. The two most common coupling schemes are Hund's case (a) and (b) [81]. In case (a), both the spin and orbital angular momenta of the electrons are coupled to the internuclear axis, leading to strong spin-orbit coupling. The resulting vector is then coupled with the rotation of the molecule to form the total angular momentum \vec{J} . It should be noted that this definition of \vec{J} is different from the one in atoms. In Hund's coupling case (b), the spin-orbit coupling is weak or non-existent. In this case, the electronic orbital and rotational angular momenta are coupled first, after which the spin is added to form the total angular momentum. In the following calculations, the z-axis is again defined parallel to the magnetic field.

Oxygen molecules

The oxygen molecule is one of a few molecules that is magnetic in the ground state. The valence electron configuration is $(\pi^*2p)^2$ and the ground state is described by the term-symbol $X^3\Sigma_g^-$. The triplet-spin state is formed by the two electrons in the anti-bonding pi orbitals with parallel spins, as Hund's rules dictate. The most abundant isotopomer of oxygen, ${}^{16}\text{O}_2$, has a total nuclear spin $I = 0$. Because of this, the rest of the wave function of the oxygen molecule is symmetric under permutation of the identical nuclei. Since the triplet-spin state of the electrons is symmetric, the orbital part is anti-symmetric and the vibrational wave function is symmetric, only rotational modes that are anti-symmetric

($N = 1, 3, 5, \dots$) can be used to form the total molecular wave function. The electron spin couples to the rotational momentum of the molecules to form the total angular momentum $J = N - 1, N, N + 1$ for each rotational state. Due to the lack of orbital angular momentum, the coupling scheme can best be described in Hund's case (b). The matrix elements of the Zeeman Hamiltonian operator without orbital angular momentum are evaluated as follows:

$$\langle N', S', J', m'_J | \hat{H}_Z | N, S, J, m_J \rangle = g_e \mu_B B_z \delta_{SS'} \delta_{NN'} (-1)^{J+m_J+J'+N+S} \quad (2.8)$$

$$\sqrt{(2J+1)(2J'+1)S(S+1)(2S+1)} \begin{pmatrix} J & 1 & J' \\ m_J & 0 & -m'_J \end{pmatrix} \begin{Bmatrix} S & N & J' \\ J & 1 & S' \end{Bmatrix},$$

where Wigner 3-j and 6-j symbols represent the Clebsch-Gordon coefficients for the transformation between the uncoupled and the coupled basis sets. Only combinations of wave functions where $m_J = m_{J'}$ and $\Delta J = -1, 0, 1$ produce non-zero matrix elements, resulting in off-diagonal elements between different J -states. These off-diagonal elements form separate block-matrices for each m_J that can be solved individually. By diagonalizing these block matrices and calculating the eigenvalues, the Zeeman energy levels are found. For the first rotational manifold ($N = 1$) these energy levels as a function of magnetic field strength up to 2 T can be seen in Figure 2.2c. The off-diagonal terms result in an effective repulsion between energy levels with the same m_J . For example the $m_J = 0$ levels that would otherwise be neutral turn into LFS and HFS states due to their interaction between different J -levels. The state with the highest magnetic moment ($J = 2, m_J = 2$) does not experience any repulsion and remains linear with an effective magnetic moment of 2 Bohr magnetons. This state will be targeted in the experiments described in chapter 6. At magnetic fields above 7 T, different rotational manifolds will interfere and cause avoided crossings [82]. However, these magnetic field strengths are out of range for the Zeeman decelerator used in this work.

2.3 Multistage Zeeman deceleration

In order to perform scattering experiments with variable collision energy and high resolution, control over the velocity distributions of the colliding beams is required. A multistage Zeeman decelerator is used to manipulate the velocities of particles that have a magnetic dipole moment. As was seen in the previous section, particles with a magnetic dipole moment experience a Zeeman energy shift that is either HFS or LFS depending on the orientation of the dipole in the magnetic field. By using time-inhomogeneous magnetic fields, a non-conservative force can be applied to these paramagnetic particles, thus accelerating the particles in a particular direction. In a multistage Zeeman decelerator this is performed with a series of pulsed solenoids. In this section, we give a general description of the Zeeman

deceleration technique. The alternative operation principle of our decelerator is explained in chapter 3.

2.3.1 Longitudinal velocity manipulation

In a supersonic molecular beam, a forward mean velocity between 350 m/s and 2000 m/s is produced, depending on the temperature and molecules in the gas reservoir. These beams are created with a velocity spread between 10% and 20% of the mean beam speed. For a scattering experiment, additional control over the velocity distribution is desired. The goal here is two-fold: First, to make the mean velocity of the beam tunable in order to scan a range of collision energies. Second, to narrow the velocity spread and thus increase the collision-energy resolution. Both of these goals can be achieved by applying time-inhomogeneous magnetic fields to the atoms or molecules in a beam pulse.

Solenoids are used to produce pulsed magnetic fields in a molecular beamline, with the beam traveling through the centers of the solenoids. Figure 2.3 shows the magnetic field of a solenoid of 62 windings around a bore of 7-mm diameter running a current of 300 A. In this section, only the magnetic field on the beam axis is considered. In order to explain the concept of Zeeman deceleration, it is instructive to consider a single paramagnetic particle traveling along the beamline through a series of solenoids. Figure 2.4 is used to illustrate this process, which shows the potential energy as a function of the longitudinal position of a LFS particle. For this particle, the magnetic field in a solenoid can be interpreted as a potential energy hill. During the ascent the particle loses kinetic energy, which is converted into Zeeman potential energy. This same amount of energy is reverted back to kinetic energy as the particle descends the hill, and the forward velocity is restored. However, by switching off the solenoid field at some intervening time during the ascent, the particle loses kinetic energy permanently. This energy loss is shown in Figure 2.4 as ΔE_{kin} . In a multistage Zeeman decelerator this process is repeated many times in order to remove the desired amount of kinetic energy and thus lower the forward velocity of the particle. For the particle we considered so far, each solenoid is turned off at the exact same relative position on the potential energy curve. Assuming instantaneous switching times of the solenoids, this particle loses an equal amount of kinetic energy per stage, and is referred to as the synchronous particle [40, 58, 83].

The deceleration per solenoid is defined by the relative position of this synchronous particle at the moment of switching. The longitudinal position of a particle relative to the solenoid center is commonly referred to as the phase angle, ϕ . The relative scaling of this phase angle can be seen in Figure 2.5. Phase angle zero is found between two solenoids, while the solenoid centers are positioned at $-\pi/2$ and $\pi/2$. In this definition, the phase angle is periodic with period π . The

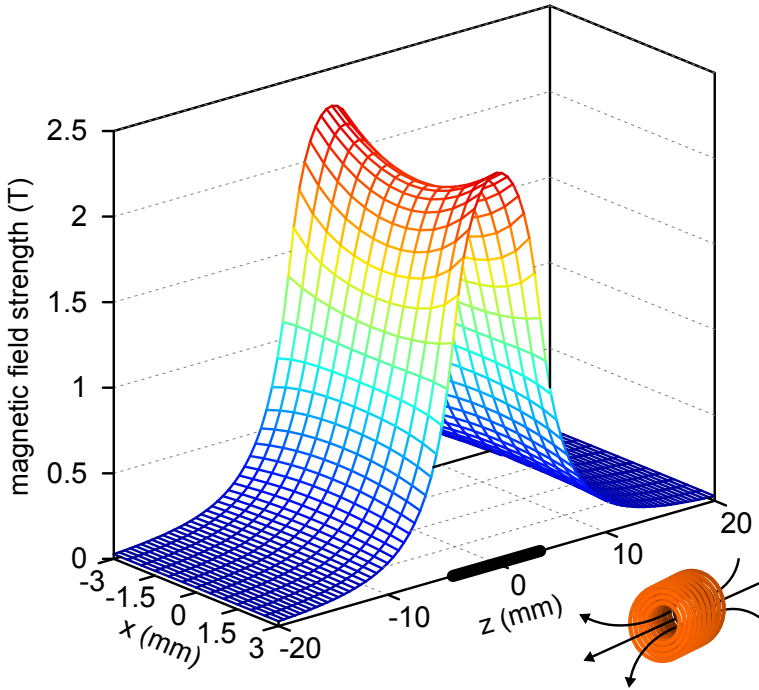


Figure 2.3: Magnetic field strength of a solenoid of 62 windings around a 7-mm-diameter bore running 300 A of current. The longitudinal (z) and transverse (x) coordinates are relative to the solenoid center. The size of the solenoid is shown on the z -axis with a black line. The solenoid in the bottom right corner shows the orientation of the solenoid and the direction of the magnetic field-lines when the current runs in counterclockwise direction.

phase angle of the synchronous particle at the moment of switching is called the equilibrium phase angle, ϕ_0 . When the equilibrium phase angle is increased towards $\pi/2$, the synchronous particle climbs more of the potential hill resulting in a larger amount of deceleration, and *visa versa* for smaller ϕ_0 . In this way, the synchronous particle is ultimately used as a tool to determine the switching times for the solenoids that result in the desired kinetic energy change.

This definition of the relative position in terms of a phase angle stems from the same concept used in multistage Stark deceleration [21, 84]. In the case of Stark deceleration this definition is more intuitive, as the potential landscape is inherently periodic, due to every other electrode being electronically connected. Detailed descriptions of the operation of a Stark decelerator can be found in other works [49, 50].

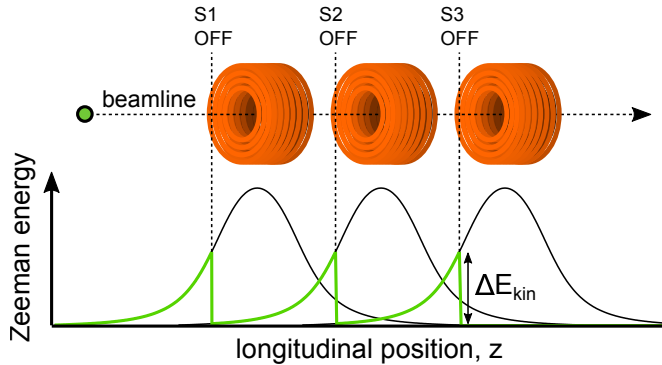


Figure 2.4: The Zeeman energy diagram of a synchronous LFS particle passing through a series of solenoids as a function of the longitudinal position. In this example, the solenoids S1, S2 and S3 are switched off instantaneously when the synchronous particle reaches the corresponding positions indicated by the vertical dashed lines. The complete Zeeman potential-energy curves inside the individual solenoids are shown in black, while the potential experienced by the synchronous particle is shown in green. The kinetic energy loss per solenoid is equal to ΔE_{kin} .

In an experiment a supersonic molecular beam is used that contains numerous particles, with a distribution of positions and velocities. The synchronous particle is typically chosen with a velocity close to the mean velocity of the molecular beam. When a solenoid field is switched off, particles that were behind the synchronous particle experienced less deceleration, while the opposite is true for particles that were ahead of the synchronous particle. The result is an effective focusing force relative to the synchronous particle in the longitudinal direction, i.e., over multiple deceleration stages, nearby non-synchronous particles will oscillate around the synchronous particle, forming a discrete packet. Particles that are too far ahead will no longer be focused towards the synchronous particle, as they regain kinetic energy from descending the potential hill before the fields are switched off, as can be seen in Figure 2.5. This effectively sets a limit to the longitudinal velocity range of particles that orbit the synchronous particle. The velocity spread is reduced when higher equilibrium phase angles are used, since non-synchronous particles require less spatial offset before they are accelerated away from the synchronous particle. The result is a molecular packet with a mean velocity that is tunable via the choice of ϕ_0 , and a narrow velocity spread, which is ideal in molecular scattering experiments.

The multistage Zeeman decelerator can also be utilized in an acceleration mode, by switching the solenoids on when the synchronous particle has passed

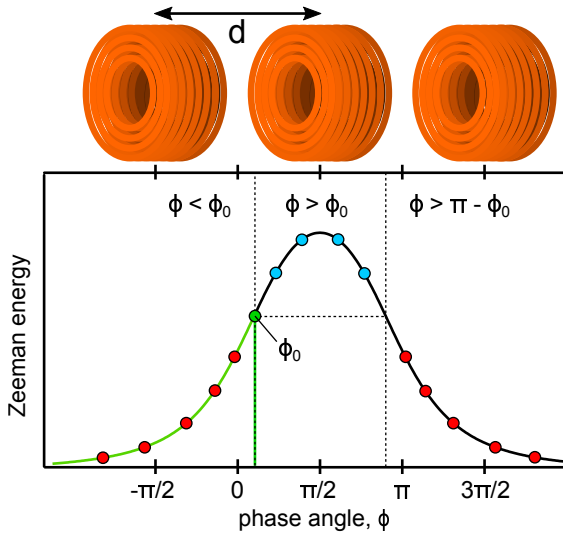


Figure 2.5: The Zeeman potential energy of LFS particles in a single active solenoid as a function of the phase angle, ϕ . The relative positions of the solenoid and its nearest neighbors are shown above the graph, with the distance d between them. The green part of the energy curve shows the Zeeman energy for the synchronous particle, and the switching position is indicated with the equilibrium phase angle, ϕ_0 . Red (blue) dots on the curve show non-synchronous particles that lose less (more) kinetic energy than the synchronous particle. Three zones are distinguished by the vertical dashed lines. Particles in the first two zones experience a relative acceleration towards the synchronous particle, while in the third zone particles are accelerated away from the synchronous particle.

the solenoid center. This switching mode also provides longitudinal velocity focusing near the synchronous particle, in a similar manner to the deceleration mode. However, this mode is rarely utilized as faster beams are more readily produced than slower beams by for example heating of the valve. In chapter 3 further utility of this acceleration mode is discussed and in chapter 4 a demonstration is given.

2.3.2 Transverse effects

In the previous section, only the longitudinal effects of the multistage Zeeman decelerator were discussed. In this section, the transverse motion of LFS particles in a Zeeman decelerator are considered. Since the solenoids have cylindrical symmetry, the transverse coordinates are considered as a single dimension.

In a solenoid magnetic field, there is only a small variation in the magnetic

field in the radial direction, compared to the longitudinal direction. As can be seen in Figure 2.3, this field is concave inside the solenoid, resulting in a focusing force for LFS particles. However, the magnetic field outside the solenoid is slightly convex resulting in a defocusing force. Since the magnetic field of a solenoid is always off when the particles pass through the center, the particles will experience on average the defocusing field more than the focusing field. Depending on the equilibrium phase angle used in the sequence, the average transverse force can result in very weak focusing or even slight defocusing of the molecular beam.

This effect of velocity focusing that depends on the equilibrium phase angle of the decelerator was investigated previously by Wiederkehr *et al.* [57]. It was found that optimal transmission was achieved when the equilibrium phase angle was around 40 degrees, i.e., when the particles traveled a moderate distance into the active solenoid before it was turned off. This result reveals a strong link between the longitudinal and transverse motions in this type of decelerator. It also shows that the number of transmitted particles rapidly drops at equilibrium phase angles that are too small, due to the transverse defocusing effect in the solenoids fringe fields. Because of these reasons, we decided to make a new type of multistage Zeeman decelerator, where the transverse and longitudinal motions are decoupled. In chapter 3 the new design concept is explained, and simulated results are shown that substantiate the concept.

2.4 Detection

Several methods exist to detect molecules or atoms in a vacuum. Some of these techniques rely on an ionization step to split neutral particles into an electron and a positive ion. These charged particles can be accelerated with electrostatics towards a measurement device, often with an amplification step to enhance the signal. In our experiments, we use microchannel plate (MCP) detectors to record and amplify the signal of ions and other energetic particles.

2.4.1 Microchannel plate detectors

MCP detection is based on the electron multiplier tube, a device in which one initial electron is converted into an avalanche of electrons through collisions with the tube walls. Since the amplification efficiency relies on the ratio of the tube width and height, the size of the tube can be scaled down to arbitrary size. By using a massive array of $\approx 10^6$ microscopic channels that act as electron multipliers, a compact detection plate is formed that can measure charged particles with high time resolution and little to no dead time. The signal can also be resolved spatially by reading out specific channels.

Modern MCP detectors are made of lead glass, a material that is optimized for emission of secondary electrons on collision with a primary electron. The channels are pulled from glass capillary and fused into a closely packed array. Each channel is typically a few tens of micrometers in diameter, and about 1 mm in length. They are created under a slight angle (a few degrees) to the normal of the plate surface in order to enhance collisions between the channel wall and incoming electrons. The front and back of the MCP are coated with a conducting material, which act as the input and output electrodes. In order to gain further amplification, two MCP plates can be mounted in a ‘Chevron’ configuration where the two plates have a 180 degree rotation to each other. The rotation between the two plates promotes more collisions with the channel walls, thus enhancing the amount of electron signal received. An even higher enhancement factor can be obtained with a ‘Z-stack’ configuration, where a third plate is added to the stack with another 180 degree rotation. For our experiments, a Chevron MCP detector (Jordan TOF products) was sufficient.

An electron avalanche can be initiated in a few different ways. It can be created by the impact of a charged particle, but also by an energetic photon (UV or X-RAY) or even a neutral atom with sufficient internal energy. For example, a metastable He atom such as described in section 4.2.2 has an internal energy of about 19.8 eV [85]. This is easily above the work function of lead glass at 5.4 eV [86]. When such an energetic atom hits the lead glass channel of the MCP, an electron avalanche is initiated, similar to a charged particle hitting the plate. This allows for detection of metastable helium beams without an ionization step. This technique will be used in the experimental setups described in chapter 4 and 5.

2.4.2 Particle ionization

Neutral atoms or molecules can be ionized by supplying sufficient energy for the most weakly bound electron to escape. This ionization energy (IE) differs per type of atom or molecule and is typically in the order of 5-25 eV. Energy can be supplied to a neutral particle for example by colliding it with a fast electron (electron impact ionization), collision with an electronically excited atom (Penning ionization) or by interaction with one or more photons (photoionization). The ionization efficiency with multiple photons can be increased by utilizing an excited energy level of the atom or molecule as an intermediate. This is called resonant enhanced multi-photon ionization (REMPI). Besides a high ionization efficiency, this technique has the advantage that it is quantum-state selective, though it does require a resonant transition with sufficient lifetime at a wavelength for which a laser can be produced with sufficient intensity.

For example, atomic oxygen in the triplet ground state ($2p^4 \ ^3P$) can be ionized using a REMPI scheme with three photons of the same color. This 2+1 REMPI

scheme requires two photons to reach the resonant state and a third photon to ionize it. The intermediate state ($2p^33p\ ^3P$) lies $\approx 88630\text{ cm}^{-1}$ above the ground state in energy, and therefore requires two photons of $\approx 44315\text{ cm}^{-1}$ in energy, which is $\approx 225.7\text{ nm}$ in wavelength. The first ionization energy of the oxygen atom is about 13.6 eV (109837 cm^{-1}), which is exceeded when a third photon is absorbed through the resonant state.

2.4.3 Data acquisition

As part of the experimental setup, a new data acquisition system was developed. This system had to be capable of controlling and reading out multiple hardware components with precise timings, and to be able to scan these timings while simultaneously measuring the resulting changes to the system. The data acquisition system was built using commercially available hardware components, while the software controlling these components was built using the (National Instruments) LabVIEW environment. This section will give a brief overview of the FullDAQ software and hardware components that were used in the experiments of this thesis.

In order to send out a sufficient number of triggers, a PulseBlaster (Spincore) is used to provide up to 24 programmable TTL level pulses. The PulseBlaster is capable of delivering these pulses with 10 ns precision using a 100 MHz internal clock frequency. The timings and their relative delay are completely software controlled, and can be changed in the downtime between two pulse sequences, at least when running at 10 Hz repetition rate. A digital oscilloscope (Picoscope 5444A) is used to measure BNC voltage signals. This oscilloscope has a minimum readout time step of 1 ns, when using a single channel, but up to four channels can be used simultaneously with 4 ns precision. Finally, an IDS camera (model UI-1240SE-M-GL) was interfaced to the program. This is a monochrome CMOS camera that has a 1280×1024 grid and a 1.31-MPix resolution. The camera was used in the experiments described in chapter 5 to measure the light from a phosphor screen attached to an MCP detector. This camera can also be used to complete a velocity map imaging (VMI) setup [87].

The software was built from the ground up, using interconnected modules to simultaneously scan and measure the signal with a variety of options. The main interface can be seen in Figure 2.6. This interface enables the user to control the 24-channel timing pulses. Each channel has a ‘start’ and ‘end’ timing, and each of these timings is set to a delay from a relative point in time that can either be time zero (t_0) or any of the other timings. In this way, any relations between the different pulse timings can be set.

The ‘SCOPE’ button opens a module where the user can control the digital oscilloscope. A hardware trigger can be set on any of the four channels, or on the dedicated external trigger channel. Data can be acquired with a high level of

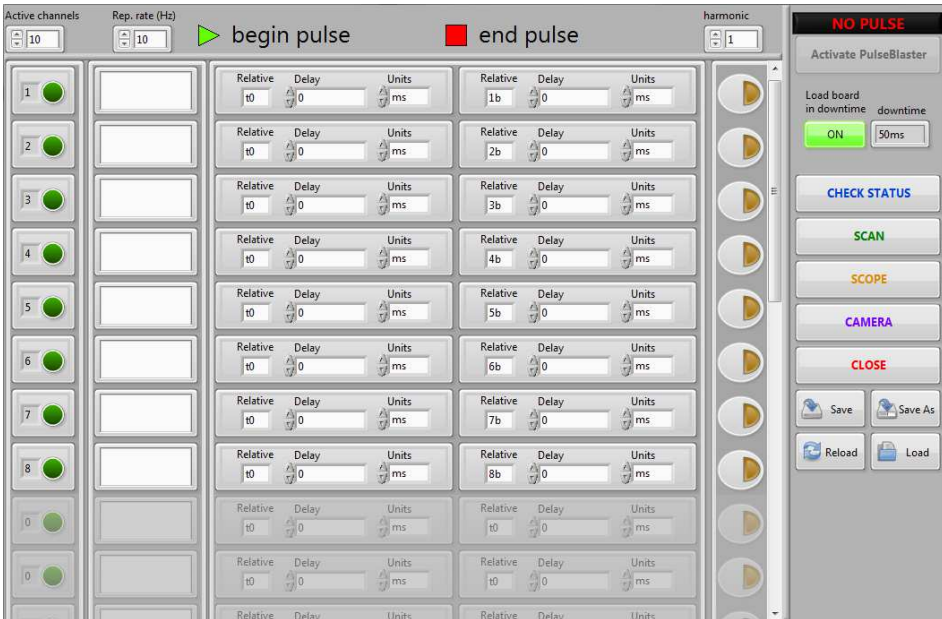


Figure 2.6: The main user interface of the FullDAQ software.

customizability, allowing the user to prioritize either enhanced timing or voltage accuracy. When acquiring data, either a single-shot mode or a running average over a set number of measurements can be used. Traces can be saved and used as a reference signal or exported for further analysis. In this module, the user can also set timing ‘gates’ in the graph, which represent for example a single peak in an ion mass spectrum. These gates are used to obtain integral signal during a scan.

The ‘CAMERA’ module contains an interface with the IDS camera. All the necessary camera parameters are controlled here, such as the trigger type, exposure time and refresh rate. After the camera has been set up, it can be used much in the same way as the oscilloscope. Individual images can be saved for further analysis, using a single shot, summing or event counting mode. The event counting mode uses the principle of signal centroiding [88] in order to pinpoint the exact position of an impinging ion on an MCP detector with phosphor screen. This measuring mode is used to count individual ion events from a phosphor screen, and is only effective when there is no overlap between ion signals. The spatial images measured in chapter 5 involved many overlapping atoms each shot. Therefore, summing mode was opted over the event counting mode. However, event counting

mode will be essential when measuring scattering distributions using VMI detection. More on this technique can be found in [87]. Within the camera image the user can define rectangular areas that fulfill a similar function to gates in the oscilloscope. These areas are used to accumulate data and construct a graph when scanning an experimental parameter.

The ‘SCAN’ module is used to scan a variety of experimental parameters. During one of these scans, either the oscilloscope gates or the camera rectangles are used to accumulate data for each step in the scan. Three types of scans are available. First, any of the 24-channel start or end timings can be used to scan the components controlled with the associated timing. For example, the arrival time of the detection laser relative to the pulsed valve can be scanned to obtain time-of-flight (TOF) profiles of the molecular beam. Second, a connection to a computer-controlled dye laser is made in order to scan the detection wavelength and measure a spectrum. And for the third scan type—in the final multistage Zeeman deceleration setup—an interface is made to the computer controlling the timing sequences of the solenoids. This allows us to scan the mean beam velocity and thus the collision energy in future scattering experiments. In this way, integral cross-sections of collision processes can be accurately measured without introducing additional inaccuracies due to calibration procedures. The three types of scans can be averaged over multiple passes in a continuous cycle, scanning the parameter back-and-forth, in order to mitigate any drifting effects during longer scans.

3

A new concept multistage Zeeman decelerator

While Zeeman decelerators provide excellent control over the longitudinal velocities in beams of paramagnetic particles, their control over the transverse velocities is limited due to the link between these two components. In order to gain independent control over the longitudinal and transverse motion, a new concept multistage Zeeman decelerator was developed. This chapter describes that concept and shows simulated results that reveal the six-dimensional phase-space distributions of packets of molecules that are transmitted through this decelerator.

Based on

Multistage Zeeman deceleration for molecular-scattering studies, T. Cremers, S. Chefdeville, N. Janssen, E. Sweers, S. Koot, P. Claus and S. Y. T. van de Meerakker, *Phys. Rev. A* **95**, 043415 (2017)

3.1 Introduction

Here, we describe a new concept for a multistage Zeeman decelerator that is optimized for applications in scattering experiments. The decelerator consists of an array of alternating magnetic hexapoles and solenoids, used to effectively decouple the longitudinal and transverse motions of the molecules inside the decelerator. We analyze in detail the performance of the decelerator using numerical trajectory calculations, and show that the decelerator exhibits phase stability, with a spatial and velocity acceptance that is much larger in the longitudinal than in the transverse directions. For this, we simulate decelerators of arbitrary length and use the NH ($X^3\Sigma^-$) radical as an example, as a possible target molecule for future scattering experiments. In the simulations, we use the field geometry as induced by the experimentally proven solenoid used in the Zeeman decelerator at ETH Zürich [57]. We show that the decelerator is able to both decelerate and accelerate, as well as to guide a packet of molecules through the decelerator at constant speed.

3

3.2 Zeeman decelerator concept

The multistage Zeeman decelerator we propose consists of a series of alternating hexapoles and solenoids, as is shown schematically in Figure 3.1. The lengths of the hexapoles and solenoids are almost identical. To simulate the magnetic field generated by the solenoids, we choose parameters that are similar to the ones used in the experiments by Wiederkehr *et al.* [57]. We assume a solenoid with a length of 7.5 mm, an inner and outer diameter of 7 and 11 mm, respectively, through which we run maximum currents of 300 A. Furthermore, we set the inner diameter to 3 mm for molecules to pass through. These solenoids can, for instance, be produced by winding enameled wire in multiple layers, and the current through these solenoids can be switched using commercially available high-current switches. With these levels of current, this solenoid can create a magnetic field strength on the molecular beam axis as shown in Figure 3.2a; the radial profiles of the field strength at a few positions z along the beam axis are shown in panel *b*. It is shown that the solenoid creates a concave field distribution near the center of the solenoid, whereas a mildly convex shape is produced outside the solenoid.

The hexapoles have a length of 8.0 mm, are separated by a distance $D = 4$ mm from the solenoids, and produce a magnetic field that is zero on the molecular beam axis but that increases quadratically as a function of the radial off-axis position r (see Figure 3.2c). We assume that the maximum magnetic field strength amounts to 0.5 T at a radial distance $r = 1.5$ mm from the beam axis. Such magnetic field strengths are readily produced by arrangements of current carrying

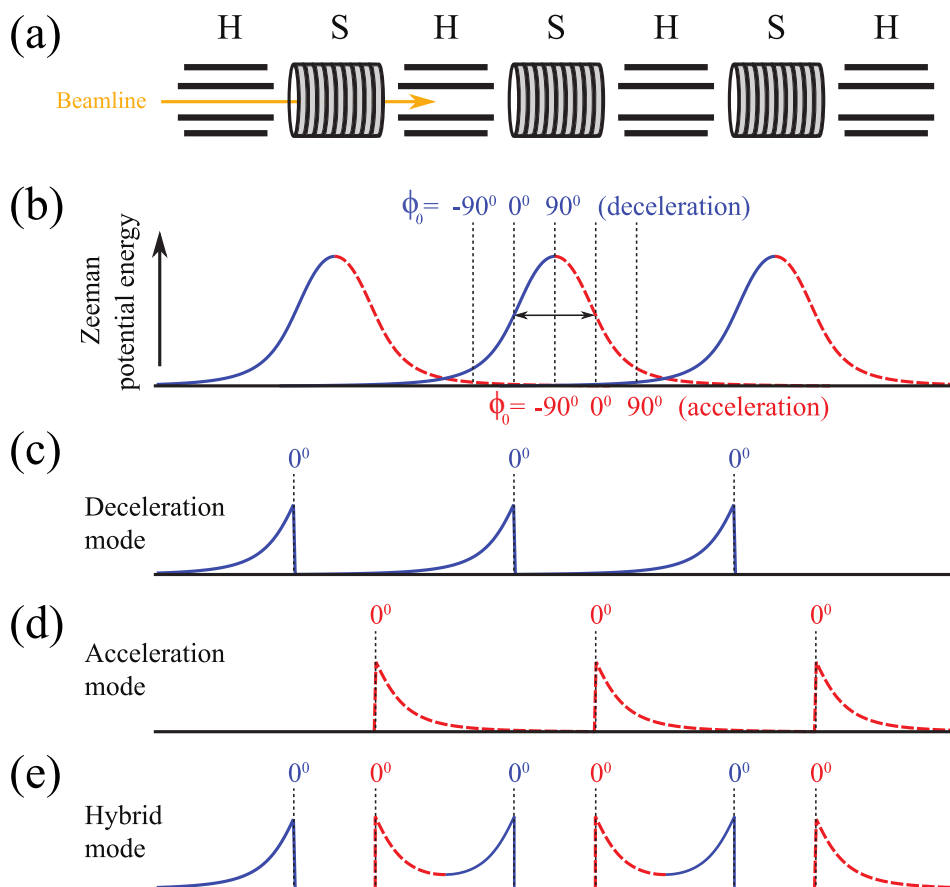


Figure 3.1: (a) Schematic representation of the array of alternating hexapoles (H) and solenoids (S). (b) Zeeman potential energy experienced by a low-field seeking molecule traveling along the beam axis for activated solenoids. The decelerator can be operated in a deceleration mode (c), an acceleration mode (d), and a hybrid mode (e). For each mode, the Zeeman energy experienced by the synchronous molecule is illustrated for $\phi_0 = 0^\circ$. Blue and red curves indicate the part of the potentials that decelerate and accelerate low-field seeking particles, respectively.

wires, permanent magnets [89, 90], or a combination of both [91].

The key idea behind this Zeeman decelerator concept is to effectively decouple the longitudinal and transverse motions of the molecules inside the decelerator. The fields generated by the solenoids are used to decelerate or accelerate the beam, but their mild transverse focusing and defocusing forces are almost negli-

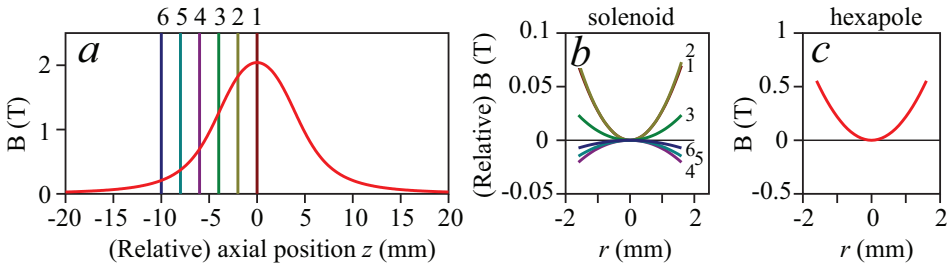


Figure 3.2: (a) On-axis magnetic field strength produced by a solenoid. (b) Radial field induced by the solenoid at various axial positions as indicated by the colored and numbered lines in panel a. (c) Radial field inside a hexapole.

ble compared to the strong focusing effects of the hexapoles. These hexapoles, in turn, hardly contribute to the longitudinal deceleration forces. As we will discuss more quantitatively in the next sections, this stabilizes molecular trajectories and results in phase stability.

Decelerators in which dedicated and spatially separated elements are used for transverse focusing and longitudinal deceleration have been considered before [48, 92]. In charged particle accelerators, such separation is common practice, and the detrimental effects of elements that affect simultaneously the longitudinal and transverse particle motions are well known [93]. The insertion of focusing elements between the mechanically coupled deceleration electrodes in a Stark decelerator appears technically impractical, however. By contrast, the relatively open structure of individually connected solenoids in a Zeeman decelerator allows for the easy addition of focusing elements. In addition, magnetic fields generated by adjacent elements are additive; shielding effects of nearby electrodes that are a common problem when designing electric field geometries do not occur.

The insertion of hexapoles further opens up the possibility to operate the Zeeman decelerator in three distinct modes that allow for either deceleration, acceleration, or guiding the molecular packet through the decelerator at constant speed. These operation modes are schematically illustrated in the lower half of Figure 3.1. In the description of the decelerator, we use the concepts of an equilibrium phase angle ϕ_0 and a synchronous molecule from the conventions used to describe Stark decelerators [21, 84]. The definition of ϕ_0 in each of the modes is illustrated in Figure 3.1. Because of the larger separation between solenoid centers, we had to change the definition of the phase angle positions. In this new definition, zero degrees is defined as the relative position along the beam axis where the magnetic field is at half the maximum strength. In deceleration mode, a solenoid is switched on before the synchronous molecule arrives in the solenoid, and switched off when the synchronous molecule has reached the position corresponding to ϕ_0 .

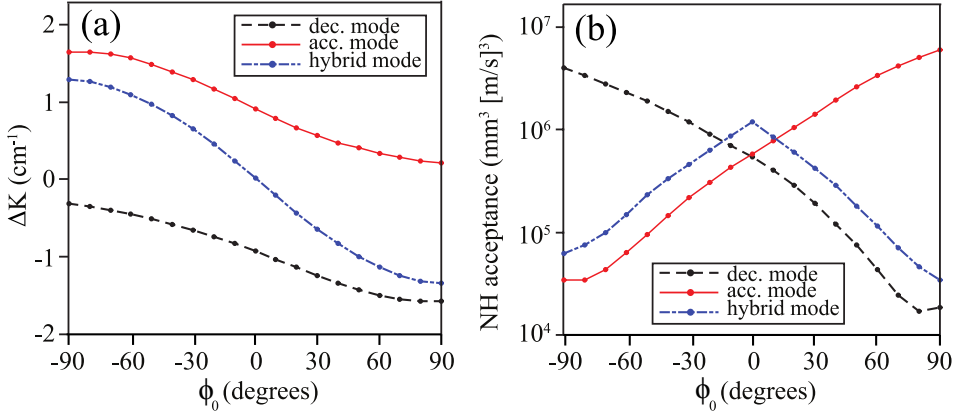


Figure 3.3: (a) Kinetic energy change ΔK per stage for a synchronous NH radical ($X^3\Sigma^-, N = 0, J = 1, M = 1$), if the decelerator is operated in deceleration, acceleration and in hybrid mode. (b) Corresponding 6D phase-space acceptances for NH radicals passing through a decelerator that consists of a suitable number of solenoids and hexapoles.

In acceleration mode, a solenoid is switched on when the synchronous molecules has reached the position corresponding to ϕ_0 , and it is only switched off when the synchronous molecule no longer experiences the field induced by the solenoid. In hybrid mode, two adjacent solenoids are simultaneously activated to create a symmetric potential in the longitudinal direction. For this, each solenoid is activated twice: once when the synchronous molecule approaches, and once when the synchronous molecule exits the solenoid, i.e., combining the deceleration and acceleration modes.

In this description we neglected the nonzero switching time of the currents in the solenoids. However, in reality the current pulses feature a rise time of about 8 μs . In the simulations, the full current profile is taken into account; we will adopt the convention that the current has reached half of the maximum value when the synchronous particle reaches the ϕ_0 position. This switching protocol ensures that in hybrid mode with $\phi_0 = 0^\circ$, the molecules will receive an equal amount of acceleration and deceleration, in analogy with operation of a Stark decelerator with $\phi_0 = 0^\circ$.

The kinetic energy change ΔK that the synchronous molecule experiences per stage is shown for each mode in Figure 3.3a. In this calculation we assume the NH radical in its electronic ground state, which has a $2\text{-}\mu_B$ magnetic dipole moment (*vide infra*). In the deceleration and acceleration modes, the full range of ϕ_0 (-90° to 90°) can be used to reduce and increase the kinetic energy, respectively. In hybrid mode, deceleration and acceleration are achieved for $0^\circ < \phi_0 \leq 90^\circ$ and

$-90^\circ \leq \phi_0 < 0^\circ$, respectively, whereas the packet is transported through the decelerator at constant speed for $\phi_0 = 0^\circ$. The maximum value for ΔK that can be achieved amounts to approximately 1.5 cm^{-1} .

3.2.1 Numerical trajectory simulations

The operation characteristics of the Zeeman decelerator are extensively tested using numerical trajectory simulations. In these simulations, it is essential to take the temporal profile of the current pulses into account. Unless stated otherwise, we assume single pulse profiles as illustrated in Figure 3.4a. The current pulses feature a rise time of approximately $8 \mu\text{s}$, then a variable hold-on time during which the current has a constant value of 300 A. The current exponentially decays to a lingering current of 15 A with a characteristic decay time of $5 \mu\text{s}$, as can be created by switching the current to a simple resistor in the electronic drive unit. This lingering current is introduced to prevent Majorana transitions, as will be explained in section 3.2.3. Furthermore, we assume that the hexapoles are always active when molecules are in their proximity.

In these simulations, we use NH radicals in the $X^3\Sigma^-$ ($N = 0, J = 1$) rotational ground state throughout. The Zeeman effect of this state is shown in Figure 3.4b. NH radicals in the low-field seeking $M = 1$ component possess a magnetic moment of $2 \mu_B$, and experience a linear Zeeman shift. NH radicals in this state have a relatively small mass-to-magnetic moment ratio of $7.5 \text{ amu}/\mu_B$, making NH a prime candidate for Zeeman deceleration experiments. Our findings are easily translated to other species by appropriate scaling of this ratio, in particular for species that also have a linear Zeeman shift (such as metastable helium, for instance).

The inherent 6D phase-space acceptance of the decelerator is investigated by uniformly filling a block-shaped area in 6D phase-space, and by propagating each molecule within this volume through a decelerator that consists of 100 solenoids and 100 hexapoles. In the range of negative ϕ_0 in deceleration mode and positive ϕ_0 for acceleration mode we instead used 200 pairs of solenoids and hexapoles to spatially separate the molecules within the phase stable area from the remainder of the distribution. This is explained in appendix B. The uniform distributions are produced using six unique Van der Corput sequences [94]. For each of the three operation modes, the resulting longitudinal phase-space distributions of the molecules in the last solenoid of the decelerator are shown in Figure 3.5 for three different ϕ_0 . The separatrices that follow from the 1D model for phase stability that explicitly takes the temporal profiles of the currents into account, as described in detail by Dulitz *et al.* [40], are given as a cyan overlay. For more details, see appendix A.

In each simulation, the synchronous molecule has an initial velocity chosen

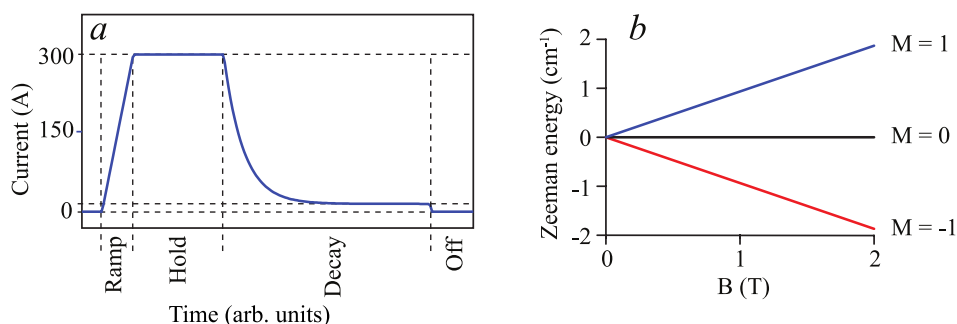


Figure 3.4: (a) Schematic representation of a single current pulse applied to a solenoid. (b) Zeeman energy diagram for NH radicals in the $X^3\Sigma^-, N=0, J=1$ rotational ground state.

such that the total flight time is approximately 4.8 ms. This results in velocity progressions of [370 \rightarrow 625], [390 \rightarrow 599] and [421 \rightarrow 568] m/s in acceleration mode with $\phi_0 = -60^\circ, -30^\circ$ and 0° , respectively; a progression of [445 \rightarrow 550], [500 \rightarrow 500] and [550 \rightarrow 447] m/s in hybrid mode with $\phi_0 = -30^\circ, 0^\circ$ and 30° ; and finally a progression of [570 \rightarrow 421], [595 \rightarrow 399] and [615 \rightarrow 383] m/s in deceleration mode corresponding to $\phi_0 = 0^\circ, 30^\circ$ and 60° .

It is shown that in all operation modes and for all values of ϕ_0 , the separatrices accurately describe the longitudinal acceptances of the decelerator. For larger values of $|\phi_0|$, the sizes of the separatrices are reduced, reflecting the smaller size and depth of the effective time-averaged potential wells. Note the symmetric shape of the separatrix when the decelerator is operated in hybrid mode with $\phi_0 = 0^\circ$, corresponding to guiding of the packet through the decelerator at constant speed. The transmitted particle density is slightly less in hybrid mode than in other modes, which indicates that the transverse acceptance is not completely independent of the solenoid fields. However, in each mode of operation the regions in phase-space accepted by the decelerator are homogeneously filled; no regions with a significantly reduced number of molecules are found. This is a strong indication that the decelerator indeed features phase stability.

The transverse acceptance is found to be rather independent of ϕ_0 , and is shown in Figure 3.6 for $\phi_0 = 0^\circ$ only. It can be seen that the transverse acceptance is typically smaller than the longitudinal acceptance, in accordance with our desideratum for molecular beam scattering experiments. Note that the transverse (velocity) acceptance can be modified independently from the deceleration and acceleration properties of the decelerator, simply by adjusting the field strength of the hexapoles.

Additionally, trajectory simulations can be used to quantify the overall 6D ac-

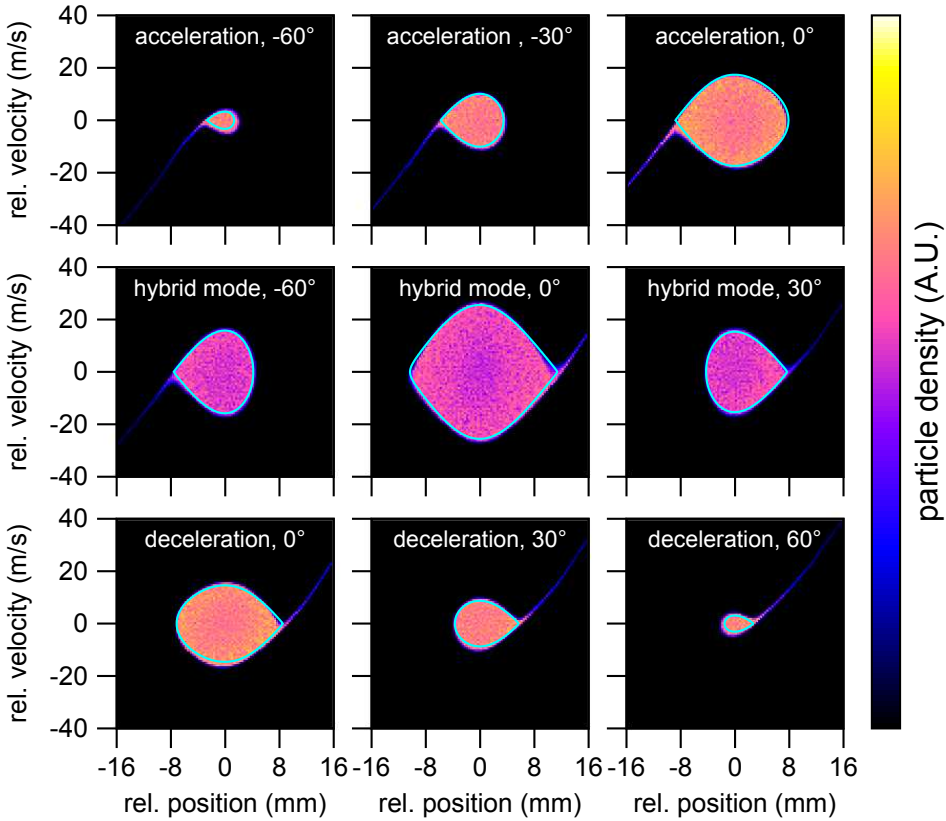


Figure 3.5: Longitudinal phase-space distributions of $\text{NH}(X^3\Sigma^-, N = 0, J = 1)$ in the final solenoid of the 100-stage decelerator when the decelerator is operated using different switching modes and values for ϕ_0 . These distributions result from 3D trajectory simulations of $5 \cdot 10^6$ particles. Positions and velocities are given relative to the synchronous particle. The same normalization was used for all graphs. The theoretical separatrices for each sequence are visible as cyan overlays.

ceptance of the decelerator. Because of the uniform initial distribution, all particles that are propagated represent a small but equal volume in phase-space. At the end of the decelerator, the particles within a predefined range with respect to the synchronous particle are counted, yielding the volume in phase-space occupied by these particles. In the simulations, the size of the initial 'block' distribution is increased until the relative number of counted particles reaches a maximum. We define the corresponding phase-space volume as the acceptance of the decelera-

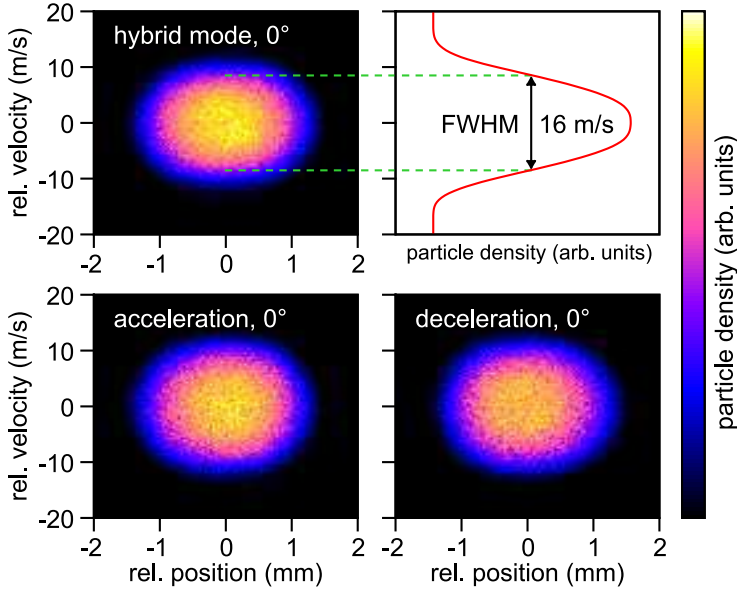


Figure 3.6: Transverse phase-space distributions that result from the same simulations used in Figure 3.5. The normalization is different for hybrid mode to compensate for the larger longitudinal acceptance. The top-right panel shows the transverse velocity profile for the hybrid mode, taken at the beam axis (0-mm transverse position).

tor. The resulting 6D acceptance is shown for each operation mode in panel *b* of Figure 3.3.

Operating in hybrid mode results in the typical triangle-shaped acceptance curve as a function of ϕ_0 that is also found for Stark decelerators. A maximum 6D phase-space acceptance of approximately $1.2 \cdot 10^6 \text{ mm}^3 (\text{m/s})^3$ is found for $\phi_0 = 0^\circ$, and it drops below $10^5 \text{ mm}^3 (\text{m/s})^3$ at large $|\phi_0|$. A peculiar effect is seen in the deceleration and acceleration modes for $\phi_0 < 0^\circ$ and $\phi_0 > 0^\circ$, respectively. Here, the acceptance largely exceeds the acceptance for $\phi_0 = 0^\circ$, and approaches values of $6 \cdot 10^6 \text{ mm}^3 (\text{m/s})^3$. This is a special consequence of the continuously acting focusing forces of the hexapoles, and will be discussed in more detail in appendix B.

Although one has to be careful to derive the merits of a decelerator from the 6D phase-space acceptance alone, it is instructive to compare these numbers to the phase-space acceptances found in other decelerators. Conceptually, the hybrid mode of our Zeeman decelerator is compared best to the $s = 3$ mode of a Stark decelerator. For the latter, Scharfenberg *et al.* found a maximum phase-space ac-

ceptance of $3 \cdot 10^5 \text{ mm}^3 (\text{m/s})^3$ for OH ($X^2\Pi_{3/2}, J = 3/2$) radicals, with a similar partitioning of this acceptance between the longitudinal and transverse coordinates as found here [50]. In comparison, for a multistage Zeeman decelerator without hexapoles, Wiederkehr *et al.* found that the 6D acceptance peaks at about $2 \cdot 10^3 \text{ mm}^3 (\text{m/s})^3$ for Ne (3P_2) atoms when equilibrium phase angles in the range 30° – 45° degrees are used [57]. The acceptance of the multistage Zeeman decelerator developed by Raizen and coworkers, also referred to as a magnetic coilgun, was reported to have an upper limit of $10^5 \text{ mm}^3 (\text{m/s})^3$ [22]. The highest 6D acceptances to date are found in traveling wave decelerators, mostly thanks to the large transverse acceptances of these decelerators. The maximum acceptance of the traveling wave Zeeman decelerator of Narevicius and coworkers, for instance, amounts to $2 \cdot 10^7 \text{ mm}^3 (\text{m/s})^3$ for Ne (3P_2) atoms [34].

3.2.2 Phase stability

The numerical trajectory simulations yield strong indications that the molecules are transported through the Zeeman decelerator without loss, i.e., phase stable operation is ensured. We support this conjecture further by considering the equation of motion for the transverse trajectories, using a model that was originally developed to investigate phase stability in Stark decelerators [47]. In this model, we consider a (nonsynchronous) molecule with initial longitudinal position z_i relative to the synchronous molecule, which oscillates in longitudinal phase-space around the synchronous molecule with longitudinal frequency ω_z . In other words, during this motion the relative longitudinal coordinate ϕ oscillates around the synchronous value ϕ_0 . In the transverse direction, the molecule oscillates around the beam axis with transverse frequency ω_r , which changes with ϕ . In Figure 3.7, the longitudinal and transverse oscillation frequencies are shown that are found when the Zeeman decelerator is operated in hybrid mode with $\phi_0 = 0^\circ$. For deceleration and acceleration modes rather similar frequencies are found (data not shown). It can be seen that the transverse oscillation frequency largely exceeds the longitudinal oscillation frequency. As we will show below, this eliminates the instabilities that has deteriorated the phase-space acceptance of multistage Stark and Zeeman decelerators in the past [47, 48, 57, 58].

During its motion, a molecule experiences a time-dependent transverse oscillation frequency that is given by [47]:

$$\omega_r(t) = \omega_0^2 - A \cos(2\omega_z t), \quad (3.1)$$

where ω_0 and A are constants that characterize the oscillatory function. The resulting transverse equation of motion is given by the Mathieu differential equation:

$$\frac{d^2 r}{d\tau^2} + [a - 2q \cos(2\tau)]r = 0, \quad (3.2)$$

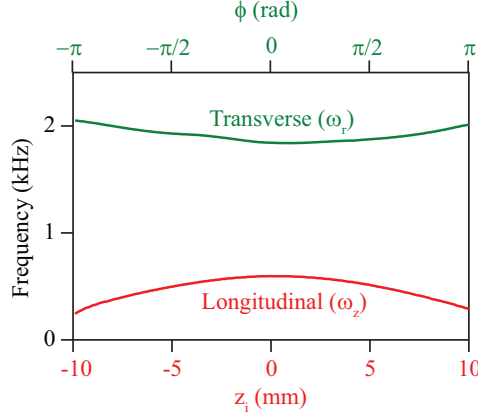


Figure 3.7: Transverse and longitudinal oscillation frequencies of an NH ($X^3\Sigma^-, N = 0, J = 1$) radical as a function of the initial longitudinal position z_i and phase ϕ , respectively. The Zeeman decelerator is assumed to operate in hybrid mode with $\phi_0 = 0^\circ$.

with:

$$a = \left(\frac{\omega_0}{\omega_z}\right)^2, \quad q = \frac{A}{2\omega_z^2}, \quad \tau = \omega_z t. \quad (3.3)$$

Depending on the values of a and q , the solution of this equation exhibits stable or unstable behavior. This is illustrated in Figure 3.8 that displays the Mathieu stability diagram. Stable and unstable solutions exist for combinations of a and q within the white and gray areas, respectively. For each operation mode of the decelerator, and for a given phase angle ϕ_0 , the values for the parameters a and q can be determined from the longitudinal and transverse oscillation frequencies of Figure 3.7. The resulting values for the parameters q and a as a function of z_i are shown in panel *a* and *b* of Figure 3.8, for the decelerator running in hybrid mode with $\phi_0 = 0^\circ$. The (a, q) combinations that govern the molecular trajectories for this operation mode are included as a solid red line in the stability diagram shown in panel *c*. Clearly, the red line circumvents all unstable regions, and only passes through the unavoidable 'vertical tongues' where they have negligible width. These narrow strips do not cause unstable behavior for decelerators of realistic length. The unstable areas in the Mathieu diagram are avoided because of the high values of the parameter a . This same result was found for the other operation modes and equilibrium phase angles. We thus conclude that the insertion of hexapoles effectively decouples the transverse motion from the longitudinal motion; the Zeeman decelerator we propose is inherently phase stable, and can in principle be realized with arbitrary length.

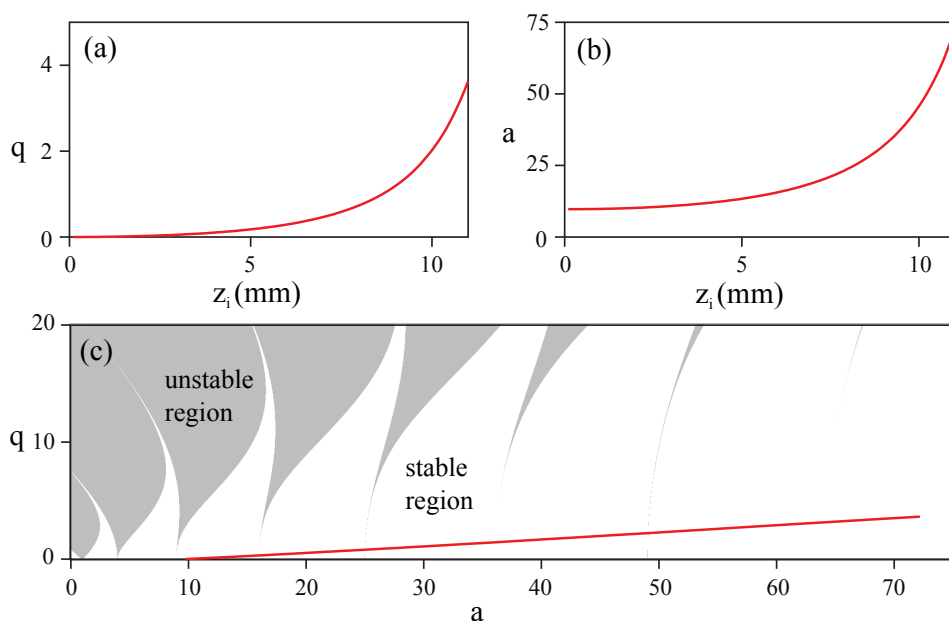


Figure 3.8: Values for the parameters q (panel a) and a (panel b) for a nonsynchronous molecule as a function of the initial longitudinal position z_i if the decelerator is operated in hybrid mode with $\phi_0 = 0^\circ$. The red curve in the Mathieu stability diagram (panel c) characterizes the stability of the resulting trajectories. Based on the coupled equations of motion, trajectories are stable or unstable within the white or grey areas, respectively.

3.2.3 Prevention of Majorana losses

An important requirement in devices that control the motion of molecules using externally applied fields, is that the molecules remain in a given quantum state as they spend time in the device. As the field strength approaches zero, different quantum states may become (almost) energetically degenerate, resulting in a possibility for nonadiabatic transitions. This may lead to loss of particles, which is often referred to as Majorana losses.

The occurrence of nonadiabatic transitions has been studied extensively for neutral molecules in electric traps [95], as well as for miniaturized Stark decelerators integrated on a chip [96]. Tarbutt and coworkers developed a theoretical model based on the time-dependent Hamiltonian for the field-molecule interaction, and quantitatively investigated the transition probability as the field strength comes close to zero, and/or if the field vector rotates quickly relative to the decelerated particles [97].

In the multistage Zeeman decelerators that are currently operational, losses

due to nonadiabatic transitions can play a significant role [30]. Specifically, when switching off a solenoid right as the particle bunch is near the solenoid center, there will be a moment in time where no well-defined magnetic quantization field is present. In previous multistage Zeeman decelerator designs, this was compensated by introducing a temporal overlap between the current pulses of adjacent solenoids, effectively eliminating nonadiabatic transitions [30]. In the Zeeman decelerator concept presented in this manuscript, this solution is not available, since adjacent solenoids are separated by hexapole elements. The hexapoles induce only marginal fringe fields, and do not contribute any magnetic field strength on the molecular beam axis.

Referring back to Figure 3.4a, we introduce a quantization field throughout the hexapole-solenoid array by switching each solenoid to a low-level lingering current when the high current pulse is switched off. Since the fringe field of a solenoid extends beyond the geometric center of adjacent hexapoles, and since in the center of the solenoid the maximum magnetic field per unit of current is created, a lingering current of approximately 15 A is sufficient to provide a minimum quantization field of 0.1 T. The resulting sequences of current profiles through the solenoids with number n , $n + 1$ and $n + 2$ are shown in the upper half of Figure 3.9 for the deceleration (panel a) and hybrid modes (panel b). The profiles for acceleration mode are not shown here, but they feature the low current before switching to full current, instead of a low current after. The lingering current exponentially decays to its final value, and lasts until the next solenoid is switched off. In panels c and d the corresponding magnetic field strength is shown that is experienced by the synchronous molecule as it propagates through the decelerator (blue curves), together with the field that would have resulted if the solenoid were switched off with a conventional ramp time (red curves). Clearly, the low level current effectively eliminates the zero-field regions.

From model calculations similar to the ones developed by Tarbutt and coworkers [97], we expect that the magnetic field vector inside the solenoids will not rotate fast enough to induce nonadiabatic transitions, provided that all solenoid fields are oriented in the same direction. We therefore conclude that the probability for nonadiabatic transitions is expected to be negligible for the Zeeman decelerator concept proposed here.

One may wonder how the addition of the slowly decaying lingering current affects the ability to efficiently accelerate or decelerate the molecules. This is illustrated in panels e and f of Figure 3.9 that displays the acceleration rate experienced by the synchronous molecule. The acceleration follows from $-(\vec{\nabla}U_Z)/m$, where U_Z is the Zeeman energy for NH ($X^3\Sigma^-, N = 0, J = 1, M = 1$) induced by the time-varying magnetic field $B(T)$, and m is the mass of the NH radical. It is seen that the lingering current only marginally affects the acceleration force; a slight additional deceleration at early times is compensated by a small acceleration

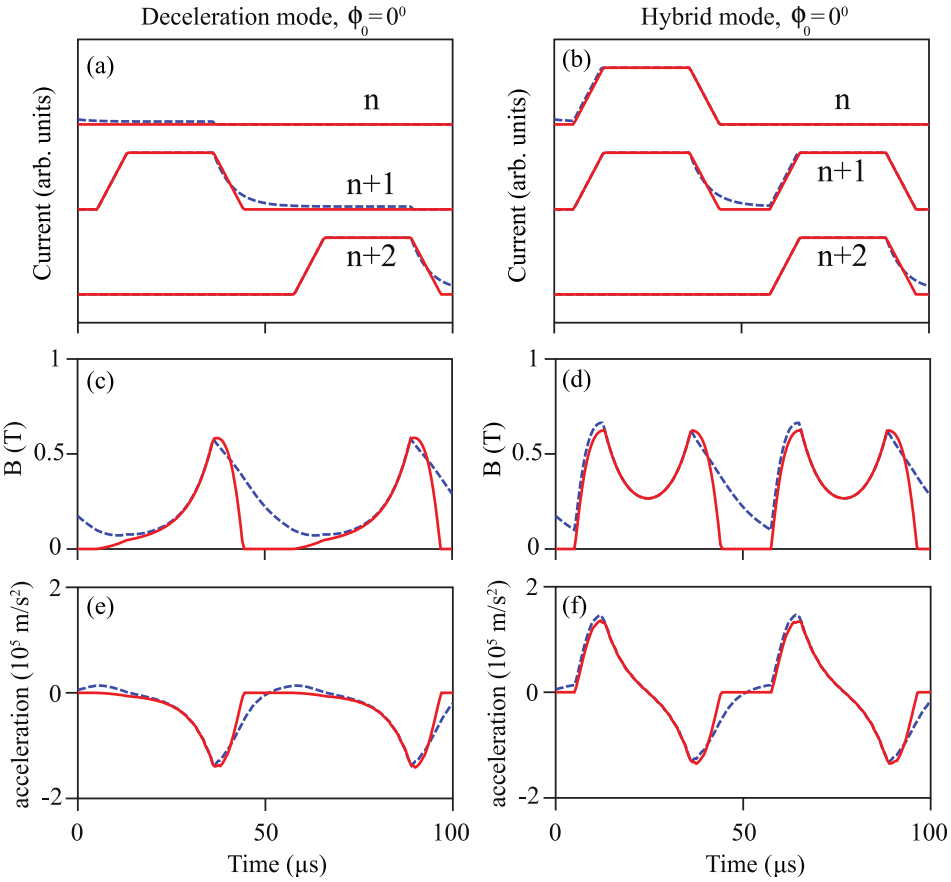


Figure 3.9: Schematic representation of the switching protocol, when the Zeeman decelerator is operated in deceleration mode (left) and hybrid mode (right) with $\phi_0 = 0^\circ$. (a,b) Sequence of current pulses applied to adjacent solenoids, using conventional ramp down profiles (red curves) or using a lingering decaying current (blue curves). (c,d) Magnetic field strength experienced by the synchronous molecule as a function of time induced by the sequence of current pulses. (e,f) Resulting acceleration of the synchronous molecule as a function of time.

when the synchronous molecule exits the solenoid. Overall, the resulting values for ΔK with or without lingering current, as obtained by integrating the curves in panels e and f, are almost identical (data not shown).

3.2.4 Excessive focusing at low velocities

A common problem in multistage decelerators is the occurrence of losses due to excessive focusing at low forward velocities. This effect has been studied and observed in multistage Stark decelerators that operate in the $s = 1$ or $s = 3$ modes, where losses occur below approximately 50 or 150 m/s, respectively [48, 50]. Our concept for a multistage Zeeman decelerator shares these over-focusing effects at low final velocities, which may be considered a disadvantage over traveling wave decelerators, which are phase stable down to near-zero velocities.

At relatively high velocities, the hexapole focusing forces can be seen as a continuously acting averaged force, keeping the molecules confined to the beam axis. However, at low velocities this approximation is no longer valid, and the molecules can drift from the beam axis between adjacent hexapoles. We investigate the expected losses using similar numerical trajectory simulations as discussed in section 3.2.1, i.e., we again assume a Zeeman decelerator consisting of 100 hexapole-solenoid pairs. We assume packets of molecules with five different mean initial velocities ranging between $v_{\text{in}} = 350$ m/s and 550 m/s, and these packets are subsequently propagated through the decelerator. The decelerator is operated in hybrid mode, and used with different values for ϕ_0 . Since we assume a 100-stage decelerator throughout, the packets emerge from the decelerator with different final velocities.

In Figure 3.10 we show the number of decelerated particles that are expected at the end of the decelerator as a function of ϕ_0 (panel *a*), or as a function of the final velocity (panel *b*). For low values of ϕ_0 , the transmitted number of molecules is (almost) equal for all curves; the slightly higher transmission for higher values of v_{in} is related to the shorter flight time of the molecules in the decelerator. Consequently, molecules that are not within the inherent 6D phase-space acceptance of the decelerator can still make it to the end of the decelerator, and are counted in the simulations. For higher values of ϕ_0 , the transmitted number of molecules decreases, reflecting the reduction of the phase-space acceptance for these phase angles. This is particularly clear for the blue and green curves ($v_{\text{in}} = 550$ and 500 m/s, respectively), which follow the 6D phase-space acceptance curve from Figure 3.3*b*. The three other curves feature a drop in transmission that occurs when the velocity drops below approximately 160 m/s, as is indicated by the dashed vertical lines. Obviously, for lower values of v_{in} , this velocity is reached at lower values of ϕ_0 (see panel *a*).

The production of final velocities below this drop-off velocity is not a prime requirement in crossed-beam scattering experiments, as the collision energy is determined by the velocities of both beams and the crossing angle between the beams. Very low collision energies can be reached using small crossing angles, relaxing the requirements on the final velocities of the reagent beams. For these applications we therefore see no direct need to combat these over-focusing effects.

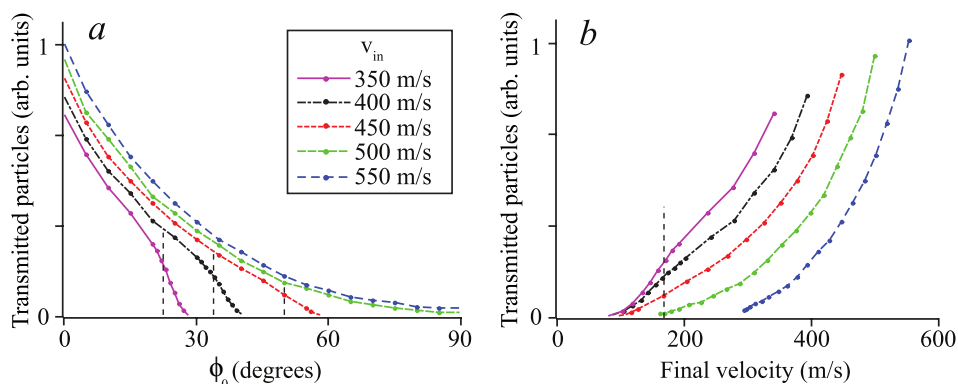


Figure 3.10: Simulated number of transmitted NH radicals that pass through a 100 hexapole-solenoid-pair Zeeman decelerator operating in hybrid mode, as a function of ϕ_0 (a) and as a function of the final velocity (b). Packets of NH are used with a mean initial velocity ranging between 350 m/s and 550 m/s.

However, there are several promising options to mitigate these effects if desired. The first option is to employ hexapoles with a tunable strength, such that the transverse oscillation frequency can be modulated along with the decreasing velocity of the molecular packet. Similarly, permanent hexapoles with different magnetization can be installed to modify the focusing properties. Finally, it appears possible to merge a hexapole and solenoid into a single element, by superimposing a hexapole arrangement on the outer diameter of the solenoid. Although technically more challenging, this approach will provide an almost continuously acting transverse focusing force, while keeping the possibility to apply current pulses to the solenoids. Preliminary trajectory simulations suggest that indeed a significant improvement can be achieved, but the validity of these approaches will need to be investigated further if near-zero final velocities are required.

3.3 Conclusions and Outlook

In this chapter we introduced a new type of multistage Zeeman decelerator that is specifically optimized for crossed-beam scattering experiments. The decelerator consists of an array of alternating solenoids and hexapoles, that effectively decouples the longitudinal deceleration and transverse focusing forces. This ensures that phase-stable operation of the decelerator is possible over a wide range of velocities. For applications in scattering experiments, this decelerator concept has a number of advantages over existing and experimentally demonstrated Zeeman decelerators. The decelerator can be operated in three distinct modes that

make either acceleration, deceleration, or guiding at constant speed possible, enabling the production of molecular packets with a continuously tunable velocity over a wide range of final velocities. Phase stability ensures that molecules can be transported through the decelerator with minimal loss, resulting in relatively high overall 6D phase-space acceptance. Most importantly, this acceptance is distributed unequally between the longitudinal and transverse directions. Both the spatial and velocity acceptances are much larger in the longitudinal than in the transverse directions, which meets the requirements for beam distributions in scattering experiments in an optimal way.

At low final velocities, however, losses due to over-focusing occur. In crossed-beam scattering experiments this appears inconsequential, but for trapping experiments—where low final velocities are essential—the use of the concept presented here should be carefully considered. We have discussed various promising options for combating these losses using alternative hexapole designs in the last section of the decelerator. Additionally, Zhang *et al.* proposed a new operation scheme in a Stark decelerator that optimizes the transmitted particle numbers and velocity distributions, which could potentially be translated to a Zeeman decelerator [98]. The validity of these approaches will need to be investigated further, especially if near-zero final velocities are required.

4

Multistage Zeeman deceleration of metastable helium

This chapter describes a 24-stage prototype Zeeman decelerator following the concept described in the previous chapter. The decelerator incorporates a new solenoid design that consists of copper capillary. This chapter describes the characterization of this prototype, performed with beams of metastable helium. The decelerator was operated in acceleration, deceleration and hybrid modes that were described in the previous chapter. Measured and simulated profiles are compared and show an excellent agreement.

Based on

Multistage Zeeman deceleration for molecular-scattering studies, T. Cremers, S. Chefdeville, N. Janssen, E. Sweers, S. Koot, P. Claus and S. Y. T. van de Meerakker, *Phys. Rev. A* **95**, 043415 (2017)

4.1 Introduction

This chapter describes in a proof-of-principle experiment the successful implementation of the concept described in the previous chapter using a Zeeman decelerator consisting of an array of 25 hexapoles and 24 solenoids. The performance of the decelerator in acceleration, deceleration and hybrid modes is characterized using beams of metastable Helium (3S) atoms. This particle was chosen because it can readily be produced with an already tunable initial velocity, and full time-of-flight profiles can be measured easily with an MCP detector.

In the decelerator presented here, we use copper capillary material in a new type of solenoid that allows for direct contact of the solenoid material with cooling liquid. The solenoid is placed inside vacuum, while offering excellent thermal properties and allowing the use of low-voltage electronic components that are readily available and cost effective. Assemblies of permanent magnets are used to form the hexapole elements. Together, this results in a multistage Zeeman decelerator that is relatively easy and cheap to build, and that can be operated at repetition rates up to 10 Hz.

4.2 Experimental

4.2.1 Multistage Zeeman decelerator

An overview of the experiment is shown in Figure 4.1. The generation and detection of the metastable helium beam will be discussed in section 4.2.2; in this section we will first describe the mechanical design of the prototype, starting with a description of the solenoids and associated electronics.

An essential part in a multistage Zeeman decelerator is the design of the deceleration solenoids, and the cooling strategy to remove the dissipated energy. A variety of solenoid designs have been implemented successfully in multistage Zeeman decelerators before. Merkt and coworkers utilized tightly-wound solenoids of insulated copper wire that were thermally connected to water-cooled ceramics [29]. Later, similar solenoids were placed outside a vacuum tube, and submerged in a bath of cooling water [99]. This improved the cooling capacity, and enabled the experiment to operate at repetition rates of 10 Hz. Raizen and coworkers also developed a multistage Zeeman decelerator, referred to as the atomic or molecular coilgun, that is based on solenoids encased in high permeability material to increase the on-axis maximum magnetic field strength [32, 36]. Recently, different types of traveling wave Zeeman decelerators have been developed, which consist of numerous spatially overlapping quadrupole solenoids [34], or a helical wire arrangement to produce the desired magnetic field [38].

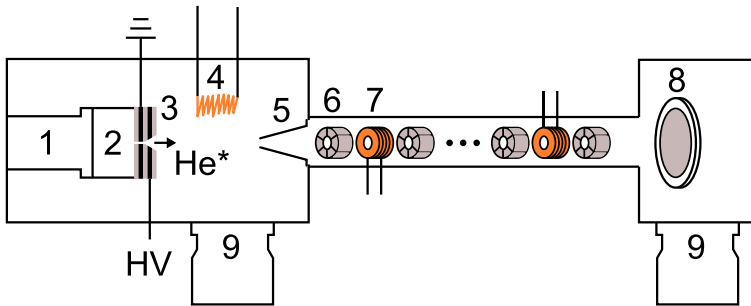


Figure 4.1: Schematic representation of the experimental setup. The main components are: 1, coldhead; 2, Even-Lavie valve; 3, pinhole discharge; 4, hot filament; 5, skimmer; 6, hexapole; 7, solenoid; 8, MCP detector; 9, turbo-molecular pump

In the decelerator presented here, we use a new type of solenoid that is placed inside vacuum, but that allows for direct contact of the solenoid material with cooling liquid. The solenoids consist of 4.5 windings of a copper capillary that is wound around a 3-mm bore diameter. The capillary has an inner diameter of 0.6 mm and an outer diameter of 1.5 mm, and cooling liquid is circulated directly through the capillary. The solenoid is wound such that the first and last windings end with a straight section of the capillary, as is shown in a photograph of a single solenoid in Figure 4.2*b*. These straight sections are glued into an aluminium mounting flange, as will be further discussed later. The inherent magnetic field profile generated by this solenoid is very similar to the solenoids as used in the simulations presented in chapter 3.

The use of a single layer of rather thick copper capillary as solenoid material in a Zeeman decelerator is unconventional, but it has some definite advantages. Because of the low-resistance copper capillary, small operating voltages (24 V) are sufficient to generate currents of approximately 4.5 kA that produce a maximum field of 2.2 T on the solenoid axis. This in turn allows for the use of FET-based electronics components to switch these currents, which are considerably cheaper than their high voltage IGBT-based counterparts. The same holds for the power supplies that deliver the current. By running cooling liquid directly through the solenoid capillary, the solenoids are efficiently cooled. The low operation voltage ensures that the cooling liquid does not conduct any significant electricity.

The current pulses are provided by specially designed printed-circuit boards (PCBs). Each solenoid is connected to a single PCB, that is mounted directly onto the solenoid-flange feedthroughs in order to minimize power loss between board and solenoid. Because of the change to the solenoid design, much higher currents are required to produce the same magnetic field strength as the original solenoid design used in the development of the concept. The attached PCBs are therefore

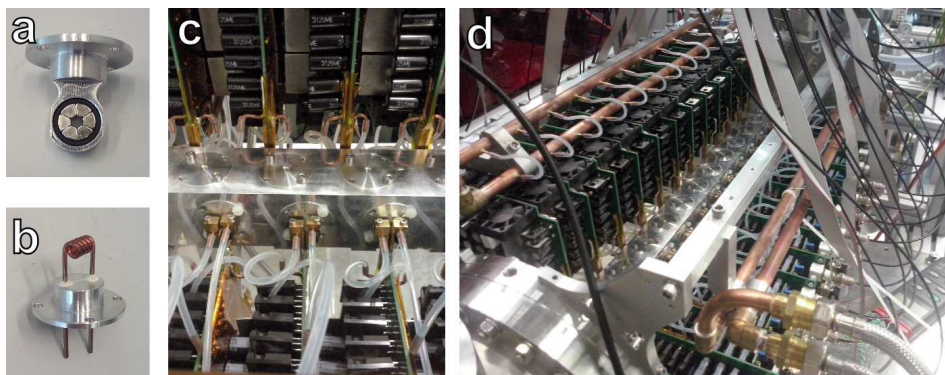


Figure 4.2: Photographs of the prototype Zeeman decelerator and the most relevant components. (a) a hexapole element embedded in a custom flange; (b) a solenoid element with connections through a custom flange; (c) close-up of the decelerator housing; (d) an overview of the decelerator.

designed to generate a maximum current of about 4.5 kA, which is enough to produce around a 2.2-T field in the solenoid. The electronics are able to apply up to two consecutive pulses to each solenoid, as is required for the hybrid mode of operation. While the low number of windings in the new solenoid severely reduces the self-inductance, the rise and fall times of the currents are still significantly longer, due to the high current requirement. After a deceleration pulse, a low-level lingering current of about 150 A is maintained in the solenoid to prevent Majorana transitions (see section 3.2.3), providing a quantization field for atoms or molecules that are near the solenoid. When calculating the solenoid time sequence, these current profile have to be matched accurately in order to calculate the correct timings. A more detailed look into the current profiles is given in the next chapter, where we discuss the finalized design of our multistage Zeeman decelerator.

The magnetic hexapoles consist of six wedge-shaped permanent magnets in a ring, as seen in Figure 4.2a. Adjacent magnets in the ring have opposite radial magnetization. The inner diameter of the hexapole is 3 mm and the length is 8 mm, such that these dimensions match approximately to the corresponding solenoid dimensions. The magnets used in this experiment are based on NdFeB (grade N42SH) with a remanence of approximately 450 mT. The advantage of using hexapoles consisting of permanent magnets is twofold: first, the implementation is mechanically straightforward, and second, no additional electronics are needed to generate the focusing fields. However, this approach lacks any tunability of the field strength. This can in part be overcome by selectively remov-

ing hexapoles from the decelerator, or by exchanging the magnets for ones with a different magnetization. If required, electromagnetic hexapoles that allow for tunability of the field strength can be used instead. We have built and successfully operated hexapoles that are made of the solenoid capillary material, and could optimize their focusing strength by simply adjusting the time these hexapoles are switched on. However, we found that similar beam densities were achieved using the permanent hexapoles, and experiments with electromagnetic hexapoles are not further discussed here.

The decelerator contains 24 solenoids and 25 hexapoles that are placed with a center-to-center distance of 11 mm inside a vacuum chamber. The chamber consists of a hollow aluminium block of length 600 mm with a squared cross section of side lengths 40 mm. This chamber is made by machining the sides of standard aluminium pipe material with an inner diameter of 20 mm. Solenoids and hexapoles are mounted on separate flanges, as can be seen in Figure 4.2, such that each element can be installed or removed separately. The first and last element of the decelerator is a hexapole to provide transverse focusing forces at the entrance and exit of the decelerator, respectively. Openings for the individual flanges on the decelerator housing spiral along the sides between subsequent elements, with clockwise 90 degree rotations. In this way there is enough space on each side of the decelerator to accommodate the electronics boards of the solenoids, which have a 42-mm height. In addition, since subsequent solenoids are rotated by 180 degrees in the decelerator, any asymmetry in the magnetic field because of the relatively coarse winding geometry is compensated.

Vacuum inside the decelerator housing is maintained by a vacuum pump installed under the detection chamber, which has an open connection to the decelerator housing. Only a minor pressure increase in the chamber is observed if the solenoids are operational, reflecting the relatively low operational temperature of the solenoids. Although for a longer decelerators additional pumping capacity inside the decelerator is advantageous, we find that for the relatively short decelerator used here the beam density is hardly deteriorated by collisions with background gas provided the repetition rate of the experiment is below 5 Hz. Under these conditions, the pressure in the decelerator maintains below $5 \cdot 10^{-7}$ mbar.

4.2.2 Metastable helium beam

A beam of helium in the metastable $(1s)(2s) \ ^3S$ ($m_S = 1$) state (from this point He^*) was used to test the performance of the Zeeman decelerator. This species was chosen for two main reasons. First, He^* has a small mass-to-magnetic-moment ratio ($2.0 \text{ amu}/\mu_B$) with a large Zeeman shift, which allows for effective manipulation of the atom with magnetic fields. This allows us to significantly vary the mean velocity of the beam despite the relatively low number of solenoids. Sec-

ond, He* can be measured directly with a microchannel plate (MCP) detector, without the need for an ionizing laser, such that full time-of-flight (TOF) profiles can be recorded in a single shot. This allows for a real-time view of TOF profiles when settings of the decelerator are changed, and greatly facilitates optimization procedures.

The beam of He* is generated by expanding a pulse of neat He atoms into vacuum using a modified Even-Lavie valve (ELV) [100] that is cooled to about 16 K using a commercially available cold-head (Oerlikon Leybold). At this temperature the mean thermal velocity of helium is about 460 m/s. The ELV nozzle is replaced by a discharge source consisting of alternating isolated and conducting plates, equivalent to the one described in section 2.1.3. The discharge occurs between the conducting plates, where the front plate is kept at -600 V and the back plate is grounded. To ignite the discharge, a hot filament running 3 A of current is used. The voltage applied to the front plate is pulsed (20-30 μ s duration) to reduce the total energy dissipation in the discharge. Under optimal conditions, a beam of He* is formed, with a mean velocity just above 500 m/s. Unless stated otherwise, in the experiments presented here, the decelerator is programmed to select a packet of He* with an initial velocity of 520 m/s.

The beam of He* passes through a 3-mm diameter skimmer (Beam Dynamics, model 50.8) into the decelerator housing. The first element (a hexapole) is positioned about 70 mm behind the skimmer orifice. The beam is detected by an MCP detector that is positioned 128 mm downstream from the exit of the decelerator. This MCP is used to directly record the integrated signal from the impinging He* atoms.

4.3 Results and Discussion

4.3.1 Longitudinal velocity control

As explained in section 3.2, the decelerator can be operated in three distinct modes of operation: in deceleration or acceleration mode, the atoms are most efficiently decelerated or accelerated, respectively, whereas in the so-called hybrid mode of operation, the beam can be guided through the decelerator at constant speed (some mild deceleration or acceleration is in principle also possible in this mode). In this section, we present experimental results for all three modes of operation.

We will start with the regular deceleration mode. In Figure 4.3, TOF profiles for He* atoms exiting the decelerator are shown that are obtained when the decelerator is operated in deceleration mode, using different values for the equilibrium phase angle ϕ_0 . In the corresponding pulse sequences, the synchronous atom is decelerated from 520 m/s to 365 m/s, 347 m/s and 333 m/s, corresponding to effective equilibrium phase angles of 30°, 45° and 60°, respectively. The corre-

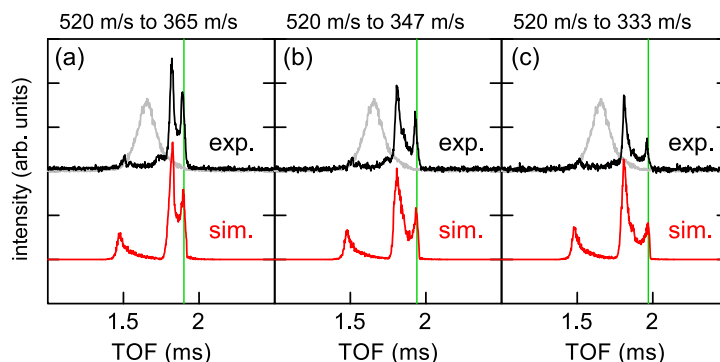


Figure 4.3: TOF profiles of He^* exiting the Zeeman decelerator when the decelerator is operated in deceleration mode using an effective equilibrium phase angle of 30° (a), 45° (b) and 60° (c). Deceleration sequences were used to select an initial velocity of 520 m/s, resulting in the final velocities mentioned above each graph. Black traces are the experimentally obtained profiles, red traces show the profiles that result from numerical trajectory simulations. The gray traces show the TOF profiles that are measured when all solenoids are switched off. Vertical green lines indicate the arrival times of the synchronous atoms that are expected from the simulations.

sponding loss of kinetic energy amounts to 23 cm^{-1} , 25 cm^{-1} and 27 cm^{-1} . The arrival time of the synchronous atom in the graphs is indicated by the vertical green lines. Black traces show the measured profiles; the gray traces that are shown as an overlay are obtained when the decelerator was not operated, i.e., the solenoids are all inactive but the permanent hexapole magnets are still present to focus the beam transversely.

The experimental TOF profiles are compared with profiles that result from three dimensional trajectory simulations. In these simulations, an initial beam distribution is assumed that closely resembles the He^* pulse generated by the modified ELV. The resulting TOF profiles are shown in red, vertically offset from the measured profiles for clarity. The simulated profiles show good agreement with the experiment, both in relative intensity and arrival time of the peaks. However, it must be noted that the relative intensities are very sensitive to the chosen parameters of the initial He^* pulse. By virtue of the supersonic expansion and discharge processes, these distributions are often not precisely known, and may vary from day to day. Nevertheless, the agreement obtained here, in particular regarding the overall shape of the TOF profiles and the predicted arrival times of the decelerated beam, suggests that the trajectory simulations accurately describe the motion of atoms inside the decelerator. No indications are found for unexpected loss of atoms during the deceleration process, or for behavior that is not described

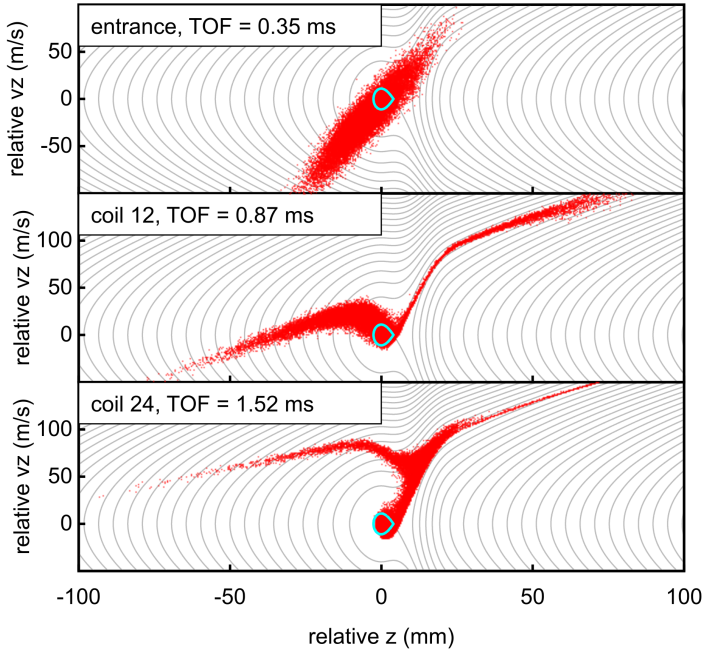


Figure 4.4: Longitudinal phase-space distributions of He^* atoms during a deceleration sequence from 520 m/s to 365 m/s, obtained from simulations. The horizontal (vertical) axis shows the longitudinal position (velocity) relative to the synchronous atom. Each red dot represents a simulated He^* atom. Grey contour lines show the expected trajectories derived from the averaged Zeeman potential energy, and the cyan contour shows the separatrix of the stable region in phase-space. The distributions are sampled at the time the synchronous atom enters the decelerator (top), when it arrived at solenoid 12 (middle) and solenoid 24 (bottom).

by the simulations.

The profiles presented in Figure 4.3 show more features than the decelerated packets alone. In particular, there is an additional decelerated peak in each of the graphs that is more intense but slightly faster than the decelerated packet. We use the three dimensional trajectory simulations to study the origin of this feature. In Figure 4.4, the longitudinal phase-space distributions are shown that result from these simulations at the entrance (upper panel), middle (central panel), and exit (lower panel) of the decelerator. The simulation pertains to the situation that

results in the TOF profiles presented in Figure 4.3a, i.e., the decelerator is operated in deceleration mode with $\phi_0 = 30^\circ$.

In these phase-space distributions, the grey contour lines depict the predicted trajectories considering the time-averaged Zeeman potential energy. The separatrix of the stable phase-space is highlighted with a cyan overlay. From this evolution of the longitudinal phase-space distribution, we can understand the origin of various pronounced features in the TOF profiles. The first peak in each TOF profile is a collection of the fastest particles in the initial beam distribution. These particles are hardly affected by the solenoids, and propagate to the detector almost in free flight. However, the part of the beam that is initially slower than the synchronous molecule is strongly affected by the solenoids. This part eventually gains in velocity relative to the decelerated bunch, resulting in an ensemble of particles with a relatively high density. This part arrives at the detector just before the decelerated He* atoms, resulting in the second intense peak in the TOF profiles of Figure 4.3. It is noted that this peak appears intense because our decelerator is rather short, leaving insufficient time for the decelerated bunch to fully separate from the initial beam distribution. For longer decelerators, the part of the beam that is not enclosed by the separatrix will gradually spread out, and its signature in the TOF profiles will weaken.

The phase-space distributions that are found at the end of the decelerator may also be used to determine the velocity width of the decelerated packet of atoms. In the example of Figure 4.4, these widths are about 25 m/s.

For completeness, we also measure a TOF profile when the decelerator is operated in acceleration mode. Figure 4.5a shows the TOF profile for the acceleration of He* atoms from an initial velocity of 560 m/s to a final velocity of 676 m/s. The simulated profile (red trace) shows good agreement with the experimental profile (black trace). Again, the vertical green line indicates the expected arrival time of the accelerated bunch. The sequence selects the fastest atoms in the beam, which is why no additional peaks are visible.

Finally, we study the performance of the decelerator in hybrid mode. This mode of operation allows for guiding of the beam through the decelerator at constant speed. In Figure 4.5b a TOF profile is shown when the decelerator is operated in hybrid mode and $\phi_0 = 0^\circ$, selecting an initial velocity of 520 m/s. The simulated TOF profile (red trace) again shows good agreement with the experimental TOF profile (black trace), although the intensity ratios between the guided part and the wings of the distributions are slightly different in the simulations than in the experiment. This is attributed to the idealized initial atom distribution that are assumed in the simulations.

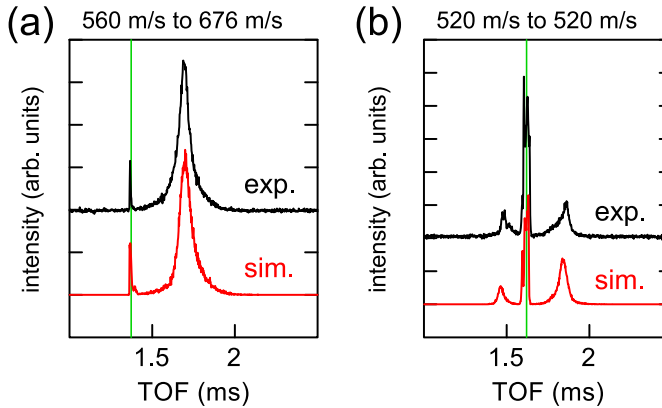


Figure 4.5: (a) TOF profile of He^* accelerated by a multistage Zeeman decelerator from 560 m/s to 676 m/s. The black and red trace correspond to the experimental and simulated TOF profiles, respectively. (b) Experimental (black) and simulated (red) TOF profile when the decelerator operates in hybrid mode, guiding a bunch of atoms with mean velocity of 520 m/s. The vertical green lines depict the arrival time of the synchronous atom in the simulation.

4.3.2 Presence of metastable helium molecules

While our experiment is designed to decelerate He^* atoms in the 3S state, other types of particles may be created in the discharged beam as well. Specifically, formation of metastable He_2 molecules in the $a^3\Sigma$ state (from here on He_2^*) is expected, as is also observed in the experiments by Motsch *et al.* and Jansen *et al.* that use a similar discharge source [101, 102]. However, He_2^* is indistinguishable from He^* in our detection system. In order to probe both species separately, mass-selective detection using a non-resonant laser ionization detection scheme is used. Ultraviolet (UV) laser radiation with a wavelength of 243 nm is produced by doubling the light from an Nd:YAG-pumped pulsed dye laser running with Coumarin 480 dye, and focused into the molecular beam close to the exit of the decelerator. The resulting ions are extracted with an electric field of about 1 kV/cm and accelerated towards an MCP detector, where the arrival time of the ions reflect their mass-over-charge ratio.

We used this detection scheme to investigate the chemical composition of the beam that exits the Zeeman decelerator. In Figure 4.6, ion TOF spectra (i.e., the arrival times of the ions at the MCP detector with respect to the laser pulse) are shown. The black trace shows the ion TOF spectrum if the beam of He^* atoms is passed through the decelerator without operating the solenoids. The UV laser

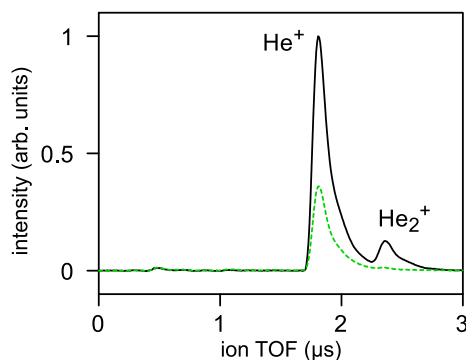


Figure 4.6: Ion-TOF spectra of ions created when UV radiation interacts with the beam that exits the Zeeman decelerator. The black trace is taken for a beam that passes through the decelerator with inactive coils, while the green trace results from a Zeeman decelerated part of the beam.

is fired at the mean arrival time of the beam in the laser ionization region. Two peaks are clearly visible corresponding to the expected arrival time of He^+ and He_2^+ , confirming that indeed He_2 molecules are created in the discharge. He atoms and molecules are detected in an 8:1 ratio in the neutral beam.

The green trace in Figure 4.6 shows the ion TOF spectra that is recorded when the solenoids are operated for a typical deceleration sequence similar to the ones used to generate Figure 4.3. This trace was taken when the UV laser selectively detects the decelerated part of the He^* beam. Here, only He^+ is present in the ion TOF spectrum. Although He_2^* has the same magnetic moment as He^* and will thus experience the same force, the double mass of the molecule results in only half the acceleration. He_2^* is therefore not decelerated at the same rate as He^* , and will not exit the decelerator at the same time as the decelerated He^* atoms. In conclusion, the Zeeman decelerator is quite effective in separating He^* from the He_2^* ; the decelerated bunch only contains those species and/or particles in the quantum level for which the deceleration sequence was calculated.

Referring back to Figures 4.3 and 4.5 that were recorded without laser-based mass spectroscopic detection, one may wonder how the presence of He_2^* molecules in the beam affect the recorded TOF profiles. Figure 4.7 revisits the measurement from Figure 4.3a, but taking also He_2 molecules into account with the appropriate ratio to generate the simulated TOF profile. The resulting TOF profile for He_2^* molecules is shown by the green trace, and is seen to fill the part of the TOF that was under represented by the original simulations (indicated by the vertical green arrow for the experimental trace).

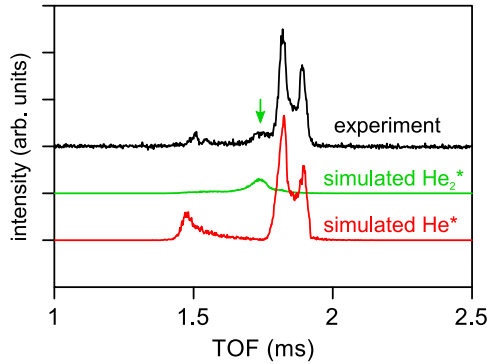


Figure 4.7: TOF profile from Figure 4.3a revisited. The experimental (black) profile is compared to simulated profiles for He^* (red) and He_2^* (green). The simulated signal of He_2^* is scaled to 1/8 of the He^* signal. Each profile is vertically offset for reasons of clarity.

4.4 Conclusions and Outlook

In a proof-of-principle experiment, we demonstrated the successful implementation of a new concept presented in the previous chapter, using a decelerator that consist of 24 solenoids and 25 hexapoles. The performance of the decelerator was experimentally tested using beams of metastable helium atoms. The deceleration, acceleration, and guiding of a beam at constant speed has been demonstrated. The experimental TOF profiles of the atoms exiting the decelerator show excellent agreement with the profiles that result from numerical trajectory simulations. Although the decelerator presented here is relatively short, up to 60% of the kinetic energy of He^* atoms that travel with an initial velocity of about 520 m/s could be removed.

In the Zeeman decelerator presented here, we utilize a rather unconventional solenoid design that uses a thick copper capillary through which cooling liquid is circulated. The solenoid design allows for the switching of high currents up to 4.5 kA, using readily available and cheap low-voltage electronics components. The design is mechanically simple, and can be built at relatively low cost. However, because of the limited pumping capacity of the decelerator vacuum chamber, signal levels suffer at repetition rates above 5 Hz. This limitation is expected to be more pronounced for a longer version of the decelerator. The next chapter describes the construction of an improved 100-stage Zeeman decelerator that solves this problem.

5

Design and construction of a multistage Zeeman decelerator for molecular-beam scattering experiments

With the information gathered from the prototype Zeeman decelerator described in the previous chapter, an improved design was made. In this chapter a detailed description of that new design is given, focusing primarily on the mechanical and electronic aspects. This design carries over the positive characteristics of the prototype design—such as independent longitudinal and transverse focusing—but improves on the cooling and vacuum-pumping capacities. Measurements of metastable rare-gas beams are used to characterize the transverse focusing properties of the decelerator.

Based on

Design and construction of a multistage Zeeman decelerator for crossed molecular beams scattering experiments, T. Cremers, N. Janssen, E. Sweers and S. Y. T. van de Meerakker (submitted, 2018)

5.1 Introduction

This chapter described in detail a multistage Zeeman decelerator that consists of an alternating array of 100 solenoids and 100 hexapoles, such that the transverse and longitudinal motions of particles traveling through the decelerator are decoupled and can be controlled separately. The solenoids are made of copper capillary and are internally cooled using a flow of liquid, affording repetition rates of the experiment exceeding 10 Hz. Electrical currents up to 4.5 kA are pulsed through the solenoids using cost-effective FET-based components, whereas the hexapoles consist of an array of permanent magnets. The decelerator features a modular design, and can easily be extended or shortened to arbitrary length by adding or removing modules. We characterize the focusing properties of the decelerator using beams of metastable He, Ne, Ar or Kr atoms, that are guided through the decelerator and imaged on a screen upon exiting the decelerator.

This chapter is organized as follows: Section 5.2.1 describes the mechanical design of the apparatus in detail, while Section 5.2.2 provides a detailed account on the electronics that power the solenoids. Section 5.2.3 provides a comparison between the solenoid and hexapole contribution to the transverse forces in the decelerator. In Section 5.2.4 the experimental setup is explained. The results of these experiments are presented in Section 5.3. Finally, in Section 5.4 the chapter is summarized and the prospects for our Zeeman decelerator in scattering experiments is discussed.

5.2 Experimental

5.2.1 Mechanical implementation

The multistage Zeeman decelerator presented here features a modular design that allows for an easy extension to arbitrary length. Each module houses 20 solenoids and 19 hexapoles. In 5.1 a depiction of one such module is shown. For easy maintenance and replacement of parts, the solenoids and hexapoles are mounted individually using an aluminium mounting flange, as can be seen in Figure 5.1a and b. The decelerator consists of five modules, yielding a total of 100 deceleration stages. In Figure 5.2 a schematic drawing of the complete decelerator is shown, together with longitudinal cross sections detailing the connections between the source chamber, the decelerator modules and the detection chamber, as well as transverse cross sections that illustrate the positioning of the hexapoles and solenoids. A number of additional hexapoles are installed in the region between the end of the decelerator and the detection region, in order to maintain the transverse particle distribution of the decelerated beam into the detection chamber, as will be further described in section 5.2.4.

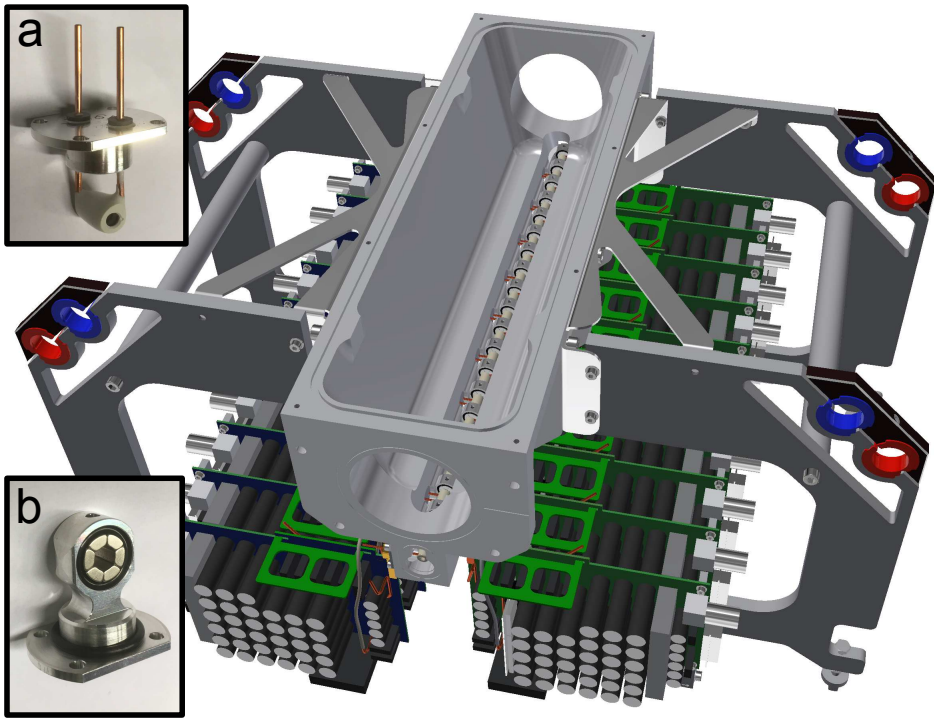


Figure 5.1: Projection of the 3-D model of one multistage Zeeman decelerator module, including the supporting frame and the printed-circuit boards. The cooling tubes and the lid are not included for clarity. The module contains 20 solenoids that are inserted from the sides and 19 hexapoles that are connected from below. The photographs (a) and (b) show respectively a solenoid and a hexapole inside an aluminium flange.

A single module is made from a 150 mm x 150 mm x 440 mm block of aluminium. First, it is modified into roughly the shape of the chamber by a computer controlled milling machine. The final alignment of the decelerator is purely mechanical, therefore the precision of the solenoid and hexapole ports, as well as the connection between adjacent modules is critical. This high level of precision can be achieved by milling all critical sections in a single session. For this, the aluminium block is fixed in a 5-axis computer controlled milling machine, such that the position of each face and threaded hole is well-defined to the accuracy of the 5-axis machine.

Adjacent modules use a stainless steel ring as a dowel, fixing two modules together and aligning them (see Figure 5.2B). This ring holds a hexapole, in order to present an uninterrupted sequence of solenoids and hexapoles throughout the

decelerator. Similar dowels are used at the entrance and exit of the decelerator, where two custom CF200 flanges interface the decelerator to a commercial source and detection vacuum chamber, respectively. For ease of installation, the aluminium modules are connected to a set of braces that are designed to rest on two girders that run parallel with the decelerator. These braces also hold the cooling liquid manifolds running alongside the decelerator, as seen in Figure 5.1.

The solenoids and hexapoles have a center-to-center distance of 11 mm, limited by the combined length of a single solenoid and hexapole, with approximately a 1-mm spacing between them. The hexapoles are inserted into the module from the bottom, whereas the solenoids are inserted from either sides of the module in an alternating manner to facilitate sufficient space for the installation of a printed-circuit board (PCB) for each solenoid (see also the transverse cross sections of a module shown in Figure 5.2). The top of a module is closed with a lid that has two CF63 and one CF100 flange port, which can be used to install turbo-molecular pumps, pressure gauges, or auxiliary equipment. In our setup, only three of the five modules are equipped with a 250 l/s pump, which yields sufficient pumping capacity to run the experiment at a 10-Hz repetition rate.

The hexapoles are made from six arc-shaped permanent magnets that form a ring with alternating radial magnetization. The commercially available magnets (China Magnets Source Material LTD), consist of grade N30M sintered neodymium. Magnets of this grade typical have a surface magnetic field of about 1.1 T. The magnet ring has an outer diameter of 10 mm, an inner diameter of 5 mm and has a length of 8 mm. This assembly was chosen over the hexapoles used in the prototype design, in order to produce beams of atoms and molecules with reduced transverse spread. The magnet assemblies are fixed in place with two rubber rings in an aluminium mounting flange (see Figure 5.1*b*). A disadvantage of permanent magnets is that the field strength cannot be controlled. Yet, the mechanical implementation as used here allows for an easy and reproducible replacement of the magnets with weaker or stronger magnets. This may need to be considered for species that have a much different mass-over-magnetic-moment ratio than the species used here, or if a smaller transverse velocity spread is required.

The solenoids consist of copper capillary of 1.5-mm outer diameter and 0.6-mm inner diameter, with four and a half windings around a bore of 3 mm in diameter. A winding process was developed that guarantees that all 100 solenoids have the same dimensions, with little to no deviation. The capillary is wound on a rod with evenly spaced grooves that ensure equal spacing between the windings. The straight entrance and exit sections of the solenoid capillary act as feed-through in the aluminium flange, and define the correct positioning of the solenoid with respect to the beam axis. Sufficient accuracy is obtained with a precise mold, in which a rod is fixed through the solenoid at the correct distance from the aluminium flange. A polyvinyl chloride (PVC) bus is used to isolate the capillary

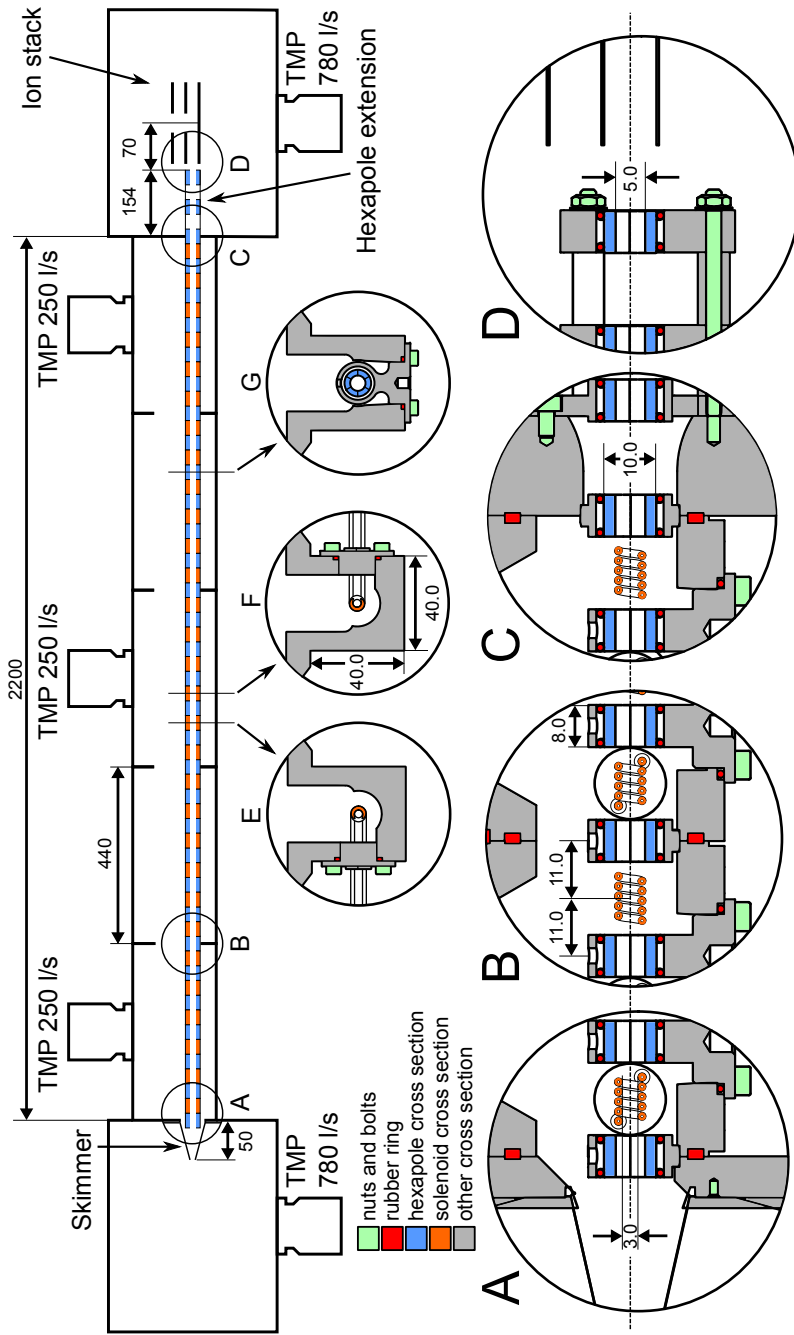


Figure 5.2: Schematic representation of the multistage Zeeman decelerator. Distances are given in mm. The top image shows the Zeeman decelerator together with the source and detection chambers. In this image, four areas of interest are depicted in detailed longitudinal cross sections. These areas are: (A) Connection between source chamber and decelerator module, (B) Connection between two modules, (C) Connection between module and detection chamber, (D) End of the hexapole extension and part of the ion stack. Three transverse cross sections below the main diagram show solenoids mounted from the left (E) and right (F), and a hexapole mounted from below (G).

from the aluminium flange, and is fixed with Torr-seal to obtain a seal suitable for high-vacuum. This resin is heated and applied from both sides and stirred until no air bubbles remain. The accuracy of the solenoid positions and rotations relative to the aluminium mounts is tested by installing them in a decelerator module, and inserting a 2.8-mm diameter PVC rod through the centers of the 20 solenoids. When extra friction is detected during this test, the offending solenoid is identified and replaced. When the rod is transmitted smoothly, the solenoids are accepted.

The hollow capillary allows for a flow of cooling liquid that is thus in direct contact with the solenoids inside the vacuum chamber, an idea that was carried over from the prototype design. The cooling liquid is pumped from a single source (ThermoFisher system I heat exchanger), and a series of manifolds is used to distribute the flow equally, with silicon tubes running to and from the solenoids. These tubes are connected directly to the solenoid feedthroughs, using brass rings that provide a tight seal. Initially automobile coolant (PROFCLEAN, all-season) was used, but it proved unsuitable for the narrow solenoid capillary. The anti-freeze made it too viscous and it occasionally caused obstructions. We switched to racing coolant (BARDAHL ref. 13113), which forgoes the anti-freeze agent but still has anti-corrosive properties.

For optimal cooling, a rapid flow is needed, which depends on the pressure difference between the liquid at the entrance and exit of the solenoids. The maximum pressure difference before the silicon tubes would detach from the solenoids was found to be 1.5 bar. In the experiments, a pressure difference of 0.8 bar is used, which has proven sufficient to run the solenoids at repetition rates of 10 Hz.

In early testing stages, when applying current pulses to the solenoids, they would audibly flex due to the self-inductive force on the capillary. In some cases, after a few months of operation, the capillary was found to tear open and spill cooling liquid. To prevent breaks, solenoids were coated with Torr-seal to combat the flexing motion. After being applied to the solenoid, the resin is heated to reduce viscosity and release any trapped air. The solenoid is rotated until the resin hardens, to prevent the resin from accumulating on one side. A Teflon rod is inserted into the center of the solenoid when applying the resin, such that the bore of the solenoid remains fully unobstructed. Since Torr-seal does not adhere to Teflon, the rod is easily removed after the resin has set. No further ruptures of solenoids were observed, for almost non-stop operation during a full year.

When the five modules were fully assembled with solenoids and hexapoles, a final check was performed to confirm the precise alignment between the modules. While very small deviations between the modules are expected to be compensated by the hexapoles, larger deviations could significantly reduce the number of transmitted particles. However, with a theodolite we observed a straight sight-line through the entire decelerator, which is a good indication that the modules are well aligned.

5.2.2 Electronics

Each solenoid is connected to an individual PCB that is powered by a separate 24-volt power supply. These low voltages are sufficient because of the low resistance in the solenoids ($\approx 1 \text{ m}\Omega$), and allow for the use of relatively cheap FET-based electronic components compared to the high-voltage IGBT switches that are used in Zeeman decelerators of other design. The PCBs can provide two successive current pulses of up to 4.5 kA per deceleration sequence. With these currents, magnetic fields above 2 T are generated in the solenoid center. The currents are pulsed for 10-100 μs , depending on the mean velocity of the molecular packet. The duration of these pulses, in combination with the maximum current and the experimental repetition rate, defines the amount of heat dissipated in the solenoid and in the PCB. In order to maintain repetition rates of at least 10 Hz, the PCB is liquid cooled using the same manifold that provides the cooling liquid to the solenoids. A 40-mm fan is mounted on each PCB for additional cooling.

Figure 5.3a shows a simplified schematic of the electronic circuit of the PCB, including the solenoid. The schematic circuit also shows the three possible pathways in which the current can flow. The first pathway is active when gate S1 is closed, and is used to drive the capacitor charge through the solenoid, providing up to 4.5 kA of current for a short time. The second pathway is engaged when S2 is closed, which adds a 100-m Ω resistance in series with the solenoid. With this resistor in series, the current through the solenoid is severely reduced, down to about 150 A. This small current is sufficient to provide a bias magnetic field inside the solenoids that prevent Majorana transitions in the molecular packet [83]. This pathway is used when the particles pass through the solenoid after switch S1 has opened. The third pathway is used to eliminate flyback when gates S1 and S2 are open, by sending any excess charge back to the capacitors.

Depending on the mode of operation, switch S1 is opened in a single (deceleration and acceleration mode) or double pulse (hybrid mode). Figure 5.3c and d show the current profiles through the solenoid when it receives a single and double pulse, respectively. These profiles were obtained from the induced voltage over a miniature solenoid that was placed inside the center of a decelerator solenoid. This provided us with the shape of the current pulses in our solenoids. As can be seen in the measured profiles, there is a significant rise and fall time in the current profiles. This is due to the self-inductance in the solenoid (50 nH) and surrounding electronics. In previous iterations of the electronics, the rise time was reduced by using a fourth pathway that increased the potential difference through the solenoid to 60 V. However, the reduction in rise time was too small to justify the increased stress on the switching transistors. The rise and fall profiles are necessarily taken into account when calculating the switching times of the solenoids in the simulation. Exponential rise and fall curves are used with exponential factors around 20 μs . The second pathway is automatically engaged 30 μs after the

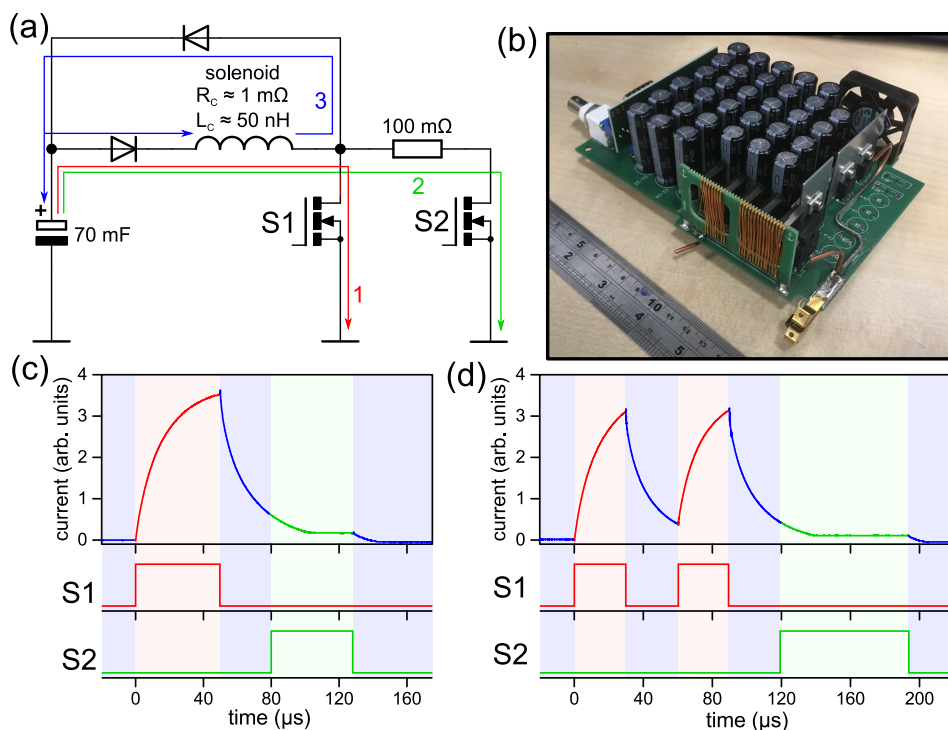


Figure 5.3: Schematic representation of the driving electronics and the current pulse through a solenoid. (a) A schematic drawing of the electronic circuit enabling the solenoid current. The capacitor of 70 mF in the bottom-left represents a parallel array of 32 smaller capacitors of 2.2 mF. The PCB in the photograph of panel (b) features these capacitors as the main component. Current profile of a single (c) or double (d) pulse through the solenoid derived from the voltage induced in a smaller pickup solenoid. The trigger pulses for gates S1 and S2 to generate these pulses are shown underneath the current profiles. The color in the profiles correspond to the currently active electronic pathway in panel (a). The colored pathways correspond to: 1. maximum current through solenoid, 2. reduced current through solenoid, and 3. dissipation of any leftover current in the solenoid. (color online)

single or double S1 pulse is terminated, and remains active during 50 - 80 μs . The 30- μs delay allows the current to decay more quickly through the second pathway while preventing excessive heat to be generated in the resistor. The 50 - 80 μs duration was chosen as sufficient time for all molecules in a packet to benefit from the quantization field.

One of the challenges in designing the PCBs is the relatively high current that

flows through the components, which causes a large amount of heat dissipation. In order to counteract this, where possible the tracks between electrical components are kept at low resistance by using as much of the PCB surface as possible. Additionally, cooling liquid is flowed through copper capillary that is directly soldered onto the PCB area that experiences the most heat dissipation. The connection between PCB and solenoid is necessarily kept as short as physically possible, by attaching it directly onto the solenoid legs with a set of brass clamps. These brass clamps and the copper cooling tubes on the PCB are seen in the bottom-right of Figure 5.3*b*. The length of the solenoid leg between the clamp and the beginning of the solenoid is only about 23 mm, yet it constitutes about 40% of the total current carrying wire. For the 100 m Ω resistance in the second current pathway a conventional resistor proved unsuitable, as its thermal conductivity was not sufficient to disperse the heat pulse generated in a single switching sequence. Instead a bifilar coil of copper wire is used as a resistor. The wire is wrapped around a rectangular grid that maximizes the surface area. This component is custom made, and can be seen next to the brass clamps in Figure 5.3*b*. The temperature of each solenoid is continuously monitored via a thermocouple on the connecting clamps of the circuit board. When the temperature of the solenoid exceeds a user-set threshold, operation of the decelerator is interrupted.

The switching timings for the solenoids are calculated using a molecular trajectory program, by simulating a synchronous particle. The list of timings is sent to a small computer (Raspberry Pi), which passes them onto a timing PCB for each solenoid. Each individual timing is addressed with a unique number that is recognized by a dual in-line package (DIP)-switch system on the PCBs. Once loaded, these timing PCBs are synchronized to a single 20 MHz clock, and start counting when the system receives an external trigger. At the loaded pulse timings, they send a trigger to the PCB connected to the solenoid, which then generates a pulse for the appropriate duration.

5.2.3 Transverse focusing

The magnetic field inside a solenoid running 4.5 kA of current was calculated by applying the Biot-Savart law to a solenoid geometry that matched our solenoid design. The result is shown in Figure 5.4*a*. The fields are calculated along lines parallel to the beamline at three different transverse positions. The magnetic field distributions close to the inside of the solenoid are shown to fluctuate based on the proximity to the nearest capillary. Consequently, the entrance and exit connections of a solenoid cause an asymmetry in the induced magnetic fringe fields near the ends of a solenoid. Adjacent solenoids are therefore rotated such that all entrance connections are positioned on alternating sides of the beam axis, to average out the asymmetry. For LFS particles, the average transverse gradient of

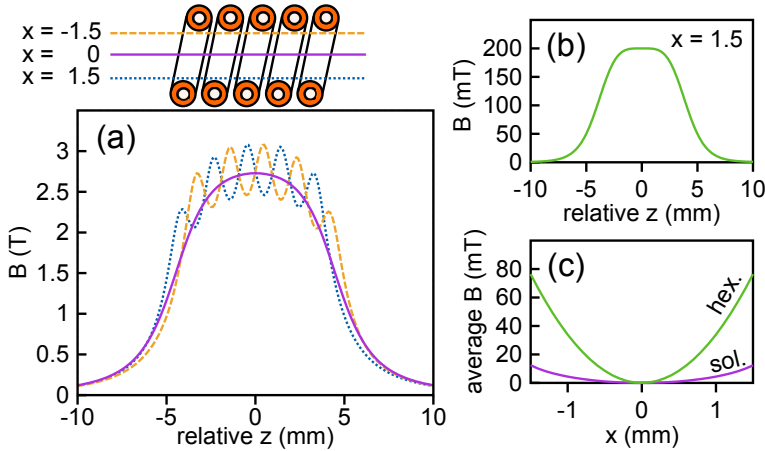


Figure 5.4: (a) The magnetic field strength, B , inside one of our solenoids running 4.5 kA of current, as a function of the longitudinal position, z , relative to the solenoid center. A cross section of a solenoid is shown above the graph, with the lines along which the magnetic fields were calculated. (b) The magnetic field strength of a hexapole used in our experiments, at a radial offset of 1.5 mm, as a function of the relative longitudinal position. (c) The average magnetic field contribution of the solenoids (purple) and hexapoles (green) along the transverse coordinate, x . The average was taken over two periods of the active decelerator (see equation 5.1 and the accompanying text).

the solenoids provides a focusing force directly inside the solenoids, but results in a small defocusing force in the fringe fields.

The magnetic field inside a hexapole was calculated using Radia 4.29 [103], and is shown in Figure 5.4b, for a transverse offset of 1.5 mm. On-axis the hexapole magnetic field is by definition zero, resulting in a magnetic field gradient that is purely focusing for all LFS particles. From a quick comparison of the transverse gradients of the solenoid and hexapole fields, it would seem that the solenoids provide the stronger transverse focusing. However, due to the rising and falling of the currents inside the solenoids, this is not the case. We show this with a particle simulation that uses the routines from a previous work [83], but with updated current profiles and field distributions. We simulate the synchronous particle to obtain the time-dependent magnetic fields, and calculate the average contribution of the solenoids and hexapoles to the field as a function of the transverse coordinate, x . The field was averaged over two time periods of the decelerator to average out the effect of the solenoid fringe fields:

$$B_{avg}(x) = \frac{1}{2T} \int_0^{2T} B(z(t), x, t) dt \quad (5.1)$$

where one period, T , is the time in which the synchronous particle passes one solenoid and one hexapole, and z is the longitudinal position of the synchronous particle. B is the magnetic field strength inside the decelerator, which depends on the position and the time in the decelerator. The vertical offset, y , is set to zero. We chose a decelerator sequence that is representative for the experiments described in section 5.3, specifically a guiding sequence at 550 m/s. The result of this simulation can be seen in Figure 5.4c, for the contributions of the solenoids and hexapoles separately. In the solenoid contribution, the minimum magnetic field was set to zero, to show only the transverse gradient. The permanent magnetic hexapoles contribute significantly more to the transverse focusing of the particle beam, about five times more compared to the solenoids. By contrast, the solenoids affect the longitudinal velocity components, much more than the hexapoles. These two elements together allow for nearly independent control over the longitudinal and transverse properties of decelerated particles. The transverse and longitudinal focusing properties are also independent of the length of the decelerator, due to the phase-stable nature of the multistage Zeeman decelerator, as evident from section 3.2.2.

5.2.4 Experimental setup

In order to characterize the Zeeman decelerator, and experimentally validate the suitability of the solenoid-hexapole concept for Zeeman deceleration, beams of atoms or molecules are passed through the Zeeman decelerator and their arrival in the detection area is monitored. Control over the longitudinal velocity of oxygen atoms and molecules will be demonstrated in chapter 6, where we presented time-of-flight (TOF) profiles of the atoms and molecules exiting the decelerator. In this chapter, we primarily focus on the transverse properties of the decelerator. For this, we generate beams of metastable rare gas atoms (He, Ne, Ar and Kr), and guide them through the decelerator in hybrid mode. We measure the radial distribution of the atoms upon exiting the Zeeman decelerator, which probes the transverse velocity spread of the Zeeman decelerated packet. A schematic representation of the experimental setup can be seen in Figure 5.5.

Rare gas atoms are brought into a metastable state via an electric discharge, by promoting one electron from the highest occupied atomic orbital to the lowest unoccupied orbital. Rare gas atoms in these metastable states have enough internal energy to release an Auger electron when they impinge on a microchannel plate detector (MCP) [67]. The subsequent electron avalanche can be measured directly. In addition, a phosphor screen is attached to the MCP that generates a flash of light at the impact position. A CMOS camera is used to record the light from the phosphor screen to retrieve a spatial map of the metastable atoms exiting the decelerator.

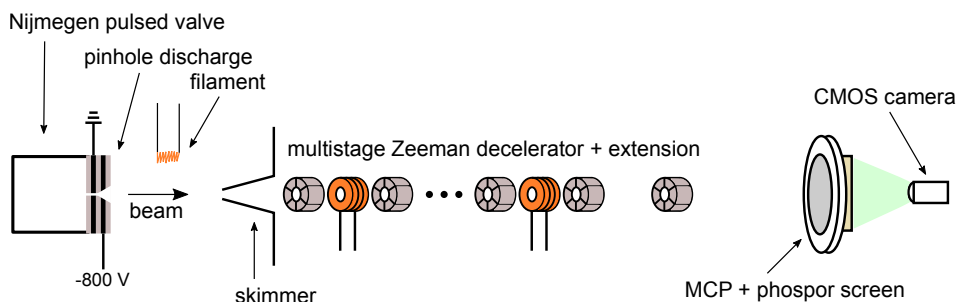


Figure 5.5: Schematic diagram of the experimental setup. The extension consists of eight hexapoles and is positioned between the exit of the decelerator and the detection region. The distance from the valve to the skimmer is approximately 100 mm, and the distance from the final hexapole to the MCP detector is 250 mm.

A Nijmegen pulsed valve is used to create supersonic beams of rare gas atoms [74]. The gases are expanded at room temperature with a repetition rate of 10 Hz. The atoms are brought into the metastable states by a discharge in the pinhole nozzle described in section 2.1.3. The front plate of the discharge nozzle is set to -800 V for 30-50 μs pulses, depending on the gas. A hot filament, consisting of a 0.3-mm diameter tungsten wire in a tight spiral through which 3 A of current is passed, is mounted near the valve orifice and used to stabilize the discharge process. The metastable atoms pass through a skimmer and into the multistage Zeeman decelerator. Between the exit of the decelerator and the detection region, an extension consisting of eight hexapoles is placed. The MCP with phosphor screen is placed 250 mm from the final hexapole. A voltage difference of 1600 V is applied over two MCP plates, and the phosphor screen is set to 4500 V. The MCP voltage is pulsed using a Behlke high-voltage switch, limiting the measurement time to only 20 μs , which is sufficient to distinguish the Zeeman decelerated atoms from the remainder of the gas pulse.

5.3 Results

A combination of TOF profiles and radial distributions were measured for metastable He, Ne, Ar and Kr atoms that exit the Zeeman decelerator. The electronic states together with the ratios of mass-to-magnetic dipole moment are listed in table 5.1. While neon and krypton are composed of a mix of different isotopes, we considered only the most abundant isotopes (^{20}Ne and ^{84}Kr) in the calculation of the velocity distributions and solenoid timings for the guiding sequences. To determine the mean velocity of the metastable atom beam, TOF profiles were first measured

atom	state	m/μ (amu/ μ_B)	exp. \bar{v}_z (m/s)	selected \bar{v}_z (m/s)	max. v_x (m/s) for 90% of packet
^4He	$1s2s\ ^3S_1$	2.00	1950	1750	12.2
^{20}Ne	$2p^53s\ ^3P_0$	6.73	1210	1100	8.5
^{40}Ar	$3p^54s\ ^3P_0$	13.32	790	790	6.0
^{84}Kr	$4p^55s\ ^3P_0$	27.93	550	550	3.5

Table 5.1: Various properties of metastable rare-gas atom beams that are relevant for Zeeman deceleration. v_z denotes the longitudinal velocity, and v_x the transverse velocity.

for all species with the solenoids off, i.e., the atoms are then only transversally focused by the hexapole array. The resulting profiles are shown in Figure 5.6 as the dashed traces, which are all normalized with respect to each other. From these profiles, and the known discharge ignition time and travel path from the source to the detector, the mean beam speeds as given in table 5.1 were deduced. These speeds are significantly higher than what may be expected for a room temperature expansion, which is attributed to heating effects due to the discharge process.

The Zeeman decelerator is subsequently used in hybrid mode and programmed to select a velocity that is close to the mean velocity of the beam. This was possible for all metastable atoms, except for the helium beam which traveled too fast to be significantly affected by the pulsed magnetic fields. The measured TOF profiles after guiding for Ne, Ar and Kr are shown in Figure 5.6. The central narrow peak in the TOF profiles contains the packet of guided atoms, and is well separated from the remainder of the atom beam even for beams of metastable Ne atoms that travel with a mean speed exceeding 1000 m/s. The guided packets of Ne, Ar and Kr had a similar longitudinal velocity spread, approximately 20 m/s, and spatial spreads of around 10 mm, 13 mm and 16 mm, respectively. The ability of the decelerator to manipulate the longitudinal motion of paramagnetic particles has been explored in a previous work [104]. Here, we focus on the transverse distributions of atoms at the end of the decelerator.

The radial distributions were measured for the selected packets of Ne, Ar and Kr, by gating the MCP such that only the guided packets are recorded. For helium an arrival time was chosen that corresponded with a forward velocity of about 1750 m/s. The images that result from measurements averaged over 50 shots of the experiment are shown in Figure 5.7. A false-color scale is used to display the intensity of the signal, of which the scale is seen in the top-left. Normalized cross sections of the radial distributions are displayed in the graph on the right. Vertical lines indicate the part of the packet that contains 90% (outer vertical lines) and 50% (inner vertical lines) of the atoms within the packet.

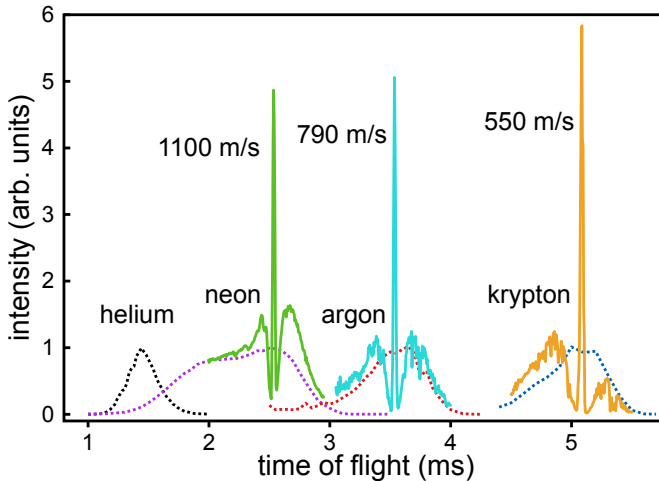


Figure 5.6: Experimental TOF profiles of metastable rare gas atoms, after passing through the multistage Zeeman decelerator. Profiles with dashed lines correspond to beams passed through the decelerator when the solenoids were not activated. For neon, argon and krypton, the decelerator is used in hybrid mode to guide the atoms through the decelerator at constant speed as indicated, resulting in the profiles with solid lines. The relative intensities for profiles corresponding to different rare gas beams are normalized with respect to the dashed curves.

The spatial distribution observed in the images result from the spatial spread of the packet at the exit of the hexapole extension, in combination with the transverse spread that is built up during the free flight towards the detector. The latter is governed by the inherent transverse velocity distribution in the packet, which in turn is governed by the transverse focusing forces of the hexapole array in the Zeeman decelerator. Since the hexapole magnets induce a magnetic field that is quadratic in the radial position, the atoms move as a harmonic oscillator in the transverse directions. In this motion, the maximum transverse velocity in the decelerator is found on the beam axis. By calculating the free-flight time of the atoms to the detector, and relating this to the maximum deviation a particle reaches when it originates from the beam axis, an upper limit to the radial velocity can be deduced from the images. Using this method, the maximum transverse velocities are calculated for the part of the packet containing 90% of the guided atoms. The resulting values are given in table 5.1, and are seen to approximately scale with $\sqrt{m/\mu}$ as expected for a harmonic oscillator.

The largest deviation from this expected result is found in the helium velocity, which should be around 15.6 m/s. This deviation stems from the measured radial

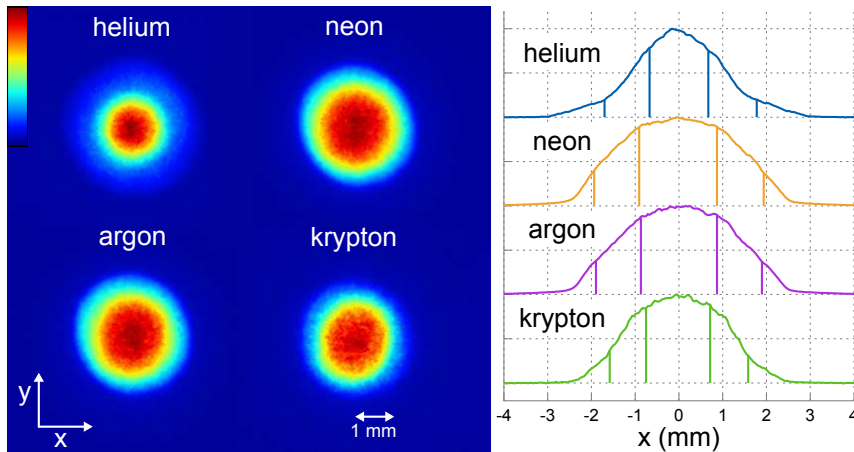


Figure 5.7: Experimental spatial distributions in the transverse plane of packets of metastable He, Ne, Ar and Kr atoms exiting the multistage Zeeman decelerator. The false-color scale depicts the intensity of the recorded signal. The graphs on the right depict the radial cuts, with different vertical offset and normalized intensity. The inner and outer vertical lines in the graphs encapsulate 50% and 90% of the total number of atoms in the packet, respectively.

distribution, which is more narrow than a calculation of the magnetic forces would suggest. More numerical trajectory simulations were performed to look directly at the transverse phase-space distributions of the metastable helium beam inside the decelerator. The results are shown in Figure 5.8. In the simulation we generated an initial helium distribution that is an approximation of the beam distribution in the experiment. While it is not an exact match, it can be used to give an understanding of the phase-space evolution in the decelerator. Due to the aperture of the skimmer, the helium distribution is truncated when flown into the first hexapole, as seen in the Figure 5.8a. With the average magnetic field gradients calculated in section 5.2.3, the transverse separatrix for helium atoms in our decelerator was calculated, and displayed over the phase spaces. Because the separatrix is not uniformly filled, the transverse phase-space distributions show significant changes in time. The particles make around five harmonic oscillations before they reach the final hexapole. During these oscillations, the transverse phase-space distribution alternates between maximum spatial and velocity spread. The transverse phase-space distribution when the helium exits the final hexapole is shown in Figure 5.8d. Because the particles have close to maximum spatial spread, the velocity distribution is more narrow than the separatrix would suggest. This is reflected in the spatial distribution found at the MCP detector position, seen in Figure 5.8e.

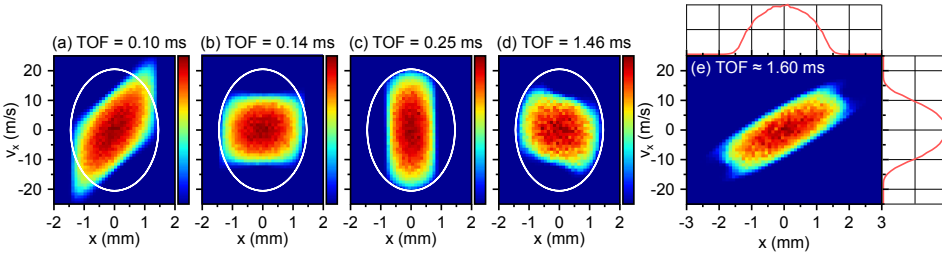


Figure 5.8: Simulated transverse phase-space diagrams of metastable helium at different times-of-flight in our multistage Zeeman decelerator with the solenoids off. The atom density is displayed with a false-color scale. The diagrams (a-d) include the separatrix of stable transverse phase-space as a white ellipse. The diagrams were generated at: (a) the entrance of the decelerator (b) the first time of maximum spatial spread (c) the first time of maximum velocity spread (d) the end of the hexapole extension (e) the position of the MCP detector in the experiment. For this final diagram the spatial and velocity distributions are also shown as individual profiles.

For Ne, Ar and Kr, the radial distributions were also measured when the solenoids in the Zeeman decelerator were not used and switched off (data not shown). These distributions showed no significant differences from the images recorded when the Zeeman decelerator was used in hybrid mode to guide the beams at constant speed. This substantiates the design principle of the decelerator, which was chosen to have transverse focusing independent of the longitudinal motion. We therefore conclude that the hexapoles focus the beam an equal amount regardless of the solenoid magnetic fields, i.e., the transverse properties of the Zeeman decelerated packets are governed by the hexapole array.

5

5.4 Conclusions and Outlook

In this chapter, a detailed account is given of the implementation of a multistage Zeeman decelerator that is specifically designed for crossed-beam scattering experiments. This Zeeman decelerator is conceptually different from other multistage Zeeman decelerators. It consists of an alternating array of solenoids and magnetic hexapoles that decouple the longitudinal and transverse properties of the decelerator. The solenoid design allows for easy in-vacuum positioning while facilitating efficient internal liquid cooling. In addition, the low resistance and self induction of the solenoids allow for the use of cost-effective low-voltage and FET-based electronic components.

The decelerator features a modular design, that allows for the easy addition or removal of individual modules. The modules are mechanically coupled and

aligned with respect to each other with high precision, and without breaking the solenoid-hexapole array. Excellent vacuum properties are maintained by sufficient pumping capacity delivered by turbo pumps that are directly connected to the modules, and the solenoids and printed-circuit boards are internally cooled. In principle, this allows for operation of the Zeeman decelerator at repetition rates exceeding 10 Hz.

The transverse focusing properties of the hexapoles are investigated by recording the radial distributions of different metastable rare-gas beams that are transmitted through the decelerator. When the hexapoles are used, the radial distributions are found to be unaffected by the magnetic fields of the solenoids, confirming that the hexapoles govern the transverse motion of particles inside the decelerator. The observed spatial distributions probe the transverse velocity distributions of the Zeeman decelerated beams, which were found to be in good agreement with the predictions from numerical calculations of the deceleration process.

The decelerator presented here is ideally suited for crossed-beam scattering experiments. It can easily be extended with a module that interfaces the decelerator with an interaction region where the Zeeman-decelerated beam is intercepted by a secondary beam. The design also allows for the addition of custom-made modules that, for instance, provide additional optical access near the exit of the decelerator. One may also envision the addition of a curved module in which adjacent solenoids and hexapoles are positioned under a small angle. This would allow for efficient removal of carrier gas atoms from the beam which is important for collision experiments involving traps or surfaces. A curved extension may also allow for the implementation of merged beam geometries to reach (ultra)low collision energies well below 1 Kelvin [105].

6

Multistage Zeeman deceleration of O and O₂

In the previous chapter, the design of a 3-meter long multistage Zeeman decelerator was described in detail and the transverse phase-space properties of guided paramagnetic beams were analyzed. In this chapter, we take a closer look at the ability of this decelerator to slow down particles. In particular, oxygen atoms and oxygen molecules are used to demonstrate the longitudinal velocity control that is attainable with the decelerator.

Based on

Multistage Zeeman deceleration of atomic and molecular oxygen, T. Cremers, S. Chefdeville, V. Plomp, N. Janssen, E. Sweers and S. Y. T. van de Meerakker, *Phys. Rev. A* **98**, 033406 (2018)

6.1 Introduction

The 100-stage Zeeman decelerator that was described in the previous chapter is used to produce state-selected beams of O (3P_2) atoms, for which we tune to a final mean velocity in the 500 - 125 m/s range. We further characterize the decelerator using beams of O₂ ($X^3\Sigma_g^-$) molecules, which we tune to velocities in the 350-150 m/s range. For both O and O₂, excellent agreement is obtained with the arrival time distributions predicted by numerical trajectory simulations of the beam manipulation process, indicating that our decelerator concept of using an alternating sequence of hexapoles and solenoids is truly phase stable. This allows for the production of intense, state-selected and velocity tunable packets of paramagnetic species, that are ideally suited for controlled elastic, inelastic or reactive scattering experiments.

6.2 Experimental

The setup is shown schematically in Figure 6.1. The molecular beam is created with a modified Even-Lavie valve (ELV) [73]. The default nozzle was replaced by a pinhole discharge that was used in to produce metastable He in chapter 4. The reservoir behind the ELV is filled with a gas mixture of 10% O₂ in Ar at a pressure of approximately 6 bar and the valve body is cooled to 200 K using a commercially available cold head (Oerlikon Leybold). At this temperature, the argon-seeded molecular beam is created with a mean forward velocity of about 510 m/s. With an electrical discharge, the beam of molecular oxygen can be partially dissociated to atomic oxygen. In the 3P_2 ground state, oxygen atoms have a magnetic moment of three Bohr magnetons, and a mass of 16 amu. This magnetic-moment-to-mass ratio is higher than that of ground state oxygen molecules ($X^3\Sigma_g^-, N = 1$), with a maximum magnetic moment of two Bohr magnetons and a mass of 32 amu.

The pinhole discharge is operated with a 50 μ s pulse of -750 V on the front plate, thus creating an electrical discharge through the expanding gas, resulting in the dissociation of O₂ into its atomic components. The discharge was reliably operated by utilizing a 0.3-mm diameter tungsten filament running a 2.5-A current, positioned next to the ELV nozzle. We observe no significant velocity change in the molecular beam from the discharged current. After the supersonic expansion from the ELV and 100 mm of free flight, the beam is collimated by a skimmer (Beam Dynamics, model 50.8) with a 3-mm aperture. After the skimmer, the beam enters a series of modular vacuum chambers that contain sections of the multistage Zeeman decelerator. Upon entering the decelerator chamber, the molecular beam immediately encounters the first magnetic hexapole in a series of alternating hexapoles and solenoids. Photographs of the machine can be seen in

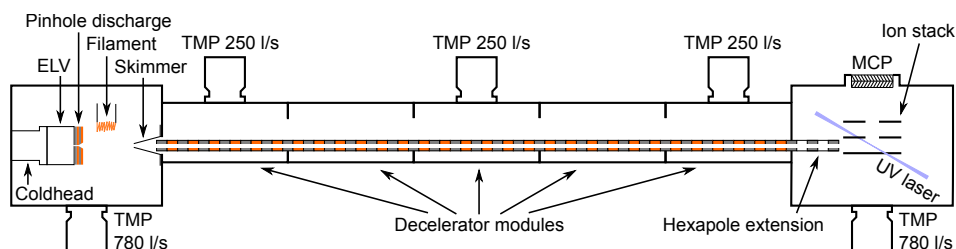


Figure 6.1: Schematic representation of the experimental setup. The main components that are represented: the pulsed valve with optional discharge, the decelerator modules with turbomolecular pump (TMP) and the REMPI detection setup. A second source chamber (not shown here), is connected directly to the detection chamber, without the five decelerator modules in between. The sequence of alternating hexapoles and solenoids is represented by the (grey-orange) dashed lines inside the decelerator modules.

Figure 6.2. For more details, see chapter 5.

A secondary source chamber is connected to the detection chamber, separated by a skimmer. Beams created in this chamber are used to measure the spectra of atomic and molecular oxygen without the influence of the multistage Zeeman decelerator. For these measurements, the ELV was moved from the primary to the secondary source chamber, to generate the same molecular beam.

The Zeeman energy level diagrams of oxygen atoms and molecules in the ground state were derived in chapter 2, and can be seen in Figure 2.2b and c. Both the oxygen atoms and molecules are ionized via a state-selective 2+1 REMPI transition. The oxygen atoms in the $2p^4\ ^3P$ ground state are excited to the $2p^33p^1\ ^3P$ state by absorbing two photons with a wavelength of around 226 nm. A third photon of the same wavelength is used to ionize the atoms. This UV radiation was obtained from the third harmonic of an Nd:YAG pumped, pulsed dye laser containing Pyridin 1. The detection laser had an energy of approximately 0.6 mJ/pulse, a beam diameter of 5 mm and was focused using a spherical lens ($f = 400$ mm). The pulse duration was about 5 ns. After ionization, the positively charged ions are accelerated with electrostatic fields towards a microchannel plate (MCP) detector. Similarly, the oxygen molecules are also ionized with a 2+1 REMPI scheme, using a wavelength of around 225 nm to detect the $X^3\Sigma_g^-$ ground state via a transition to the 3d Rydberg levels [106].



Figure 6.2: Two photographs and a schematic cross-section of the multistage Zeeman decelerator used in this experiment. In the photographs, the lid is removed from the first vacuum chamber. The zoomed-in image shows the connection between two modules, which enables an uninterrupted sequence of solenoids and hexapoles. Solenoids are encased in white epoxy resin (Torr Seal) to resist flexing forces in the solenoids due to self-inductance. The cross-section shows the close proximity of the solenoids and the circuit boards that drive the solenoid currents.

6.3 Results

6.3.1 Oxygen atoms

In Figure 6.3a we show time-of-flight (TOF) profiles of the beam of ground state atomic oxygen (3P_2) using different deceleration sequences applied to the decelerator. The non-decelerated beam (black), where only transverse focusing by the permanent hexapoles affects the particle beam, is used as a reference to normalize all measurements. By operating the multistage Zeeman decelerator in deceleration mode using different values for the phase angle [83], we obtain packets of

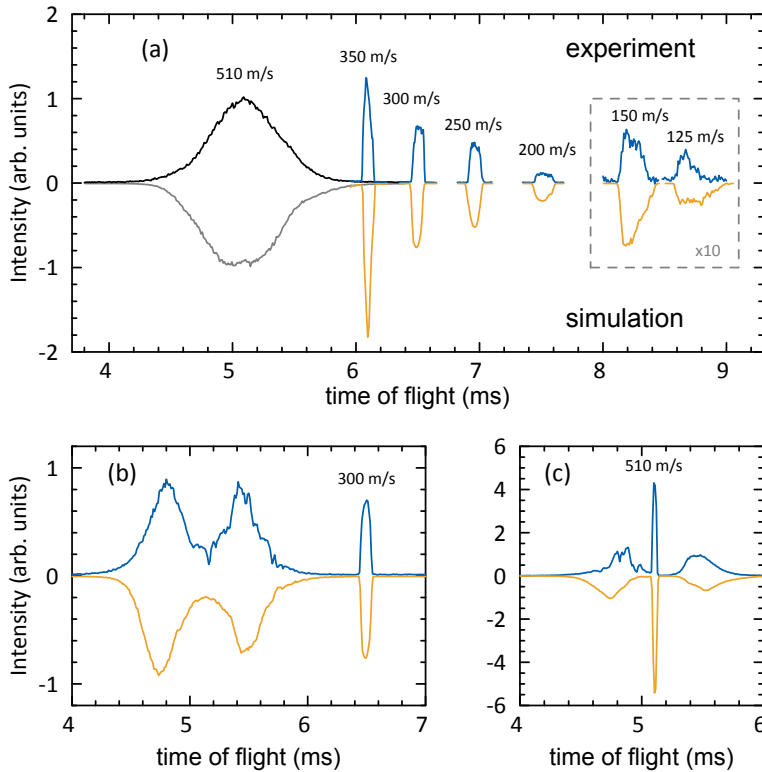


Figure 6.3: (a) TOF profiles of atomic oxygen ($2p^4\ ^3P_2$) detected with the MCP. Experimental traces are shown in the top half of the graph, simulated profiles in the bottom half. The intensity is normalized to the non-decelerated beam (black). For the decelerated peaks, only the selected part of the beam was measured, around the final mean velocity of the deceleration sequence. The intensity of the two slowest packets has been magnified by a factor of 10, for clarity. (b) Full TOF profiles after deceleration to a final mean velocity of 300 m/s. (c) Full TOF profiles of the atomic oxygen guided at 510 m/s.

O-atoms at the velocities 350 m/s, 300 m/s, 250 m/s, 200 m/s, 150 m/s and 125 m/s. At 125 m/s, the total kinetic energy of the packet has been reduced by approximately 95%. Further deceleration will show no apparent signal peak in the TOF profile, as the packet is over-focused by the hexapoles [50]. The full TOF profile for a beam decelerated to 300 m/s can be seen in Figure 6.3b.

The velocity composition of the decelerated peaks can be accurately determined with the use of particle trajectory simulations. At the higher velocities, the resulting beams are intense and already well-separated from the remaining

atoms in the molecular beam. The more decelerated atoms are focused less in the longitudinal direction, resulting in reduced intensity of the peaks. Additionally, at the lowest velocities, the travel time between hexapoles can be more than the transverse oscillation time, resulting in oxygen atoms escaping the magnetic confinement of the decelerator.

By operating the solenoids in the hybrid mode, a range of final mean velocities close to the initial mean velocity of the beam can be produced [83]. This mode of operation yields the highest particle densities and allows for the transport of particles through the decelerator at constant speed. The TOF profile that is observed when O atoms are guided at a speed of 510 m/s can be seen in Figure 6.3c. The maximum intensity is significantly larger than the decelerated beams, reflecting the greater longitudinal acceptance of this mode.

6.3.2 Oxygen molecules

The electronic ground state of O₂ is $X^3\Sigma_g^-$, with two unpaired spins resulting in a maximum magnetic moment for the lowest rotational state of two Bohr magneton. The magnetic-moment-to-mass ratio is therefore only one third of that in ground state atomic oxygen. Nevertheless, with the 100-solenoid decelerator used in our experiments, this species can be effectively decelerated. However, we require an initially slower beam to reach final velocities that are well separated in time from the non-decelerated beam. Using a mixture of 10% O₂ in Kr and cooling the valve to 200 K, the initial mean velocity of the molecular beam is around 350 m/s. In Figure 6.4a we show the various decelerated peaks of oxygen molecules in the $X^3\Sigma_g^-, J = 2$ state. From the initial mean velocity of 350 m/s, we decelerate to mean velocities of 250 m/s, 225 m/s, 200 m/s, 175 m/s and 150 m/s. At 150 m/s, the kinetic energy is reduced by 80%. In Figure 6.4b, we show the observed TOF profile when the decelerator is used in hybrid mode to select and transport a packet with a mean velocity of 350 m/s. These results are well reproduced by simulations. We observe an over-estimation of the peak intensity in the simulations for the 350 m/s packet, and attribute this to the idealized Gaussian distributions assumed for the initial beam in the simulation, that most likely do not accurately capture the actual molecular beam distribution present in the experiment.

6.3.3 State distribution

For both atomic and molecular oxygen, the Zeeman decelerator can be used to select a single quantum state, typically the state with the largest magnetic dipole moment. In atomic oxygen this is the 3P_2 spin-orbit component of the 3P_J electronic ground state and for molecular oxygen this is the $J = 2$ rotational level of the $X^3\Sigma_g^-$ state in the $N = 1$ rotational ground state. Note that following common convention in nomenclature, J is used here to indicate the spin-orbit component

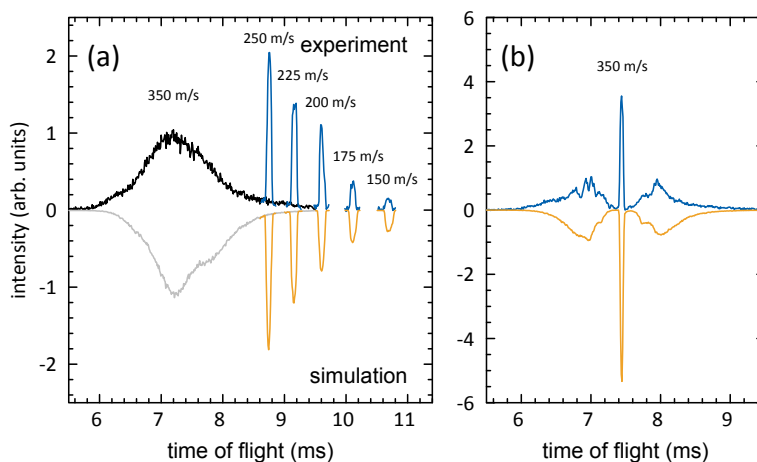


Figure 6.4: (a) TOF profiles of oxygen molecules ($X^3\Sigma_g^-$) exiting the decelerator. Experimental traces are shown in the top half and simulated profiles in the bottom half. The intensity is normalized to the non-decelerated beam (black), which was produced with a mean velocity of 350 m/s. For the decelerated peaks, only the selected part of the beam is shown with corresponding mean velocity. (b) Full TOF profiles of molecular oxygen guided at 350 m/s.

of the 3P ground state of O, as well as to indicate the spin-rotational energy levels of O_2 .

In Figure 6.5 we show the measured REMPI transitions of oxygen atoms from the electronic ground state. In the top half, the spectrum is measured after the beam has been guided by the multistage Zeeman decelerator at a speed of 510 m/s. The spectrum in the bottom half was measured without the decelerator. For this measurement, the ELV was placed in a second source chamber connected to the detection chamber, with a 3-mm diameter skimmer to collimate the beam. In both beams, the atoms mostly occupy the ground state ($J = 2$), with less than 1% of the signal intensity corresponding to population in the $J = 1$ and $J = 0$ spin-orbit states. In the guided beam, the relative population of the $J = 2$ state is enhanced due to the state-selecting properties of the multistage Zeeman decelerator. In Figure 6.6 the spectrum of O_2 is shown, again obtained from the supersonic beam with and without the decelerator to guide the beam. In this case, the Zeeman decelerator is operated to select and guide a packet with a mean velocity of 350 m/s. Since the $J = 0$ rotational energy level is the absolute ground state, it is the most populated state in the conventional beam. However, after passing through the multistage Zeeman decelerator, this state is absent from the spectrum. This is due to the slight high-field seeking Zeeman shift of this state (as seen in Figure 2.2c),

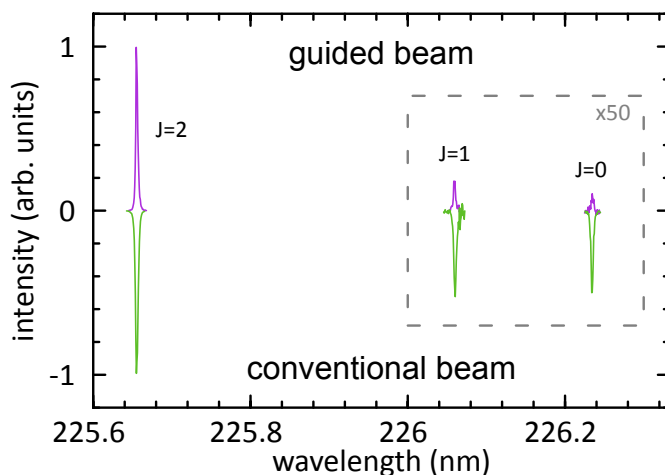


Figure 6.5: The experimental REMPI transitions of atomic oxygen from the three spin-orbit levels in the electronic ground state ($2p^4\ ^3P_J$) to the excited state ($2p^33p^1\ ^3P_J$). The peaks in the top half correspond to the beam that was manipulated by the Zeeman decelerator, while the spectrum in the bottom half was measured from the ELV in the secondary source chamber connected directly to the detection chamber. The intensity of the peaks for the $J = 1$ and $J = 0$ levels are magnified 50 times, for clarity.

resulting in transverse defocusing by the hexapole array.

With the decelerator we select the most low-field-seeking $M = 2$ projection of the $J = 2$ state, while also transmitting the low-field-seeking $M = 1$ state. However, due to an insufficient magnetic field between the end of the decelerator and the detection area, the M -states become degenerate and redistribute before they are detected. Experimentally, they become indistinguishable. However, simulations allow us to identify contributions of different M states to the TOF profiles. This can be used to predict the state-purity of the decelerated beams. As an example, TOF profiles of atomic oxygen in the $M = 1$ and $M = 2$ states are shown separately in Figure 6.7, using the simulated deceleration and guiding profiles from Figure 6.3. After deceleration to 300 m/s, oxygen atoms in the $M = 2$ state are shown to be completely separated from those in the $M = 1$ state. We can also conclude that oxygen atoms in the $J = 1$ state are filtered out of this decelerated beam, since their spin-orbit level does not have a $M = 2$ projection. With the guiding sequence, both low-field-seeking M -states are transmitted, though the accepted velocity spread is slightly larger for oxygen atoms in the $M = 2$ state.

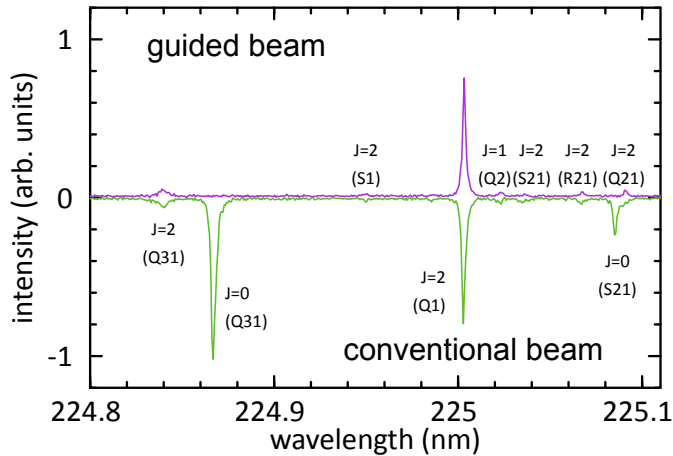


Figure 6.6: The spectrum of molecular oxygen in the ground state ($X^3\Sigma_g^-$) ionized via the 3d Rydberg levels in a 2+1 REMPI transition. The top half corresponds to the beam that was manipulated by the Zeeman decelerator, while the spectrum in the bottom half was again measured from the ELV in the secondary source chamber. The signal intensity was scaled such that the peaks at 225 nm were equal in intensity. Initial J states and transitions were assigned using a simulated spectrum.

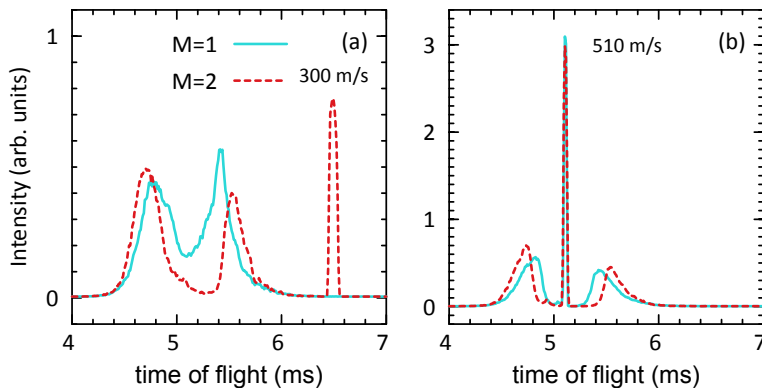


Figure 6.7: Simulated TOF profiles of oxygen atoms (3P_2) of (a) deceleration and (b) guiding sequences. The TOF profiles for the low-field-seeking states $M = 1$ and $M = 2$ are shown separately as the solid and dashed lines, respectively. Atomic oxygen in the $M = 0$ state is not shown, because it is not focused by the hexapole array and therefore negligible in intensity. High-field-seeking $M = -1, -2$ states are defocused by the hexapole array, and therefore do not reach the end of the decelerator.

6.4 Conclusions and Outlook

Beams of oxygen atoms are decelerated for the first time with a multistage Zeeman decelerator, producing packets of O atoms in a single spin-orbit state and with a well-defined and tunable velocity. We further characterized the performance of the decelerator using a seeded beam of molecular oxygen. The results presented here show that the Zeeman decelerator concept of using an alternating array of hexapoles and solenoids is truly phase stable, and decelerators using this concept may in principle be constructed with arbitrary length.

The decelerator presented here allows for the production of high-density, state-selected and velocity-tunable packets of atoms or molecules. The variety of species that can be used range from the relatively light species O, O₂ and NH, to heavier species like CaF, SrF and MnH. These species are prime candidates for controlled and low-temperature scattering studies. For instance, the velocity-controlled packets of O atoms demonstrated here are ideally suited to study low-energy inelastic or reactive collisions for a variety of benchmark systems. Theoretical predictions for inelastic O + He [107] and O + H [108] that either excite or de-excite O atoms from one spin-orbit state to another suggest that rich quantum phenomena like scattering resonances can be explored at low energies and at energies around the threshold for spin-orbit excitation [109]. The O (³P) + OH(X ²Π) → O₂(X ³Σ_g⁺) + H (²S) reaction is the inverse of "the single most important combustion reaction" [110], and is of pivotal importance to gas phase processes in atmospheres and in interstellar clouds. Theoretically, a spectacular increase in reaction rate for decreasing collision energies was predicted [111], although major discrepancies between theory and experiment exist at high collision energies for which experimental data is available [112]. The controlled packets of Zeeman-decelerated O atoms that are now available offer exciting prospects to experimentally study these processes with unprecedented sensitivity and precision.

7

Conclusions and Outlook

In chapter 3 we showed that the transverse and longitudinal motions of particles in a multistage Zeeman decelerator can be decoupled by using dedicated and spatially separated elements for transverse and longitudinal focusing. In this manner, the phase-stable operation of a multistage Zeeman decelerator can be achieved. Our concept evolved around the inclusion of magnetic hexapoles between the solenoids, as the transverse focusing elements. Numerical trajectory simulations were used to analyze the 6D phase-space distributions of controlled NH molecules in the LFS ground state. The transverse and longitudinal distributions were studied when the decelerator was operated in three distinct modes: acceleration, deceleration and hybrid mode. The transverse velocity spread was confirmed to be independent of these modes. In the longitudinal phase-space distributions, no losses due to parametric amplification were found. This is confirmed by a phase-stability diagram, in which no significant part of the phase-space distribution occupied an unstable region.

The inclusion of magnetic hexapoles between solenoids resulted in zero magnetic field regions inside the solenoids that could not be avoided by overlapping the magnetic fields of adjacent solenoids, as in earlier Zeeman decelerator designs [30, 57]. These zero-field regions could promote Majorana spin-flip transitions that effectively reduce the number of transmitted particles in the decelerator. In order to prevent this, a lingering current was introduced in the simulated current profiles. This low-level current was chosen to be sufficient to provide a 0.1-T field for the decelerated packet of molecules, while barely affecting the longitudinal forces.

Further analysis of the decelerated beams at low velocities shows that a rapid drop in particle density occurs below velocities of 160 m/s. These losses were attributed to over-focusing effects in the hexapole array. Some options were proposed to mitigate this effect, but not further explored, as extremely low beam velocities are not a requirement for crossed-beam scattering experiments.

From this promising concept a prototype design was created and implemented: a multistage Zeeman decelerator with 25 magnetic hexapoles and 24 solenoids in

an alternating array. The resulting proof-of-principle experiments performed with metastable helium beams were described in chapter 4. The prototype features a unique solenoid design, where the solenoid is created from copper capillary wound around a 3-mm bore axis. The rise and fall times of the currents in these solenoids were found to be longer than originally envisioned. However, as long as these current profiles were taken into account when calculating the decelerator pulse sequence, no adverse effects were found in the resulting beam profiles. The magnetic hexapoles were constructed from six permanent magnets in a ring assembly. While electromagnetic hexapoles were considered, similar beam densities were ultimately obtained with the two hexapole designs. Since permanent magnets require no additional driving electronics or cooling, they were chosen over the tunable electromagnetic hexapoles.

With the prototype design we were able to test the characteristics of our multistage Zeeman decelerator on beams of metastable helium atoms. We demonstrated the deceleration, acceleration and guiding at constant speed of a beam of metastable helium atoms. Excellent agreement was found between experimental and simulated time-of-flight profiles, proving that this type of multistage Zeeman design is viable. It was shown that the electrical pinhole discharge on an Even-Lavie valve produced metastable helium dimers, which we were able to separate in time from the metastable helium atoms with a deceleration sequence. This demonstrated that the decelerator is not only capable of selecting a distinct velocity distribution from the atomic beam, it is also selective to different mass-over-magnetic-moment ratios. The decelerated TOF profiles demonstrated the limitations of a relatively short decelerator, namely the incomplete separation of the phase-stable and unstable part of the metastable helium beams. In addition, the narrow decelerator tube that was used in this design provided only limited pumping capacity, resulting in reduced signal at 10 Hz repetition rate.

With our new concept validated, a finalized version of our multistage Zeeman decelerator was developed. The final design consisted of a 3-meter long decelerator of 100 solenoids and 100 hexapoles. With the lessons learned from the prototype, the design of the new vacuum chamber was modified to allow an extension to 100 stages. With the decision to only use permanent magnetic hexapoles, the new design could house all the hexapoles from the bottom of the decelerator tube, opening up the top part to accommodate a direct connection to a turbomolecular pump. The decelerator was built from multiple modules, each housing 20 solenoids and 19 hexapoles. Modules can be added or subtracted as required for a particular experiment. The solenoid-hexapole sequence remains unbroken due to a hexapole insert between the modules that simultaneously acts as a dowel between them. Since the alignment of the solenoids and hexapole is fixed, highly accurate machining of the connecting surfaces of the decelerator was required. The necessary accuracy was obtained with the use of computer-controlled milling

machines to shape the aluminium vacuum chambers. With the improved vacuum chamber design, experimental repetition rates of 30 Hz could be routinely achieved.

Beams of four kinds of metastable rare gas atoms were used to test the transverse focusing properties of the magnetic hexapole array. In this way, particles with different mean velocities and mass-to-magnetic-moment ratios were tested with no major change to the beam production method. The transverse spatial maps of the different particle beams were analyzed when the decelerator was operated in hybrid mode and when the decelerator was inactive. No significant change was found in these distributions, indicating that the transverse motion is largely independent from the longitudinal motion induced by the solenoids in this multistage Zeeman decelerator design. The experimental distributions were matched with simulated results, which were used to explain an unexpected narrowing in the helium distribution due to an incomplete filling of the transverse separatrix.

As a further characterization of our 100-stage Zeeman decelerator, the longitudinal velocity components were analyzed in two distinct beams: atomic oxygen and molecular oxygen. While molecular oxygen possessed more than twice the mass-to-magnetic-moment ratio of ground state oxygen atoms, both could be readily decelerated to a large range of final mean velocities. From atomic oxygen, initially traveling with a mean velocity of 510 m/s, more than 95% of the initial kinetic energy could be removed. For oxygen molecules traveling at an initial mean velocity of 350 m/s, about 80% could be removed before the decelerator had reached its limits. As opposed to the decelerated profiles obtained from the prototype, these decelerated profiles showed a clear separation between the phase-stable part and remaining part of the atomic and molecular beams. The velocity spread of decelerated and guided packets was accurately matched in time-of-flight profiles from trajectory simulations. Thus, we have shown an accurate prediction of the longitudinal distributions for the atomic and molecular oxygen beams. Together with the characterization of the transverse phase-space distributions of the metastable rare gas beams, a complete understanding of the 6D phase-space distributions was demonstrated for our new multistage Zeeman decelerator design. This understanding will be key in accurate calculations of the collision energies in future scattering experiments using our multistage Zeeman decelerator.

7.1 Scattering experiments

We created packets of decelerated oxygen atoms and molecules that are well-defined in both longitudinal and transverse phase-space with the use of trajectory simulations. These beams are in theory ideally suited to scattering experiments. Some preliminary scattering experiments were performed between beams

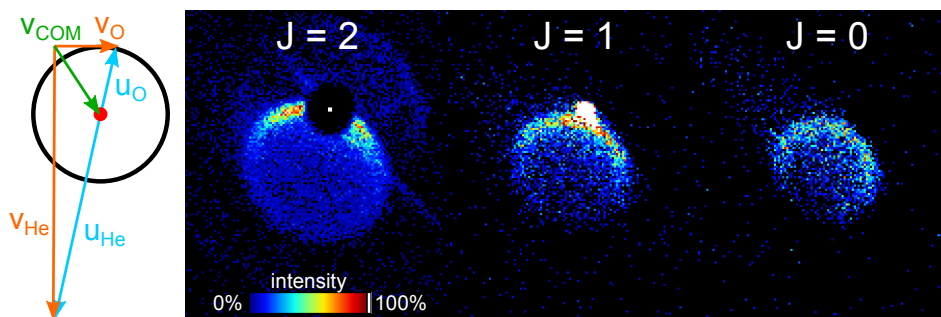


Figure 7.1: Results of preliminary scattering experiments, using a false-color scale for the intensity. Velocity maps of the elastic ($J = 2$) and inelastic ($J = 1, 0$) scattering distribution after collisions between O (3P_2) and He. Single ion positions on the detection screen were accurately assigned using centroiding. As a side-effect of this method, all beamspot signal in the native O (3P , $J = 2$) beam is accumulated in a single point, due to overlapping ions. A Newton diagram is shown on the left side, to indicate the velocity vectors of the oxygen and helium in the lab frame and center-of-mass (COM) frame, as well as the ring on which most of the elastic scattering signal ends up in a 2D projection of the 3D sphere.

of Zeeman-decelerated oxygen atoms and a conventional supersonic beam of helium. In this proof-of-principle experiment, the goal was to measure the first elastic and inelastic collision signals with a Zeeman-decelerated beam. We used velocity map imaging (VMI) to measure the Newton rings of atomic oxygen that collided with helium atoms under a 90-degree collision angle. The results can be seen in Figure 7.1. With the REMPI detection scheme described in section 2.4.2 we were able to state-selectively detect oxygen atoms that underwent elastic scattering ($J = 2$) and inelastic scattering ($J = 1$ and $J = 0$). The Zeeman decelerator was operated in the hybrid guiding mode around a mean velocity of 550 m/s, in order to obtain maximum oxygen density. The helium beam was expanded at room temperature and traveled at about 2000 m/s. In the guided beam about 1% of the oxygen was in the low-field-seeking $J = 1$ state, resulting in both elastic and inelastic collision signal for this channel. However, the scattered signal from inelastic collisions seems to dominate, as the Newton circle does not pass through the beam spot position, as would be expected for elastic scattered signal. For the $J = 0$ channel of the scattering process, pure inelastic scattering is clearly visible. These results show that sufficient density is produced by the multistage Zeeman decelerator for collisions with a secondary beam to occur reliably. However, in the results presented in Figure 7.1, there is significant blurring of the velocity resolution due to sub-optimal detection. Specifically, the REMPI scheme that was used in these experiments resulted in 40 m/s recoil velocity. While this is acceptable when

measuring the integral cross sections (ICSs), in order to measure high-resolution differential cross sections (DCSs), a suitable recoil-free REMPI scheme is required for the measured product.

There are several candidates for future scattering experiments, such as NH ($X^3\Sigma$, $N = 0$, $J = 1$), NO ($X^2\Pi_{3/2}$, $J = 3/2$), O₂ ($X^3\Sigma_g^-$, $N = 1$, $J = 2$). Of these, only NO has a well-known recoil-free REMPI scheme. For the other particles, and also for oxygen atoms, a recoil-free REMPI scheme is required before accurate measurements can be made of DCSs in scattering experiments.

7.2 Merged beams

Because it is constructed from separate elements, the multistage Zeeman decelerator has a relatively open structure compared to a Stark decelerator, which typically consists of mechanically connected electrodes. This presents the opportunity to create some interesting geometries with the Zeeman decelerator. For instance, a curved section of the decelerator can be used to filter out the carrier gas from the initial molecular beam. This would reduce the amount of background collisions in the final experiment and thereby increase the signal-to-noise ratio. Such a curved section could also be used to introduce a secondary neutral beam at zero or near-zero collision angle. Such merged beam experiments have been performed in the past, typically using an electric or magnetic guide [90]. Bertsche *et al.* were able to reach collision energy as low as 100 mK by merging two supersonic expansions using an electric and magnetic guide and matching the two velocities [113]. They measured Penning ionization rates between beams of metastable neon in the magnetic guide and NH molecules in the electric guide. Henson *et al.* merged a beam of metastable helium in a magnetic quadrupole guide with a straight beam of H₂, which allowed them to measure Penning ionization rates at collision energies down to 10 mK [105]. The combination of a multistage Zeeman decelerator with merged beam detection is an exciting prospect for ultra-cold collision experiments.

A One dimensional model for phase stability

Here we present two models for longitudinal phase stability, which were developed by Wiederkehr *et al.* [58] and Dulitz *et al.* [40], and test them with trajectory simulations of our decelerator concept.

First, Wiederkehr pioneered the 1D phase-space model for multistage Zeeman deceleration. In this model, the motion of a particle relative to the synchronous particle is described by:

$$\frac{mL}{\pi} \frac{d^2 \Delta \phi}{dt^2} + \frac{1}{L} (W(\phi_0 + \Delta \phi) - W(\phi_0)) = 0, \quad (\text{A.1})$$

where m is the mass of the particle, L is the distance between solenoid centers, $\Delta \phi$ is the instantaneous phase angle and $W(\phi)$ is the Zeeman energy in a solenoid. With this formula we can calculate the average relative forces acting on the decelerated particles by comparing their Zeeman potential energies with that of the synchronous particle, at the moment of switching. Performing numerical integration on formula A.1 yields the separatrices that should enclose the stable longitudinal phase-space for a given ϕ_0 . This model uses only the static magnetic fields, not taking into account the changing magnetic fields during the $8\text{-}\mu\text{s}$ switching time. This assumption is not completely unreasonable given that we use switching times that are $4\text{ }\mu\text{s}$ early, to compensate the additional deceleration the particles experience during the current fall period, as explained in section 3.2.

The second model was introduced by Dulitz *et al.*, which evaluated the mean longitudinal acceleration in more detail. The average acceleration is obtained via numerical time integration over one deceleration period, T , which corresponds to the synchronous particle traveling a distance L . This method can be used to evaluate both the longitudinal and transverse acceleration:

$$\bar{a}_i(\phi(t), r) = \frac{1}{T} \int_0^T a_i(\phi(t), r, t) dt, \quad (\text{A.2})$$

where a_i is either the longitudinal ($i = \phi$) or transverse ($i = r$) acceleration. The numerical integration is performed in small time steps in the same manner that the

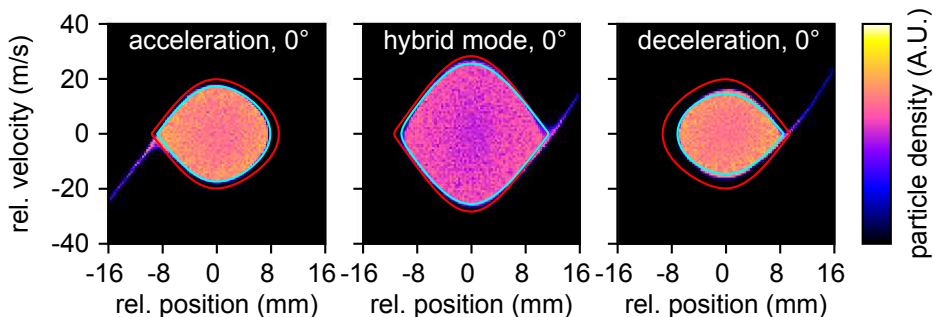


Figure A.1: Longitudinal phase-space diagrams of the three operation modes using $\phi_0 = 0^\circ$, copied from Figure 3.5. The diagrams show the separatrices determined with the Wiederkehr model (red) and the Dulitz model (cyan).

trajectory simulations are performed. With the mean acceleration as a function of the phase angle, the separatrices are determined by calculating the largest stable orbit around the synchronous particle.

With this method small details of the magnetic field are taken into account, such as the lingering currents and the resulting overlap between current profiles of adjacent solenoids. This model is based on the assumption that the longitudinal velocity does not change significantly in one period, T . The relative change in velocity per stage is small enough for this to be a good approximation (unless the beam itself is slow, then the relative change can be significant per stage). Calculations with this model require more computational power compared to the previous model, where the fields were only evaluated at two points in time (before and after switching). However, this method yields a more accurate prediction of the stable trajectories and thus the phase-space acceptance.

We obtain separatrices for acceleration, deceleration and hybrid mode with both models and compare them with the trajectory simulations (Figure A.1). Even with the early switching times for the solenoids, the Wiederkehr model consistently overestimates the longitudinal phase-space acceptance, while the Dulitz model shows excellent agreement. Therefore, despite the longer computational times, the Dulitz model is used to evaluate separatrices in longitudinal phase-space.

B

Extreme equilibrium phase angles

As can be seen in Figure 3.3*b*, the highest acceptance is found with $\phi_0 = -90^\circ$ in deceleration mode or $\phi_0 = 90^\circ$ in acceleration mode. This is a surprising result if we consider conventional multistage Zeeman decelerators. In these decelerators, the inherent transverse defocusing fields outside the solenoids prevent the effective use of these extreme values of ϕ_0 [57]. However, with the addition of magnetic hexapoles this limitation no longer exists. Indeed, the total acceptance changes almost solely with the longitudinal acceptance. This acceptance increases in deceleration and acceleration mode with lower and higher ϕ_0 , respectively. We show this for deceleration mode in Figure B.1*a*.

In the negative ϕ_0 range of deceleration mode the solenoids are turned off early, resulting in only a small amount of deceleration per stage. This is reflected in the kinetic energy change with this mode shown in Figure 3.3*a*. With lower ϕ_0 , less of the slope of the solenoid field is used to decelerate, and more of it is available for longitudinal focusing of the particle beam.

Moreover, the minimum value of $\phi_0 = -90^\circ$ is an arbitrary limit, as lower values of ϕ_0 result in even less deceleration and more longitudinal acceptance. Nevertheless, it is important to remember that this is a theoretical prediction, with the important assumption that the decelerator is of sufficient length that the slower particles have sufficient time to catch up with the synchronous particle. With less deceleration of the synchronous particle per solenoid, this catch-up time will increase. This is reflected in the difference in longitudinal phase-space distributions after 100 and 200 stages in panels *b* and *c* of Figure B.1, respectively. In these simulations (similar to those shown in Figure 3.5) a block distribution of $\text{NH}(X^3\Sigma^-, N = 0, J = 1)$ particles was used that well exceeded the predicted longitudinal separatrix. After 100 stages, the (deformed) corners of the initial block distribution are still visible as they revolve around the synchronous particle in longitudinal phase-space. Only after 200 stages of deceleration have these unaccepted particles had enough time to spatially separate from the particles with stable trajectories. This graph also shows that the prediction of the separatrix is quite accurate, and the uniformity of the particle distribution within is evidence

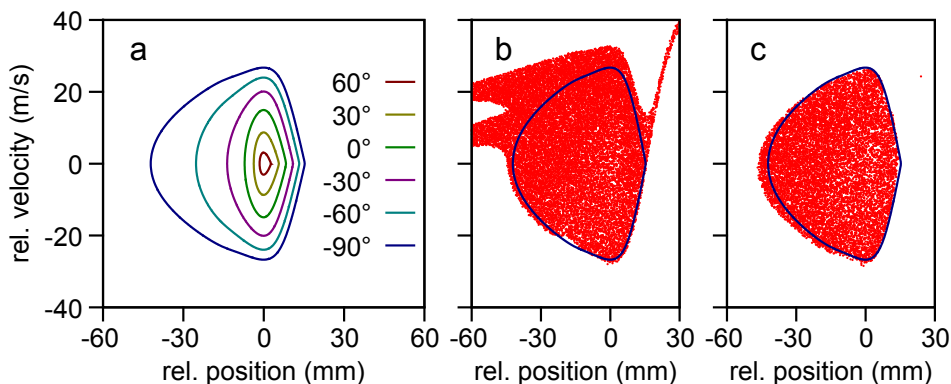


Figure B.1: Longitudinal phase-space diagrams showing the effect of negative ϕ_0 in deceleration mode. (a) shows the separatrices of this mode with different ϕ_0 , from 60° to -90° in steps of 30° . (b,c) show the results of 3D trajectory simulations of deceleration mode with $\phi_0 = -90^\circ$ after 100 and 200 deceleration stages, respectively. The graph is filled with dots that represent molecules of $\text{NH}(X^3\Sigma^-, N = 0, J = 1)$. These particles were initially distributed with a block function that well exceeded the separatrix.

of phase stability, even with these extreme values of ϕ_0 . In acceleration mode, a similar rise in acceptance can be found with increasing ϕ_0 , which is evident in Figure 3.3b.

Bibliography

- [1] J. Lennard-Jones and G. Hall, in *Roy. Soc. Lond. A*, Vol. 106 (1924) p. 441.
- [2] F. Knauer, *Zeitschrift für Physik* **80**, 80 (1933).
- [3] L. F. Broadway, in *Roy. Soc. Lond. A*, Vol. 141 (1933) pp. 634–641.
- [4] D. R. Herschbach, *Angew. Chem.* **26**, 1221 (1987).
- [5] Y. T. Lee, *Angew. Chem.* **26**, 939 (1987).
- [6] A. Kantrowitz and J. Grey, *Rev. Sci. Instrum.* **22**, 328 (1951).
- [7] R. deCarvalho, J. M. Doyle, B. Friedrich, T. Guillet, J. Kim, D. Patterson, and J. D. Weinstein, *Eur. Phys. J. D* **7**, 289 (1999).
- [8] M. Gupta and D. Herschbach, *J. Phys. Chem. A* **103**, 10670 (1999).
- [9] N. Abuaf, J. B. Anderson, R. P. Andres, J. B. Fenn, and D. G. H. Marsden, *Science* **155**, 997 (1967).
- [10] T. Hänsch and A. Schawlow, *Optics Communications* **13**, 68 (1975).
- [11] D. J. Wineland and W. M. Itano, *Phys. Rev. A* **20**, 1521 (1979).
- [12] M. D. Di Rosa, *Eur. Phys. J. D* **31**, 395 (2004).
- [13] I. Kozyryev, L. Baum, K. Matsuda, and J. M. Doyle, *Chem. Phys. Chem.* **17**, 3641 (2016).
- [14] J. F. Barry, D. J. McCarron, E. B. Norrgard, M. H. Steinecker, and D. DeMille, *Nature* **512**, 286 (2014).
- [15] M. H. Steinecker, D. J. McCarron, Y. Zhu, and D. DeMille, *Chem. Phys. Chem.* **17**, 3664 (2016).
- [16] L. Anderegg, B. L. Augenbraun, Y. Bao, S. Burchesky, L. W. Cheuk, W. Ketterle, and J. M. Doyle, *Nature* **14**, 890 (2018).
- [17] E. Narevicius, A. Libson, M. F. Riedel, C. G. Parthey, I. Chavez, U. Even, and

- M. G. Raizen, Phys. Rev. Lett. **98**, 103201 (2007).
- [18] B. K. Stuhl, M. T. Hummon, and J. Ye, Ann. Rev. Phys. Chem. **65**, 501 (2014).
- [19] M. Brouard, D. H. Parker, and S. Y. T. van de Meerakker, Chem. Soc. Rev. **43**, 7279 (2014).
- [20] S. Y. T. van de Meerakker, H. L. Bethlem, N. Vanhaecke, and G. Meijer, Chem. Rev. **112**, 4828 (2012).
- [21] H. L. Bethlem, G. Berden, and G. Meijer, Phys. Rev. Lett. **83**, 1558 (1999).
- [22] E. Narevicius and M. G. Raizen, Chem. Rev. **112**, 4879 (2012).
- [23] S. D. Hogan, M. Motsch, and F. Merkt, Phys. Chem. Chem. Phys. **13**, 18705 (2011).
- [24] L. D. Carr, D. DeMille, R. V. Krems, and J. Ye, New J. of Phys. **11**, 055049 (2009).
- [25] M. T. Bell and T. P. Softley, Mol. Phys. **107**, 99 (2009).
- [26] J. Jankunas and A. Osterwalder, Ann. Rev. Phys. Chem. **66**, 241 (2015).
- [27] R. Krems, W. Stwalley, and B. Friedrich, eds., *Cold Molecules: Theory, Experiment, Applications* (Taylor and Francis, 2009).
- [28] W. Gerlach and O. Stern, Zeitschrift Fur Physik **8**, 110 (1921).
- [29] N. Vanhaecke, U. Meier, M. Andrist, B. H. Meier, and F. Merkt, Phys. Rev. A **75**, 031402(R) (2007).
- [30] S. D. Hogan, D. Sprecher, M. Andrist, N. Vanhaecke, and F. Merkt, Phys. Rev. A **76**, 023412 (2007).
- [31] E. Narevicius, C. G. Parthey, A. Libson, J. Narevicius, I. Chavez, U. Even, and M. G. Raizen, New J. Phys. **9**, 358 (2007).
- [32] E. Narevicius, A. Libson, C. G. Parthey, I. Chavez, J. Narevicius, U. Even, and M. G. Raizen, Phys. Rev. A **77**, 051401(R) (2008).
- [33] A. Wiederkehr, H. Schmutz, M. Motsch, and F. Merkt, Mol. Phys. **110**, 1807 (2012).
- [34] E. Lavert-Ofir, L. David, A. B. Henson, S. Gersten, J. Narevicius, and E. Narevicius, Phys. Chem. Chem. Phys. **13**, 18948 (2011).
- [35] Y. Liu, M. Vashishta, P. Djuricanin, S. Zhou, W. Zhong, T. Mittertreiner, D. Carty, and T. Momose, Phys. Rev. Lett. **118**, 093201 (2017).
- [36] Y. Liu, S. Zhou, W. Zhong, P. Djuricanin, and T. Momose, Phys. Rev. A **91**,

-
- 021403 (2015).
- [37] N. Akerman, M. Karpov, Y. Segev, N. Bibelnik, J. Narevicius, and E. Narevicius, *Phys. Rev. Lett.* **119**, 073204 (2017).
- [38] A. Trimeche, M. Bera, J.-P. Cromières, J. Robert, and N. Vanhaecke, *Eur. Phys. J. D* **65**, 263 (2011).
- [39] K. Dulitz, M. Motsch, N. Vanhaecke, and T. P. Softley, *J. Chem. Phys.* **140**, 104201 (2014).
- [40] K. Dulitz, N. Vanhaecke, and T. P. Softley, *Phys. Rev. A* **91**, 013409 (2015).
- [41] K. Dulitz, A. Tauschinsky, and T. P. Softley, *New J. Phys.* **17**, 035005 (2015).
- [42] K. Dulitz, J. Toscano, A. Tauschinsky, and T. P. Softley, *J. Phys. B* **49**, 075203 (2016).
- [43] J. Toscano, A. Tauschinsky, K. Dulitz, C. J. Rennick, B. R. Heazlewood, and T. P. Softley, *New J. Phys.* **19**, 083016 (2017).
- [44] T. Momose, Y. Liu, S. Zhou, P. Djuricanin, and D. Carty, *Phys. Chem. Chem. Phys.* **15**, 1772 (2013).
- [45] L. A. McArd, A. Mizouri, P. A. Walker, V. Singh, U. Krohn, E. A. Hinds, and D. Carty, *arXiv:1807.10648* (2018).
- [46] H. L. Bethlem, G. Berden, A. J. A. van Roij, F. M. H. Crompvoets, and G. Meijer, *Phys. Rev. Lett.* **84**, 5744 (2000).
- [47] S. Y. T. van de Meerakker, N. Vanhaecke, H. L. Bethlem, and G. Meijer, *Phys. Rev. A* **73**, 023401 (2006).
- [48] B. C. Sawyer, B. K. Stuhl, B. L. Lev, J. Ye, and E. R. Hudson, *Eur. Phys. J. D* **48**, 197 (2008).
- [49] S. Y. T. van de Meerakker, N. Vanhaecke, H. L. Bethlem, and G. Meijer, *Phys. Rev. A* **71**, 053409 (2005).
- [50] L. Scharfenberg, H. Haak, G. Meijer, and S. Y. T. van de Meerakker, *Phys. Rev. A* **79**, 023410 (2009).
- [51] J. J. Gilijamse, S. Hoekstra, S. Y. T. van de Meerakker, G. C. Groenenboom, and G. Meijer, *Science* **313**, 1617 (2006).
- [52] M. Kirste, X. Wang, H. C. Schewe, G. Meijer, K. Liu, A. van der Avoird, L. M. C. Janssen, K. B. Gubbels, G. C. Groenenboom, and S. Y. T. van de Meerakker, *Science* **338**, 1060 (2012).
- [53] A. von Zastrow, J. Onvlee, S. N. Vogels, G. C. Groenenboom, A. van der

- Avoird, and S. Y. T. van de Meerakker, *Nature Chemistry* **6**, 216 (2014).
- [54] S. N. Vogels, J. Onvlee, S. Chefdeville, A. van der Avoird, G. C. Groenenboom, and S. Y. T. van de Meerakker, *Science* **350**, 787 (2015).
- [55] S. N. Vogels, T. Karman, J. Kłos, M. Besemer, J. Onvlee, A. van der Avoird, G. C. Groenenboom, and S. Y. T. van de Meerakker, *Nature Chemistry* **10**, 435 (2018).
- [56] Z. Gao, T. Karman, S. N. Vogels, M. Besemer, A. van der Avoird, G. C. Groenenboom, and S. Y. T. van de Meerakker, *Nature Chemistry* **10**, 469 (2018).
- [57] A. W. Wiederkehr, M. Motsch, S. D. Hogan, M. Andrist, H. Schmutz, B. Lambillotte, J. A. Agner, and F. Merkt, *J. Chem. Phys.* **135**, 214202 (2011).
- [58] A. W. Wiederkehr, S. D. Hogan, and F. Merkt, *Phys. Rev. A* **82**, 043428 (2010).
- [59] A. Osterwalder, S. A. Meek, G. Hammer, H. Haak, and G. Meijer, *Phys. Rev. A* **81**, 051401(R) (2010).
- [60] J. van den Berg, S. Mathavan, C. Meinema, J. Nauta, T. Nijbroek, K. Jungmann, H. Bethlem, and S. Hoekstra, *J. Mol. Spec.* **300**, 22 (2014).
- [61] P. Jansen, M. Quintero-Pérez, T. E. Wall, J. E. van den Berg, S. Hoekstra, and H. L. Bethlem, *Phys. Rev. A* **88**, 043424 (2013).
- [62] E. Lavert-Ofir, S. Gersten, A. B. Henson, I. Shani, L. David, J. Narevicius, and E. Narevicius, *New J. Phys.* **13**, 103030 (2011).
- [63] N. Akerman, M. Karpov, L. David, E. Lavert-Ofir, J. Narevicius, and E. Narevicius, *New J. Phys.* **17**, 065015 (2015).
- [64] F. M. H. Cromptoets, R. T. Jongma, H. L. Bethlem, A. J. A. van Rooij, and G. Meijer, *Phys. Rev. Lett.* **89**, 093004 (2002).
- [65] C. Vallance, *An Introduction to the Gas Phase*, 2053-2571 (Morgan & Claypool Publishers, 2017).
- [66] W. Christen and K. Rademann, *Phys. Rev. A* **77**, 012702 (2008).
- [67] F. B. Dunning and R. G. Hulet, *Atomic, Molecular and Optical Physics: Atoms and Molecules*, Vol. 29B (AP, 1996).
- [68] M. Gupta and D. Herschbach, *J. Phys. Chem. A* **105**, 1626 (2001).
- [69] O. F. Hagena and W. Obert, *J. Chem. Phys.* **56**, 1793 (1972).
- [70] L. Abad, D. Bermejo, V. J. Herrero, J. Santos, and I. Tanarro, *Rev. Sci. Instrum.* **66**, 3826 (1995).

-
- [71] J. B. Cross and J. J. Valentini, *Rev. Sci. Instrum.* **53**, 38 (1982).
- [72] D. Irimia, D. Dobrikov, R. Kortekaas, H. Voet, D. A. van den Ende, W. A. Groen, and M. H. M. Janssen, *Rev. Sci. Instrum.* **80**, 113303 (2009).
- [73] U. Even, *EPJ tech. and instrum.* **2**, 17 (2015).
- [74] B. Yan, P. F. H. Claus, B. G. M. van Oorschot, L. Gerritsen, A. T. J. B. Eppink, S. Y. T. van de Meerakker, and D. H. Parker, *Rev. Sci. Instrum.* **84**, 023102 (2013).
- [75] L. Ploenes, D. Haas, D. Zhang, S. Y. T. van de Meerakker, and S. Willitsch, *Rev. Sci. Instrum.* **87**, 053305 (2016).
- [76] M. Gryziński, *Phys. Rev.* **138**, A336 (1965).
- [77] G. E. Chamberlain and H. G. M. Heideman, *Phys. Rev. Lett.* **15**, 337 (1965).
- [78] P. Zeeman, *The London, Edinburgh, and Dublin Philosophical Magazine and Journal of Science* **44**, 55 (1897).
- [79] P. J. Mohr, D. B. Newell, and B. N. Taylor, *Journal of Physical and Chemical Reference Data* **45**, 043102 (2016).
- [80] S. S. Hodgman, R. G. Dall, L. J. Byron, K. G. H. Baldwin, S. J. Buckman, and A. G. Truscott, *Phys. Rev. Lett.* **103**, 053002 (2009).
- [81] W. Demtröder, *Molecular Physics: Theoretical Principles and Experimental Methods*, Physics textbook (Wiley, 2008).
- [82] G. Berden, R. Engeln, P. C. M. Christianen, J. C. Maan, and G. Meijer, *Phys. Rev. A* **58**, 3114 (1998).
- [83] T. Cremers, S. Chefdeville, N. Janssen, E. Sweers, S. Koot, P. Claus, and S. Y. T. van de Meerakker, *Phys. Rev. A* **95**, 043415 (2017).
- [84] H. L. Bethlem, F. M. H. Crompvoets, R. T. Jongma, S. Y. T. van de Meerakker, and G. Meijer, *Phys. Rev. A* **65**, 053416 (2002).
- [85] D. C. Morton, Q. Wu, and G. W. Drake, *Canadian Journal of Physics* **84**, 83 (2006).
- [86] A. Melamid, Z. K. Khachatryan, and A. Guzhov, *Journal of Applied Spectroscopy* **16**, 262 (1972).
- [87] A. T. J. B. Eppink and D. H. Parker, *Rev. Sci. Instrum.* **68**, 3477 (1997).
- [88] W. Li, S. D. Chambreau, S. A. Lahankar, and A. G. Suits, *Rev. Sci. Instrum.* **76**, 063106 (2005).
- [89] D. Watanabe, H. Ohoyama, T. Matsumura, and T. Kasai, *Eur. Phys. J. D* **38**, 219 (2006).

- [90] A. Osterwalder, *EPJ Techniques and Instrumentation* **2**, 10 (2015).
- [91] A. P. P. van der Poel, K. Dulitz, T. P. Softley, and H. L. Bethlem, *New J. Phys.* **17**, 055012 (2015).
- [92] J. G. Kalnins, G. Lambertson, and H. Gould, *Rev. Sci. Instrum.* **73**, 2557 (2002).
- [93] S. Y. Lee, *Accelerator physics*, 2nd ed. (World Scientific, Singapore, 2004).
- [94] J. G. van der Corput, *Proc. Akad. Wet. Amsterdam* **38**, 813 (1935).
- [95] M. Kirste, B. G. Sartakov, M. Schnell, and G. Meijer, *Phys. Rev. A* **79**, 051401 (2009).
- [96] S. A. Meek, G. Santambrogio, B. G. Sartakov, H. Conrad, and G. Meijer, *Phys. Rev. A* **83**, 033413 (2011).
- [97] T. E. Wall, S. K. Tokunaga, E. A. Hinds, and M. R. Tarbutt, *Phys. Rev. A* **81**, 033414 (2010).
- [98] D. Zhang, G. Meijer, and N. Vanhaecke, *Phys. Rev. A* **93**, 023408 (2016).
- [99] S. D. Hogan, A. W. Wiederkehr, M. Andrist, H. Schmutz, and F. Merkt, *J. Phys. B: At. Mol. Opt. Phys.* **41**, 081005 (2008).
- [100] U. Even, J. Jortner, D. Noy, N. Lavie, and C. Cossart-Magos, *J. Chem. Phys.* **112**, 8068 (2000).
- [101] M. Motsch, P. Jansen, J. A. Agner, H. Schmutz, and F. Merkt, *Phys. Rev. A* **89**, 043420 (2014).
- [102] P. Jansen, L. Semeria, L. E. Hofer, S. Scheidegger, J. A. Agner, H. Schmutz, and F. Merkt, *Phys. Rev. Lett.* **115**, 133202 (2015).
- [103] O. Chubar and P. Elleaume and J. Chavanne, “Radia 4.29,” (2009).
- [104] T. Cremers, S. Chefdeville, V. Plomp, N. Janssen, E. Sweers, and S. Y. T. van de Meerakker, *Phys. Rev. A* **98**, 033406 (2018).
- [105] A. B. Henson, S. Gersten, Y. Shagam, J. Narevicius, and E. Narevicius, *Science* **338**, 234 (2012).
- [106] R. J. Yokelson, R. J. Lipert, and W. A. Chupka, *J. Chem. Phys.* **97**, 6144 (1992).
- [107] F. Lique, J. Kłos, M. H. Alexander, S. D. Le Picard, and P. J. Dagdigan, *Monthly Notices of the Royal Astronomical Society* **474**, 2313 (2018).
- [108] E. Abrahamsson, R. V. Krems, and A. Dalgarno, *Astrophys. J.* **654**, 1171 (2007).

-
- [109] Z. Ma and K. Liu, *Chem. Phys. Lett.* **213**, 269 (1993).
- [110] D. Xie, C. Xu, T.-S. Ho, H. Rabitz, G. Lendvay, S. Y. Lin, and H. Guo, *J. Chem. Phys.* **126**, 074315 (2007).
- [111] S. Y. Lin, H. Guo, P. Honvault, C. Xu, and D. Xie, *J. Chem. Phys.* **128**, 014303 (2008).
- [112] J. Ma, S. Y. Lin, H. Guo, Z. Sun, D. H. Zhang, and D. Xie, *J. Chem. Phys.* **133**, 054302 (2010).
- [113] B. Bertsche, J. Jankunas, and A. Osterwalder, *CHIMIA International Journal for Chemistry* **68**, 256 (2014).

Summary

Since the beginning of the 19th century, it has been well understood that molecules are the building blocks of the universe. We know that these blocks are in constant motion and even in solid state, molecules are constantly vibrating in their lattice. Molecules in the gas phase are not limited in this way, and bounce around freely in their available space, undergoing constant collisions with each other. Typical molecules in the air around us move with a mean velocity of around 500 m/s and collide billions of times per second.

These collisions can affect molecules in a number of ways. They can bounce off each other and only change in direction, in a so-called elastic collision. Collisions between molecules can also result in an energy transfer between the internal states of the molecules. These are called inelastic collisions. There are also reactive collisions, in which the molecules react, forming new molecules in the process. We want to study these different type of interactions in detail.

In order to investigate collisions between molecules, a more controlled environment is required. The first step is to create pure molecular beams in a vacuum. Molecules in these beams are isolated from the outside and no longer collide billions of times per second. Now we can look at particular collisions by introducing a second molecular beam that intersects with the first beam. With laser-based detection methods we can image the products of these controlled collisions. The crux of this research is to have as much control over the initial molecules as possible, and to accurately measure the state of the molecules afterwards. In this thesis, we focused on controlling molecular beams in preparation of a collision experiment.

One method of controlling molecules is to use the interaction between molecules with a magnetic dipole moment and an external magnetic field. These types of molecules can increase or decrease in energy when entering or exiting a magnetic field, depending on the orientation of their dipole within the field. This energy shift is called the Zeeman Effect. With the use of this interaction, it is possible to control the velocity of molecules and to prepare a beam of molecules for collision experiments.

Because the Zeeman Effect is relatively weak, strong magnetic fields are re-

quired to make significant changes to the velocity of molecules. In addition, these fields need to be switched on and off rapidly, otherwise particles entering a magnetic field lose an equal amount of energy as they regain when leaving it, resulting in no change in velocity. A machine that can make this strong magnetic fields with fast switching times and apply them to decelerate (or accelerate) molecules, is called a Zeeman decelerator. The goal of the research described in this thesis is to develop a Zeeman decelerator for collision experiments in crossed molecular beams.

Zeeman decelerators have been developed in the past, but never with the specific goal of crossed molecular beam experiments. Existing designs were found not to be optimal for this type of experiment. In particular, the ratio between longitudinal and transverse focusing is inherently coupled in these models. This characteristic is not ideal for our type of experiment, which is one of the reasons that we decided to develop our own Zeeman decelerator design.

In the Zeeman decelerator design described in this thesis, the longitudinal and transverse motions are controlled independently. This is achieved by utilizing the magnetic fields in an array of alternating solenoids and magnetic hexapoles to control the molecular beam. Our new decelerator combines this feature with an efficient cooling method, which enables repetition rates of the experiment up to 30 times per second. This is made possible by using solenoids made from copper capillaries, through which a constant flow of cooling liquid is pumped.

The molecular beam can be decelerated or accelerated by changing the timings of the current pulses. A method of sending double current pulses through the solenoids was developed to guide molecular beams at constant velocity, while keeping a precise control over the velocity spread. The current pulses are generated using low-voltage electronic components. These are safer to use compared to their high-voltage counterparts. An additional benefit is that low-voltage components are generally cheaper than high-voltage components, bringing down the overall price tag of the decelerator assembly.

A theoretical study was performed to investigate the advantages and disadvantages of the new design Zeeman decelerator, and to develop the required current pulses through the solenoids. This study showed that a large amount of molecules can be decelerated per sequence, compared to most other types of Zeeman decelerator. We show that the use of magnetic hexapoles between the solenoids is an effective method to prevent instabilities in the molecular trajectories, which are typically expected in a Zeeman decelerator that consists of exclusively solenoids. We also demonstrated that a small lingering current in the solenoids can prevent so-called Majorana transitions, in which a magnetic dipole of a molecule suddenly reorients itself, changing the response of the molecule to a magnetic field. We also show that at relatively low velocities of the molecular beams, our type of Zeeman decelerator is no longer effective. At these velocities the hexapoles

focus the molecules so strongly in the transverse direction that—between the hexapoles—the molecules can escape from the decelerator.

After this theoretical study, a prototype of the Zeeman decelerator was built. The prototype consisted of 24 solenoids and 25 hexapoles. The hexapoles were each made from six permanent magnets in a ring. With this machine we were able to decelerate, accelerate and guide at constant velocity a packet of metastable helium atoms. For each of these operational modes, the resulting velocity distributions could be accurately predicted with computer simulations. For the helium atoms, there was still some overlap in arrival times for the decelerated atoms and the rest of the beam. In order to obtain complete separation between atoms with different velocities, a longer decelerator was required. We were able to show that the decelerator can separate particles with different masses and magnetic dipole moments, as was the case for metastable helium atoms and helium dimers in the decelerated beams.

The finalized Zeeman decelerator features a modular design, in which each module consists of a vacuum chamber with room for 20 solenoids and 20 hexapoles. These modules can be individually pumped using turbo-molecular pumps to improve the vacuum conditions compared to the prototype model. This modular design allows us to adapt the length of the decelerator to fit any experiment. This finalized design is described in detail, with extra attention to the development process of the solenoids. These elements have to be carefully constructed, as they determine the alignment of the decelerator, which contains a free diameter that is limited to 3 mm.

Of this design, five modules are built and assembled in the lab, for a total of 100 solenoids and 101 hexapoles. This decelerator was used for a number of experiments with different atoms and molecules. Four noble gas atoms—helium, neon, argon and krypton—were used to map the transverse velocity spread at the end of the decelerator. This allowed us to determine the transverse focusing properties of the hexapole array. We were also able to test the guiding sequences for these atoms at very different longitudinal velocities. The direct mapping of the metastable rare gas atoms was possible due to the large internal energy in their first electronically excited state, which results in a measurable response when they hit a microchannel plate detector.

Finally, experiments were performed with oxygen atoms and oxygen molecules. Both particles have a significant magnetic dipole moment in their lowest energy state, but they differ in mass by a factor of two. Since the detection method of both particles is quite similar, we could easily switch between these two species. Different sequences for both oxygen atoms and molecules were used to test the decelerating capabilities of the Zeeman decelerator. These experiments showed that a large range of final mean velocities were possible for particles of different magnetic dipole moment over mass, and that an extension of the decelerator to

arbitrary length is possible without introducing additional losses in the particle beams.

In this thesis the design of a new type of Zeeman decelerator is described, a machine that can be used to control beams of molecules with a magnetic dipole moment. This decelerator was designed for molecular collision experiments in crossed beams. We describe the first experiments performed with this type of Zeeman decelerator. The transverse and longitudinal motions are independent in this decelerator, and they are characterized as such. In these experiments we show that atomic and molecular beams can be prepared with controllable velocity distributions, in a single quantum state. This machine enables crossed beam collisions experiments with magnetic molecules and atoms with high energy resolution. This is an important step in the ongoing research of fundamental molecular interactions.

Samenvatting

Sinds het einde van de 19e eeuw is het universeel bekend dat moleculen de bouwblokken van het universum zijn. Deze bouwblokken zijn vrijwel constant in beweging en zelfs moleculen in vaste stoffen trillen constant op hun plek. Moleculen in gasvorm zijn niet zo beperkt, vliegen vrij door de beschikbare ruimte, en ondergaan constant botsingen met elkaar. Een gemiddeld molecuul in de lucht om ons heen beweegt met een snelheid van rond de 500 m/s en botst miljarden keren per seconde.

Deze botsingen kunnen de moleculen op verschillende manieren beïnvloeden. Zo kunnen de moleculen van elkaar af stuiteren en alleen van richting veranderen, in een zogenaamde elastische botsing. Maar in een botsing tussen moleculen kan ook energie overgedragen worden die de interne energietoestand van de moleculen verandert. Als dit gebeurt spreken we van een inelastische botsing. Verder kunnen bepaalde moleculen met elkaar reageren om nieuwe moleculen te vormen, in een reactieve botsing. Wij willen deze verschillende interacties in detail onderzoeken.

Om botsingen tussen moleculen te kunnen onderzoeken is een gecontroleerde omgeving nodig. De eerste stap is om pure moleculaire bundels te maken in een vacuüm. Moleculen in deze bundels zijn geïsoleerd van de buitenlucht en ondergaan hierdoor geen miljarden botsingen per seconde. Nu kunnen we doelgericht botsingen laten plaatsvinden door een tweede moleculaire bundel te overlappen met de eerste. Met laser detectie brengen we de producten van deze gecontroleerde botsingen in beeld. De crux van dit type onderzoek is om zo veel mogelijk controle te hebben over de moleculen voor de botsing en zo precies mogelijk hun toestand te meten na een botsing. In dit proefschrift concentreren we ons op het voorbereiden van moleculaire bundels voor botsingsexperimenten.

Eén methode om moleculen te beïnvloeden maakt gebruik van de interactie tussen moleculen die een magnetisch dipoolmoment bezitten en een extern magnetisch veld. Dit type molecuul zal versnellen of vertragen in een toenemend magnetisch veld, afhankelijk van de oriëntatie van zijn dipoolmoment. Deze interactie noemen we het Zeeman effect. Hiermee is het mogelijk om moleculen in

snelheid te veranderen, of te beperken, zodat een bundel kan worden voorbereid met een controleerbare snelheidspreiding.

Omdat het Zeeman effect relatief zwak is, zijn sterke magneetvelden nodig om significante veranderingen in de snelheid van moleculen te maken. Verder moeten de magneetvelden snel aan- en uit te schakelen zijn, anders vertragen de moleculen evenveel bij het binnentreden van het magneetveld als dat ze versnellen bij het verlaten ervan, waardoor er netto geen verandering in hun snelheid is. Een machine die sterke magnetische velden kan maken met snelle schakeltijden, en deze kan gebruiken om moleculen te vertragen (of te versnellen), heet een Zeeman afremmer. Het doel van dit onderzoek is om een Zeeman afremmer te ontwikkelen voor botsingsexperimenten in gekruiste moleculaire bundels.

De Zeeman afremmer die wij ontwikkelen is niet de eerste van zijn soort, maar bestaande Zeeman afremmers zijn niet gemaakt voor botsingsexperimenten tussen gekruiste bundels. De eigenschappen van deze bestaande afremmers zijn niet optimaal voor dit type experiment. In bestaande ontwerpen is de verhouding tussen de transversale en longitudinale snelheidsverdelingen inherent gekoppeld. Dit is niet wenselijk voor ons type experiment, en is één van de redenen dat we zelf een ontwerp ontwikkeld hebben.

In het ontwerp Zeeman afremmer beschreven in dit proefschrift worden de transversale en longitudinale snelheden van de moleculen onafhankelijk van elkaar beïnvloed. Dit wordt bereikt met magnetische velden van een reeks gepulseerde spoelen en magnetische hexapolen die alternerend de moleculaire bundel beïnvloeden. Het nieuwe ontwerp Zeeman afremmer combineert deze eigenschap met een efficiënte koelmethode, die experimenten faciliteert bij een repetitie tot 30 maal per seconde. Dit is mogelijk omdat de spoelen die wij gebruiken bestaan uit koperen capillairen, waardoor een constante stroom koelvloeistof vloeit.

Een moleculaire bundel kan afgeremd of versneld worden door te timing van de stroompulsen aan te passen. Een manier om dubbele stroompulsen door de spoelen te sturen was ontwikkeld om moleculaire bundels te kunnen sturen bij constante snelheid, waarbij precieze controle over de snelheidspreiding van de bundel mogelijk is. De stroompulsen worden gegenereerd met behulp van laag-voltage componenten. Ten opzichte van hoog-voltage componenten maakt dit de afremmer veiliger in gebruik. Bovendien brengt het gebruik van lage voltages de materiaalkosten van de vele printplaten en stroomvoedingen aanzienlijk omlaag.

Een theoretische studie is verricht om de voor- en nadelen van dit nieuwe ontwerp in beeld te brengen, en om details te geven over de benodigde stroompulsen door de spoelen. Deze studie toont aan dat per sequentie een grote hoeveelheid moleculen kan worden afgeremd, in vergelijking met de meeste typen Zeeman afremmers. We laten zien dat het gebruik van magnetische hexapolen tussen de spoelen een effectief middel is om de instabiliteiten van moleculaire banen te omzeilen, die typisch verwacht worden in een Zeeman afremmer die uitsluitend uit

spoelen bestaat. We demonstreren ook het gebruik van een kleine resterende stroom door de spoelen als een oplossing tegen het effect van zogenaamde Majorana transitities, waarbij het magnetisch dipoolmoment van een molecuul zich abrupt heroriënteert en hierbij zijn respons op een magnetisch veld verandert. Tot slot wordt aangetoond dat bij een relatief lage snelheid van de moleculaire bundel ons type afremmer niet meer effectief is. De hexapolen zorgen bij deze lage snelheden voor een te grote focus van de moleculen in de transversale snelheden, waardoor veel moleculen tussen de hexapolen uit de afremmer ontsnappen.

Na deze theoretische studie is er een prototype van de afremmer gebouwd, die bestaat uit 24 spoelen en 25 hexapolen. De hexapolen zijn gemaakt van een ring van zes permanente magneten. Met deze machine waren we in staat om metastabiele helium atomen af te remmen, te versnellen, en bij een constante snelheid te propageren. In elk van deze gevallen waren we in staat om precieze voorspellingen te doen over de resulterende snelheidsverdelingen met behulp van computer simulaties. Het was in deze machine niet mogelijk om het afgeremde helium met de rest van de bundel volledig te scheiden. Hiervoor was een langere machine nodig, die de moleculen met verschillende snelheden meer tijd geeft om uiteen te lopen. Wel werd er aangetoond dat de afremmer selectief is voor verschillende massa's en dipoolmomenten, met behulp van een klein deel helium dimeren in de bundel.

Voor het definitieve ontwerp van de Zeeman afremmer is voor een modulaair systeem gekozen, waarbij elke module bestaat uit een vacuüm kamer met plek voor 20 spoelen en 20 hexapolen. Deze modules kunnen individueel leeggepompt worden met een turbo-moleculaire pomp om de vacuüm condities te verbeteren ten opzichte van het prototype. Dit modulaire ontwerp staat ons ook toe om de lengte van de afremmer aan te passen aan de benodigdheden van het experiment. Dit definitieve ontwerp wordt in detail beschreven, met extra aandacht aan de ontwikkeling van de spoelen. Een precieze constructie van deze elementen is namelijk noodzakelijk voor de uitlijning van de machine, waarbij de bundelas een vrije diameter heeft van maar 3 mm.

Van dit ontwerp zijn er vijf modules gebouwd en in elkaar gezet in het lab, met een totaal van 100 spoelen en 101 hexapolen. Met deze afremmer zijn een aantal experimenten verricht met verschillende atomen en moleculen. Van vier edelgassen—helium, neon, argon en krypton—konden we de transversale snelheidspreiding in kaart te brengen, nadat ze uit de afremmer kwamen. Met deze metingen waren we in staat om de transversale-focusering eigenschappen van de reeks hexapool magneten beter te onderzoeken. Ook stelde deze metingen ons in staat om het sturen van een bundel atomen bij constante snelheid te testen voor heel verschillende snelheden. Deze meting was mogelijk door de grote hoeveelheid interne energie van deze atomen in hun eerste elektronisch aangeslagen toestand, waarbij ze een meetbare respons geven bij het raken van een microka-

naalplaat detector.

Tot slot zijn er experimenten verricht met zuurstof atomen en zuurstof moleculen. Beide deeltjes bezitten een significant magnetisch dipoolmoment in hun grondtoestand, maar ze verschillen een factor twee in massa. De detectiemethode voor beide deeltjes is bijna hetzelfde, waardoor er makkelijk gewisseld kon worden tussen de twee experimenten. Verschillende sequenties voor zowel zuurstof atomen als moleculen zijn gebruikt om het afrem-vermogen van de machine te testen. Hiermee is aangetoond dat een groot bereik aan mogelijke eindsnelheden mogelijk is voor deze verschillende deeltjes. Ook tonen deze resultaten aan dat het concept van alternerende spoelen en hexapolen resulteert in stabiele transmissie van deeltjes, en dat een extensie van de afremmer met meerdere modules mogelijk is zonder extra verliezen in de bundel.

In dit proefschrift wordt het design van een nieuw type Zeeman afremmer beschreven, een apparaat dat gebruikt kan worden om controle uit te oefenen over bundels moleculen die een magnetisch dipool moment bezitten. Deze afremmer is ontworpen voor moleculaire botsingsexperimenten tussen gekruiste bundels. We beschrijven de eerste experimenten met dit type Zeeman afremmer. De transversale en longitudinale bewegingen zijn onafhankelijk en worden apart gekarakteriseerd. In deze experimenten laten we zien dat atomaire en moleculaire bundels voorbereid kunnen worden met een afstembare snelheidsverdeling, in een enkele quantum toestand. Dit apparaat maakt gecontroleerde botsingsexperimenten met magnetische moleculen en atomen mogelijk met hoge snelheid resolutie. Dit is een belangrijke stap in het voortgaande onderzoek naar fundamentele moleculaire interacties.

Publications

1. T. Cremers, S. Chefdeville, J.M. Bakker, W.L. Meerts, S.Y.T. van de Meerakker (2019) *Direct excitation of the spin-orbit forbidden $X^2\Pi_{3/2} \leftarrow X^2\Pi_{1/2}$ transition in NO using the intra-cavity free electron laser FELICE*, Molecular Physics, DOI: 10.1080/00268976.2019.1589008
2. V. Plomp, Z. Gao, T. Cremers, S.Y.T. van de Meerakker, *Multistage Zeeman deceleration of NH $X^3\Sigma^-$ radicals*, Phys. Rev. A **99**, 033417 (2019)
3. T. Cremers, N. Janssen, E. Sweers, S.Y.T. van de Meerakker, *Design and construction of a multistage Zeeman decelerator for crossed molecular beams scattering experiments*, Rev. Sci. Instrum. **90**, 013104 (2019)
4. T. Cremers, S. Chefdeville, V. Plomp, N. Janssen, E. Sweers, S.Y.T. van de Meerakker, *Multistage Zeeman deceleration of atomic and molecular oxygen*, Phys. Rev. A **98**, 033406 (2018)
5. T. Cremers, S. Chefdeville, N. Janssen, E. Sweers, S. Koot, P. Claus, S.Y.T. van de Meerakker, *Multistage Zeeman decelerator for molecular-scattering studies*, Phys. Rev. A **95**, 043415 (2017)

Curriculum Vitae

Name	Theodorus Leonardus Cremers
Date of birth	16 november 1990
Place of birth	Nijmegen, the Netherlands
2015 - 2019	PhD in Spectroscopy of Cold Molecules, Radboud Universiteit
2013 - 2015	MSc in Physics & Astronomy, Radboud Universiteit (<i>cum laude</i>) Research project in Molecular and Laser Physics: <i>Advanced switching protocols in multistage Zeeman deceleration</i>
2010 - 2013	BSc in Physics & Astronomy, Radboud Universiteit (<i>cum laude</i>)
2003 - 2009	Atheneum, Kandinsky college Nijmegen